2016

Annual Report
Jahresbericht

Remote Sensing
Technology Institute

Department
Atmospheric Processors

DLR

Contents

1. Foreword

2016 was the year where we could take a final deep breath. From 2017 on we will see a quick succession of Earth observation missions with sensors aboard for remote sensing of the atmosphere where our department has accepted leading roles in the associated ground segments. Within only about half a decade six launches are scheduled. This is a period much more crowded than before when four instruments – GOME on ERS-2, SCIAMACHY on ENVISAT and two GOME-2 on MetOp-A and MetOp-B – were brought into low Earth orbit from 1995 to 2012.

According to the current launch manifests the "procession" of missions devoted to atmospheric science and monitoring starts in 2017 with Sentinel-5 Precursor, followed by ADM-Aeolus with Europe's first active atmospheric sensor. In 2018 the triple configuration of the GOME-2 instrument will be achieved once the third MetOp platform will have been launched. Two years later another novelty is expected – monitoring of the atmosphere over large parts of Europe from geostationary orbit. This will be Sentinel-4 exploiting the capabilities of EUMETSAT's Meteosat Third Generation platform. For the first time the atmosphere can be observed continuously during daytime without the unavoidable handicaps of polar orbits. Sentinel-5 Precursor, first on our list, has the purpose to pioneer Sentinel-5 whose lift-off is planned in 2021. While all these missions are multinational undertakings, MERLIN, the methane scout, is a bilateral venture between Germany and France. It will also be sent to space in 2021.

Only GOME-2 on MetOp-C provides us with requirements common to us. All other missions pose new and exciting challenges either because of new sensor types or much improved instrument properties. Already in 2017 we have to master the high spatial resolution of Sentinel-5 Precursor which results in very challenging data volumes to be processed. Compared to GOME-2 or SCIAMACHY, the spatial resolution will be a factor of about 100 higher. Think of a 30 Megapixel digital camera instead of a 640 × 480 pixel webcam; this is the improvement we will achieve. The algorithms and processors we have developed are prepared to digest this enormous data supply.

Concerning those future missions, the readership for this year's report still has to be satisfied with articles describing our preparatory work. However, in the coming years, more and more results can be expected. They certainly will find their way into future annual reports.

We like to thank our staff for their efforts and achievements in the past year and their contributions to the present report.

Prof. Dr. Thomas Trautmann
Dr. Manfred Gottwald

Sentinel-5 Precursor from 2017

ADM-Aeolus from 2017

GOME-2C / MetOp from 2018

Sentinel-4 from 2020

Sentinel-5 from 2021

MERLIN from 2021
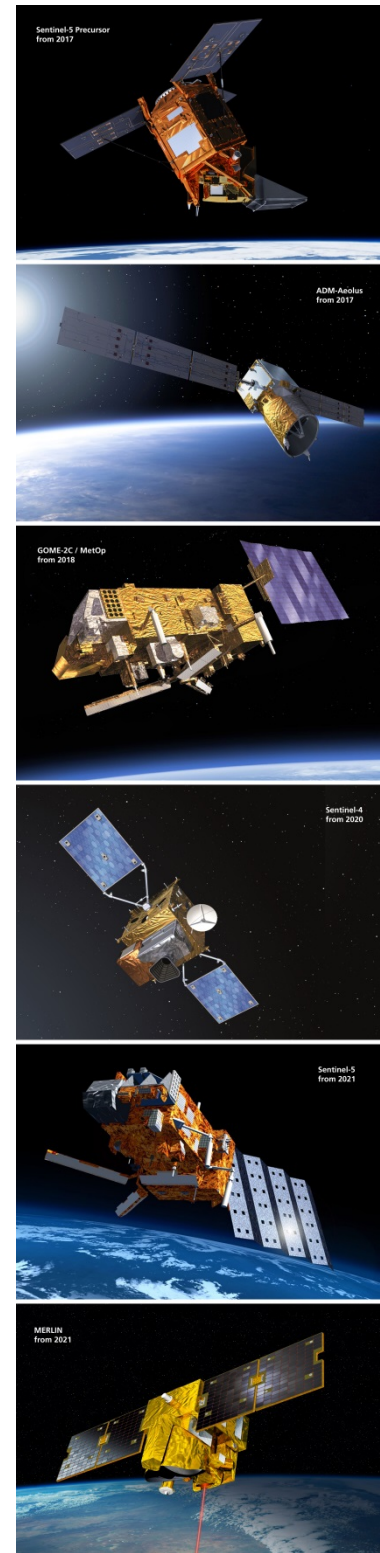
2. Atmospheric Remote Sensing – Missions and Sensors

2.1 SCIAMACHY Quality Working Group

G. Lichtenberg, B. Aberle, A. Doicu, S. Gimeno García, S. Gretschany, P. Hochstaffl, M. Meringer, F. Schreier, S. Slijkhuis

The Quality Working Group (QWG) activities in 2016 covered two major areas: the implementation of new level 1 calibration algorithms and the addition and update of level 2 retrievals.

We implemented the following changes in the level 1 processor:

- improved degradation correction using a model from SRON (*Krijger et al. 2014*)
- updated misalignment angles from in-flight calculations by IUP-IFE
- complete overhaul of polarization correction using updated algorithms from IUP-IFE and IMF
- update of bad pixel mask using results from SRON
- update of dark correction in channel 8 improving especially the orbital variance (SRON)
- investigation of the spectral calibration in channel 6 (see below) and the ISRF (see chapter 2.3)

Most of the changes were implemented in 2016 and an extended verification is ongoing to ensure that the calibration algorithms deliver the correct results. The level 2 processor had two updates. The main addition was a new tropospheric BrO product based on a BIRA algorithm. The limb cloud algorithm was updated with improved parameters. The changes currently undergo verification.

In addition to the algorithmic changes, together with the QWG we developed a new data format for level 1 and level 2 data. The current format is still based on the original ENVISAT format and the user needs custom readers to access the data. Since this hampers the general use of the data and non-standard formats also are a risk for long-term use, a new netCDF (Network Common Data Form) format was drafted by IMF. This format is oriented on the Climate Forecast (CF) convention and on the Sentinel-5(P) data formats. However, since SCIAMACHY is a much more complicated instrument than the Sentinel instruments because of its larger number of observation and calibration modes, we had to extend and adjust the format. First sample products were distributed to the QWG and presently the formats are further developed based on the comments received.

Channel 6+ spectral calibration investigations

The study described here was first presented at the ACVE conference (*Lichtenberg et al. 2016*). The channels 6+, 7 and 8 contain a certain amount of "bad" pixels, i.e. pixels that cannot be used for any retrieval, because they are too noisy, disconnected, saturate too early, etc. This is problematic for the in-flight spectral calibration: Lines from the spectral line source (SLS) are not fully sampled because they lie in a region with bad pixels (see Fig. 2-1).
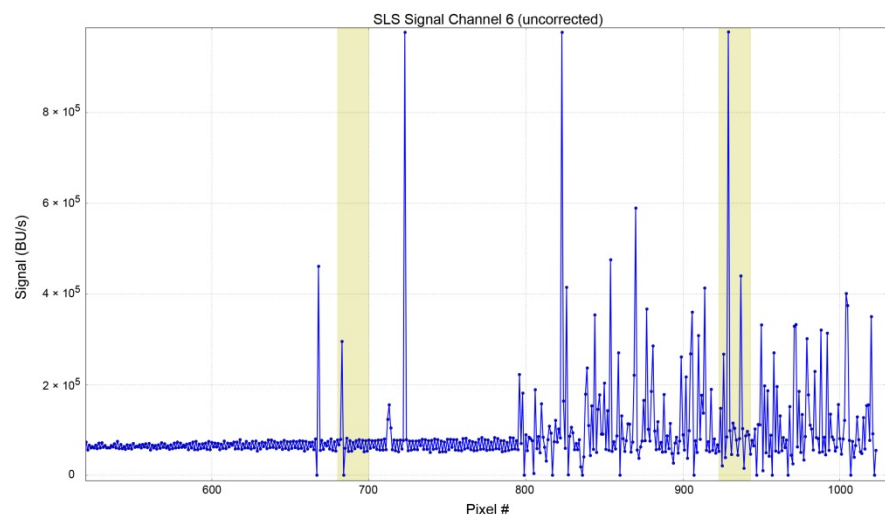

Fig. 2-1: Raw, uncorrected SLS measurement in the red end of channel 6 (called "6+"). Shaded regions mark the search area for SLS lines. The outliers are bad pixels.

Additionally, only a few lines are available in the spectral range that is covered by these channels. The level 1 processor checks the availability of lines and the quality of the signal and rejects data with insufficient quality to perform the wavelength calibration. In channels 6+, 7 and 8 the on-ground calibration is nearly never updated because of poor data quality (this is not a problem for the other channels, were the spectral calibration is updated regularly).

In order to take possible in-flight changes into account we applied an alternative calibration algorithm that was already studied for Sentinel-4 (*Noël et al. 2012*) and Sentinel-5. The algorithm uses a highly resolved solar reference spectrum and tries to fit radiance and wavelength simultaneously with a non-linear Levenberg-Marquardt fit. The fit is described by the following equation:

$$y_{fit} = P_B(\lambda) + y_{ref}(P_A(\lambda))$$

where $y_{fit,ref}$ represent the logarithm of the spectrum. The cost function for the fit is then

$$f(\lambda) = \frac{y_{fit}(\lambda) - y_{meas}(\lambda)}{\sigma(\lambda)}$$

i.e. the error weighted difference from measurement to fit is minimized. P_A represents the polynomial function for the wavelength and P_B the polynomial for the radiance.

The original approach used the full spectrum. We extended the algorithm with additional features:

- We can select arbitrary micro-windows and limit the fit to these windows. In this way one can exclude regions from the fit that are problematic due to e.g. instrumental features or other effects. All windows are concatenated and compared to the same regions in the reference.
- In a two-step micro-window approach, instead of fitting all windows, we fit only the micro-window regions individually for each window and subsequently use the results of the fits in a second fit that calculates the spectral positions for the whole channel. At the moment a polynomial fit is used.

For the Sentinel-4 UVN instrument we studied all three variants of the fit and the two step approach is the baseline to be used in the spectral calibration of this instrument. Since the method as such does not depend on the instrument, we then investigated if the method is also suitable to SCIAMACHY. In this initial investigation we concentrated on channel 6+, since here the operational CH_4 retrieval is performed (Fig. 2-2)
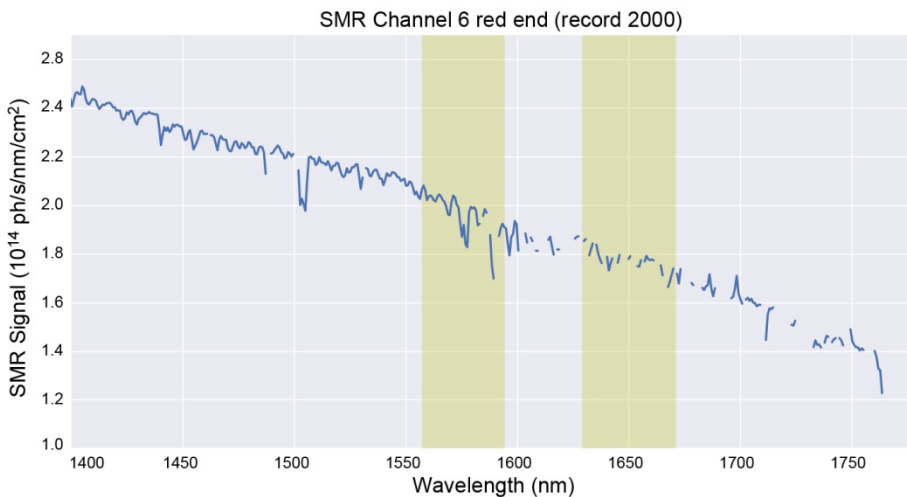
Fig. 2-2: Solar reference spectrum with bad pixels corrected (gaps) and fully calibrated.

Study set-up: In the investigation done so far we only used the full spectrum fit variant, i.e. no micro-windows. The fit depends on the chosen input parameters such as polynomial degrees for the radiance and wavelength fit, convergence criteria etc. We calculated the results for several combinations of

polynomial degrees of P_A and P_B. As input we use the level 1 data version 8, since only for this version we have the results for the complete mission available.

For the study we worked with daily Sun Mean Reference spectra. The solar reference spectrum used is the same as for Sentinel-5 instrument studies. It is based on the ATLAS-3 solar reference. We first convolved the reference with the in-flight derived spectral response function (see chapter 2.3). This is then the reference to be used in the fit.

First Results: Fig. 2-3 shows the difference between the on-ground spectral calibration and the newly fitted wavelength for different polynomial degrees of the wavelength polynomial P_A, keeping other fit parameters constant.
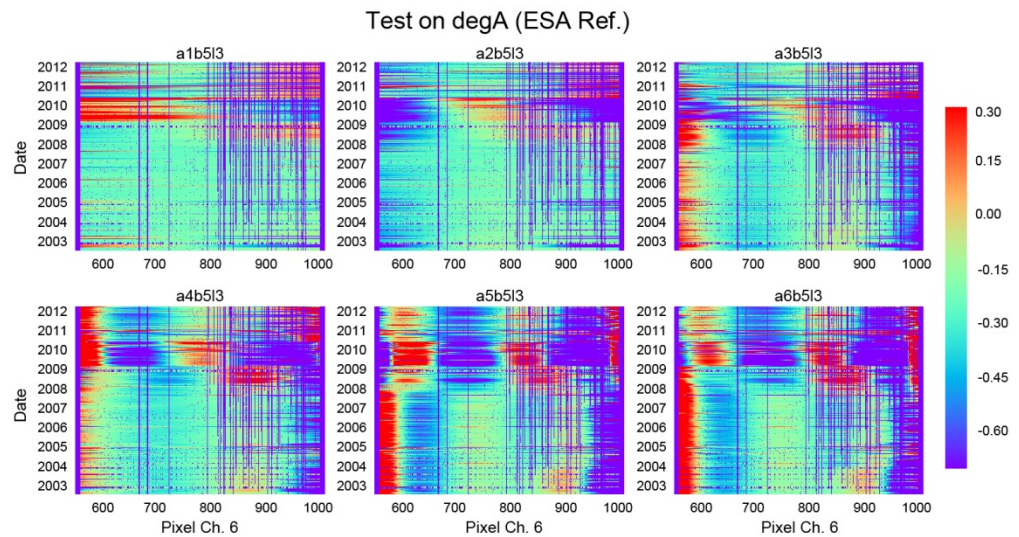
Fig. 2-3: Fit results for the whole mission. The y-axis shows the year of measurement, the x-axis the pixel number. The color indicates the shift w.r.t the on-ground calibration. Shifts between -0.7 nm and 0.3 nm are observed. Each plot shows the result for one polynomial degree of P_A with values from 1 (linear) to 6. Polynomial degrees > 4 show unrealistic high shifts. From 2009 onwards the fit gets unstable.

The shift between the on-ground and in-flight result is relatively stable for the individual pixels until March 2009. This could point to a one time on-ground to in-flight shift. After March 2009 the fit gets suddenly unstable. Therefore we explored the result in more detail. Fig. 2-4 shows the χ^2 of the fit over time.
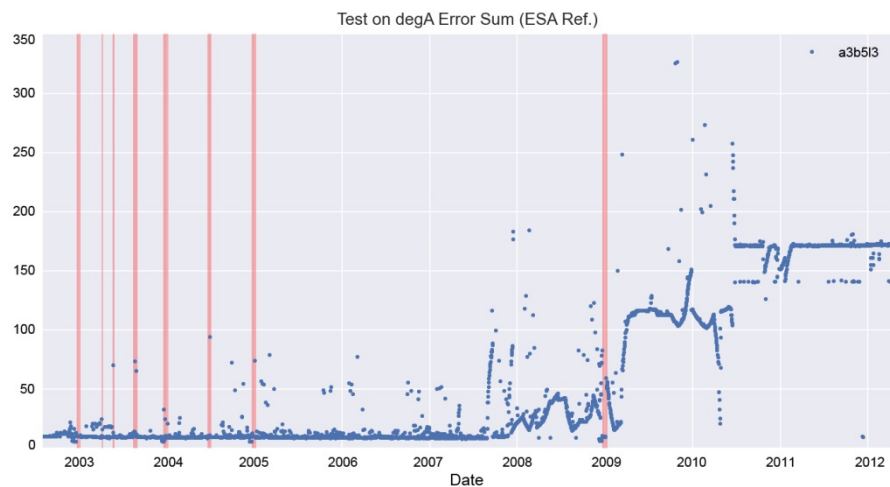
Fig. 2-4: Error sum for the fit (degree $P_A = 3$) over time. Shaded regions show decontaminations.

It is clear that the fit starts to get gradually worse from 2008 onwards and then, suddenly in March 2009 and in June 2010 the fit gets considerably worse. One obvious reason for the sudden drop in fit quality is that a pixel important for the fit gets bad. Therefore, next we looked at the number of bad pixels over time (Fig. 2-5). For March 2009, no obvious change in the number of bad pixels is visible. But surprisingly, the number of bad pixels drops in June 2010. Since this result is unexpected, we looked at the uncorrected sun signal to exclude an error in the bad pixel determination. The solar measurement confirms the drop in the number of bad pixels: Pixels that previously exhibited an unrealistic signal show a similar signal as their neighbours after June 2010 (Fig. 2-6). This indicates that the pixels indeed went from bad to good (or at least better) for reasons unknown. Methane retrievals from SRON also report a sudden change in the results from June 2010 onwards.
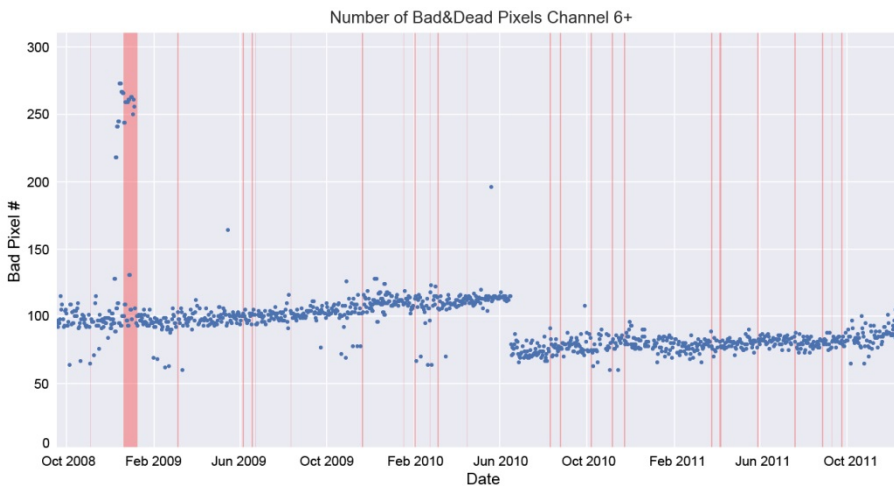
Fig. 2-5: Number of bad pixels in channel 6+ over time. In June 2010 the number of bad pixels drops for an unknown reason. Shaded regions mark decontaminations and instrument anomalies.
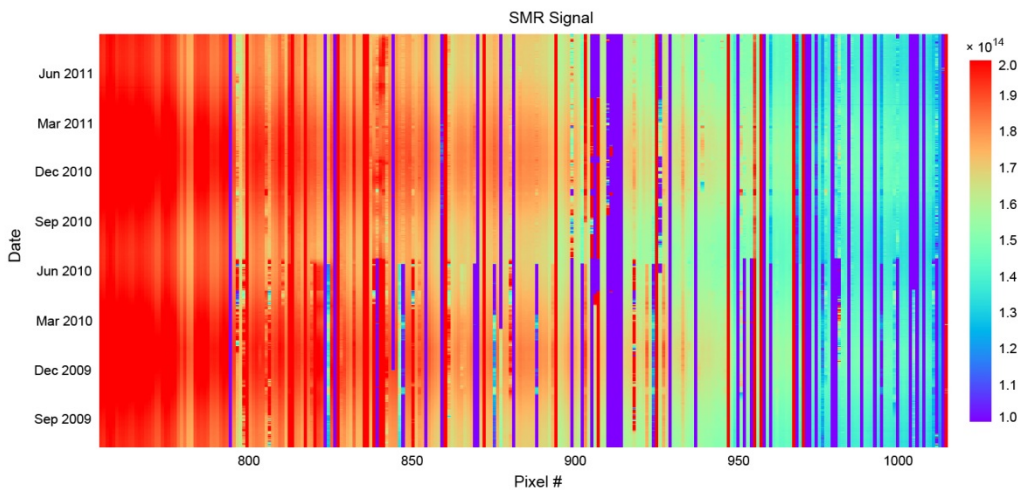
Fig. 2-6: Solar signal for pixels in channel 6+ versus time. Several pixels that show unrealistic signals (color) suddenly improve in June 2010.

Future steps: Next, we will further investigate the reason for the sudden change of the pixel behaviour and the worsening of the fit. No obvious instrument change or operation, e.g. a decontamination, coincides with the change. It is also possible that there was no significant change in the pixel behaviour, but that some of the "improving" pixels had characteristics that were on the threshold for being flagged bad and that a slight change just moved them in the "good" region again (the flagging uses fixed thresholds). However, looking at the signal differences of up to a factor of two for the sun measurements, this cannot be the case for all those pixels. Our investigation will be continued using version 9 of the level 1 data, once it has been verified at the beginning of 2017.

References

Krijger, J.M., Snel, R., van Harten, G., Rietjens, J.H.H., and Aben, I.: Mirror contamination in space I: mirror modelling, Atmos. Meas. Tech., 7, 3387-3398, doi:10.5194/amt-7-3387-2014, 2014.

Noël, S., Bramstedt, K., Bovensmann, H., Gerilowski, K., Burrows, J.P., Standfuss, C., Dufour, E. and Veihelmann, B.: Quantification and mitigation of the impact of scene inhomogeneity on Sentinel-4 UVN UV-VIS retrievals, Atmos. Meas. Tech., 5, 1319-1331, doi:10.5194/amt-5-1319-2012, 2012.

Lichtenberg, G., Hamidouche, M., Schreier, F., Hochstaffl, P., Meringer, M.: SCIAMACHY: Spectral Calibration in the SWIR Channels, presentation at the ACVE workshop, ESRIN, Frascati, 18-20 October, 2016.

2.2   SCIAMACHY Operations Support in Retrospect

M. Gottwald, E. Krieg (TwIG), K. Reissig (IBR), J. How (TwIG), S. Noël, K. Bramstedt, H. Bovensmann (all IUP-IFE)

April 30, 2016 our SCIAMACHY Operations Support officially became history when the SOST phase F had been successfully terminated. This ended a 20 year long period where a small team, the SCIAMACHY Operations Support Team (SOST), formed by personnel from DLR's Earth Observation Center (EOC) and the Institute of Environmental Physics / Institute of Remote Sensing (IUP-IFE) at the University of Bremen was – in close cooperation with ESA – responsible for instrument operations and certain aspects of instrument performance monitoring. For DLR's part the SOST composition did not change throughout the entire time and ensured that the experience and knowledge gained throughout the SCIAMACHY mission phases could always be appropriately used.

When in early 1996 the German Remote Sensing Data Center (DFD) accepted our space agency's request to establish the SCIAMACHY Operations Support function at our premises and to develop, in close cooperation with IUP-IFE's SOST part, the necessary expertise together with hard- and software subsystems for interfacing with the SCIAMACHY mission partners, it was a novel approach for us. DFD's realm had always been data oriented with command & control of the sensing instruments falling under the responsibility of mission operations centers. However, the status of SCIAMACHY as an Announcement of Opportunity (AO) instrument on ESA'S ENVISAT platform required a

Fig. 2-7: An iconic item: The SOST logo, inspired by the SOST meeting witnessing the total solar eclipse on August 11, 1999.

different solution. DLR as one of the instrument providers had to assure that instrument command & control, system monitoring and mission planning were developed in phases C/D and interfaced to ESA facilities for flawless operations of SCIAMACHY as part of the ENVISAT payload complement in phase E. This meant that SOST closely cooperated with the industrial development teams at Astrium and Dutch Space and the ENVISAT teams at ESOC, ESTEC and ESRIN. When the commissioning phase had been successfully accomplished and routine operations were about to start, responsibility for operating the instrument on AO side had been transferred from industry to SOST. Then, for almost 10 years we had to ensure that SCIAMACHY, which had been in the mid-90s for a while Germany's biggest national space endeavor, operated with high efficiency for delivering as much high-quality data as possible.

The story of SCIAMACHY operations has been told in many chapters of our past annual reports. A brief summary of 10 years SCIAMACHY operations can be particularly found in the 2012 report after the ENVISAT mission had ended with the April 8, 2012 platform malfunction. Much more detailed is the SCIAMACHY In-orbit Mission Report (*Gottwald et al. 2016*) which was published with the end of the SOST phase F. Furthermore two books, an internal space agencies publication followed by an expanded Springer issue (*Gottwald and Bovensmann 2011*) highlight the SCIAMACHY mission and how SOST contributed to it. Today, this final SOST chapter in our department's annual reports only summarizes what we had achieved and provides some lessons learnt which might be helpful just in case similar tasks will again be hosted by EOC.

SCIAMACHY Operations Summary

Since the start of quasi-routine measurements on August 2, 2002 a continuous stream of high-quality data had been acquired by SCIAMACHY. With more than 10 years in orbit, SCIAMACHY's data harvest considerably exceeded the original objective. Successful in-orbit operations were one of the prerequisites for achieving this. Particularly notable were

- **Mission operations phases**: All of the mission phases – commissioning, routine operations with two mission extensions – were passed with success. The ground segment functions for operating the instrument were implemented, tested and ready in time such that the planned engineering and measurement tasks could be accomplished without delays.
- **Mission planning**: SCIAMACHY's planning was well integrated into the overall ENVISAT mission planning. Throughout the mission, ENVISAT planning input had been received and processed as specified. The resulting output, i.e. the SCIAMACHY input for the ENVISAT scheduling tasks, was delivered in accordance with the interface control documents and no measurement time had ever been lost due to planning inconsistencies. The very rare cases where iterations between SCIAMACHY and ENVISAT had been required were handled via the well-established planning interfaces between SOST and ENVISAT.
- **Instrument availability**: The instrument executed the scheduled engineering and measurement programs with very high availability. Throughout the in-orbit phase the instrument was well under control. None of the subsystems had failed. In cases of occasional instrument unavailabilities, recovery actions were quick and efficient. The sophisticated but flexible operations concept (elaborated back in 1995!) permitted successful operations until the end of the ENVISAT mission. It also supported implementation of modified scientific, calibration and monitoring and engineering requirements.
- **Instrument performance**: Although degradation was existent, as is always the case in the harsh space environment, the overall performance of optical and thermal subsystems, the Line-of-Sight pointing knowledge and Life Limited Items exceeded expectations. Only water as the major contaminant hampered the usefulness of the IR channels 7 and 8 from an operations point of view. However even for this problem a solution was found by adopting the decontamination procedure appropriately such that stable conditions could be achieved for most of the in-orbit mission lifetime (note: shortly after launch a light leak became apparent in channel 7 which made generation of useful retrieval results from channel 7 impossible).
- **Data availability**: The excellent instrument performance was a precondition for accumulating an ever increasing repository of high-quality measurement data. In an extra effort the level 0 data were verified based on operational experience such that now level 0 data are available for all phases where the instrument was in measurement mode.

Lessons Learnt

Lessons Learnt from a SOST point of view, acquired in more than 10 years of SCIAMACHY in-orbit operations, comprise

- **Hardware and operations concept**: Specifying and developing in phase C/D an instrument with the goal to achieve an excellent piece of hardware is a prerequisite for successful in-orbit operations. This should be accompanied by establishing an operations concept which is on one hand flexible to accommodate modified scientific or operational requirements during operations but on the other hand provides continuity. It implies that the instrument and its command and control concept are designed such that instrumental settings can be easily changed from ground. This worked quite well for SCIAMACHY.
- **Instrument control concept**: Instrument operations also gained a lot from the control for on-board monitoring and failure detection. This had turned out to be a very elaborate concept. No non-recoverable failures had occurred and the instrument anomalies could be recovered following predefined procedures.
- **Contamination**: One of the areas where operations – and even more retrieval – were hampered by the instrument status was the recurring ice layer in channels 7 and 8. It was discovered as a surprise in the commissioning phase but could perhaps already have been addressed in phase C/D. Contamination experts were hard to find before launch. The information SCIAMACHY was provided with in phase C/D turned out to be unrealistic. Properly addressing contamination might have resulted in suitable on-board devices for efficiently

removing contaminants (ice) or even dedicated means for monitoring contaminants. However it also has to be mentioned that SCIAMACHY's flexible operations concept permitted to establish work-arounds, i.e. non-nominal decontamination with a well-defined sequence of warm-up/cool-down activities, which helped to recover the performance of the IR channels 7 and 8.

- **LoS pointing knowledge**: The SCIAMACHY Line-of-Sight (LoS) pointing knowledge had improved considerably over the mission lifetime even until the end of phase F, partially because of corrections on platform level and partially as the result of in-depth analyses of available pointing information. However the tight geolocation requirements in limb observations were particularly challenging and still left some questions unanswered. When improving the LoS pointing knowledge, SOST and partners could only use the available – but limited – information. Additional means for pointing analyses, e.g. Sun Follower data with higher data rate, would have been an asset.

- **Consolidated level 0**: Instrument monitoring used level 0 measurement data in consolidated format. Therefore an unambiguous cL0 data set was a must for all in-orbit mission phases. When the ENVISAT Payload Ground Segment was specified, this aspect had not been addressed such that a verification of the quality of the cL0 data had to be implemented at a later stage. Future missions should aim at generating an excellent record of consolidated data from the very beginning of a mission.

- **Involved teams**: A factor which contributed significantly to the mission success was highly motivated staff participating in industry, supporting science institutes and agencies. A good communication between the partners ensured open exchange of information and permitted to cooperate without always relying on formal rules.

- **Information exchange**: The SOST website, specified about half a year before launch and becoming operational at launch, was one of the big assets. It provided actual operations information to all mission participants, thus permitting to be always up-to-date on the instrument status. In addition, it relieved from generating numerous reports and formal documentation.
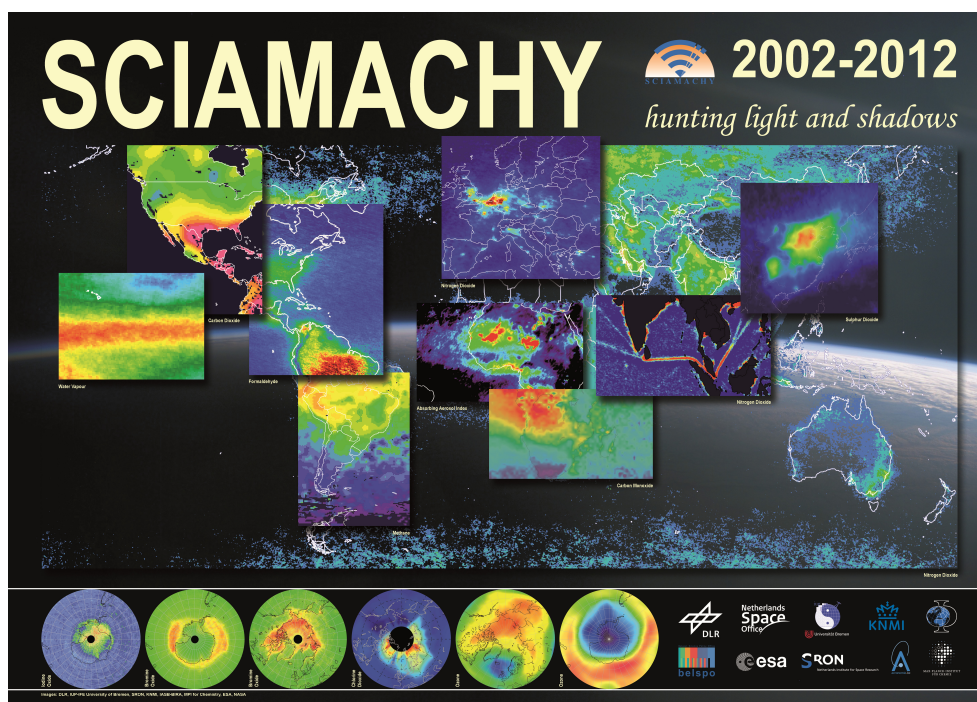

Fig. 2-8: The SCIAMACHY poster commemorating 10 years of successful operations. It was issued at ESA's Atmospheric Science Conference 2012 in Bruges, Belgium.

References

Gottwald, M., Krieg, E. Lichtenberg, G., Noël, S., Bramstedt, K., Bovensmann, H., Snel, R., Krijger, M.: SCIAMACHY In-Orbit Mission Report, PO-TN-DLR-SH-0034, Issue 1, Rev. 0, 30 April 2016, 2016. Available under http://atmos.caf.dlr.de/projects/scops/

Gottwald, M., Bovensmann, H. (Eds): SCIAMACHY - Exploring the Changing Earth's Atmosphere, ISBN 978-90-481-9895-5, DOI 10.1007/978-90-481-9896-2, Springer Dordrecht Heidelberg London New York, 2011.

2.3   SCIAMACHY Spectral Response Function: In Flight Retrieval and Analysis

M. Hamidouche, G. Lichtenberg, M. Gottwald

Our department had a leading role in the development of the operational processors for SCIAMACHY (see also chapter 2.1) and in the monitoring of the instrument performance over time (*Gottwald and Bovensmann 2011*). In this context, we investigated the role of the SCIAMACHY instrument spectral response function (ISRF), also referred to as *slit function*, on the retrievals as well as its behavior over time and in different spectral regions. In fact, the ISRF is one of the key components that are needed to perform spectral calibration and to process level 1 and level 2 data products. It is therefore essential to characterize its shape and behavior.

We developed a method to retrieve the instrument in-flight ISRF by using SCIAMACHY solar measurements. In order to recover it, we modeled SCIAMACHY-like solar measurements as the following:

$$Model = SCIAMACHY\ pixel\ sampled\ (solar\ spectrum \otimes ISRF) + Noise \qquad (1)$$

where the input solar spectrum is an existing theoretical one. After the convolution, the resulting spectra were pixel sampled to match the SCIAMACHY wavelengths axis in order to fit the models against the measurements.

The ISRF is the free component in the model. It is a mathematical function that we modeled as an exponential for channel 6 and a Voigt one, i.e. a convolution of a Gaussian and a Lorentzian function, for channel 8. The corresponding widths, as well as the exponent in the case of the exponential one, are our free parameters. The in-flight ISRF was deduced from the best fit of the measurement.

SCIAMACHY solar measurements

We used the daily solar measurements from level 1b data taken over the entire lifetime of the mission. Since the ISRF might vary slightly across the spectral channel we tried to retrieve it in as many wavelengths as possible within each channel. However this approach had its limitations because the raw solar spectra did not cover the entire wavelength range within the channels. Therefore the ISRF could not be retrieved at these missing wavelengths. We identified various solar lines at different wavelengths from the measured spectra for the fitting. The choice of the lines was sensitive due to few constraints. We needed strong and relatively narrow lines, but yet well sampled, covering enough pixels (at least about ten pixels), and showing complex structures within the selected range. All these were key points for a consistent and a reliable fitting.
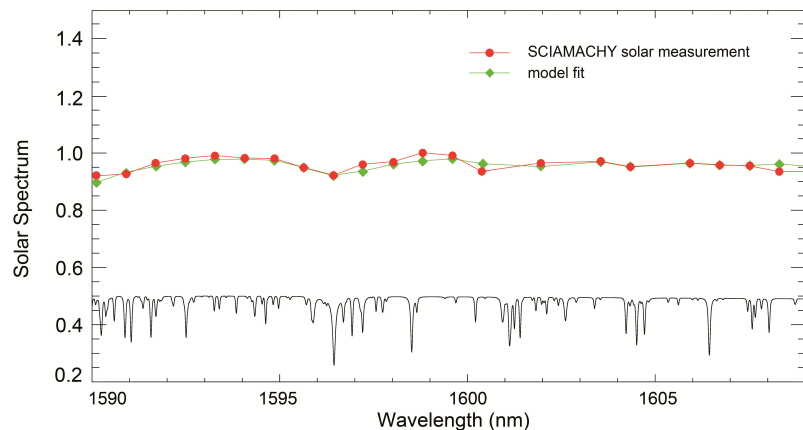

Fig. 2-9: SCIAMACHY solar measurement and the fitted model which is pixel sampled to match the SCIAMACHY axis in channel 6. The bottom high resolution spectrum is the raw (theoretical) one that we used to calculate the model.

12

However, due to ice accumulation over time on certain pixels in channel 8, the number of usable or available pixels decreased over time, which reduced significantly the number of usable solar lines for the fitting.

Fig. 2-9 illustrates an example of both a measured solar spectrum by SCIAMACHY and the corresponding modeled one over the sub-region 1590-1610 nm. Some pixels were missing in the measurement as they were flagged and thus dismissed here. The raw solar spectrum (shown in black) was used in equation (1) above. Although the raw spectrum included several solar lines, the measurement resolved only the line around 1596 nm in this spectral (sub-)region.

Retrieved ISRF

The in-flight ISRF was deduced from each solar measurement on a daily basis (excluding decontamination and anomaly orbits) during the lifetime of the mission. Fig. 2-10 shows two examples of such ISRFs for channels 6 and 8 respectively. In channel 6, the slit is obtained from the fitting shown in Fig. 2-9 and its FWHM = 1.5 nm which is consistent with the expected width of 1.48 nm (*Lichtenberg et al. 2006*). The example shown for channel 8 has a FWHM = 0.28 nm which is higher by ~7% than the expected value of 0.26 nm (*Lichtenberg et al. 2006*).

Probing the ISRF over time

The ISRF function might vary over time and its FWHM is one of the key parameters in probing any variation or stability as this defines the spectral resolution. We analyzed the FWHM evolution over time. However, we dismissed peculiar orbits/days where the solar measurement did not include enough pixels to run a consistent fitting, as in some orbits most pixels were flagged in level 1 data. This was seen in both channels but it was more common in channel 8.

We present in Fig. 2-11 some of our results in channel 6 and 8 respectively. These are the corresponding FWHM of the retrieved ISRF as a function of time on a daily basis, excluding the peculiar days mentioned earlier. The presented results span the timeframe starting at the beginning of the mission until 2009 (channel 6) and until 2005 (channel 8). In the periods beyond these dates up to the end of the mission, the fitting accuracy deteriorated considerably which is likely due to the increase of the
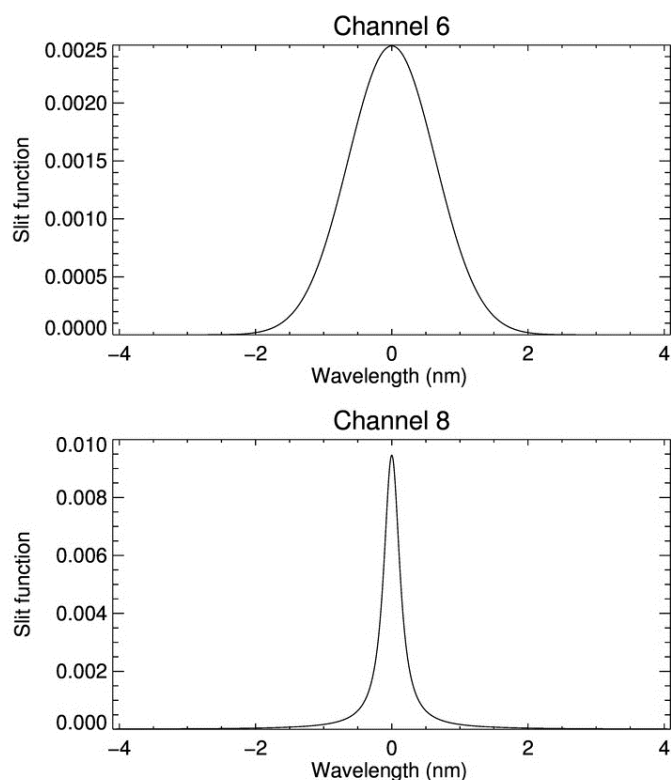

Fig. 2-10: SCIAMACHY retrieved slit function in channel 6 (top) and channel 8 (bottom).
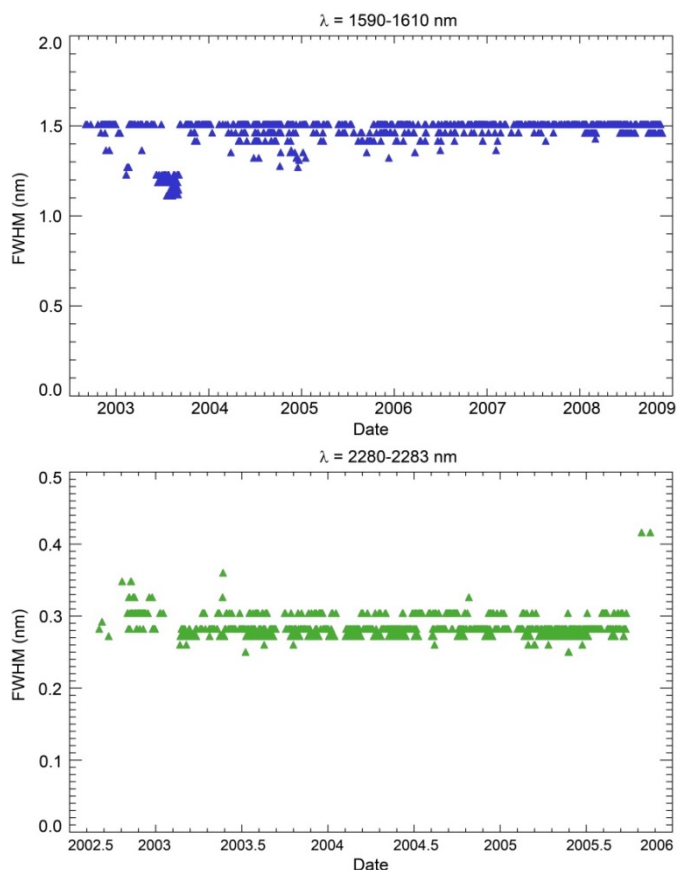

Fig. 2-11: ISRF's FWHM in channel 6 (top) and channel 8 (bottom) plotted as a function of time over several years. The corresponding ISRFs were retrieved over the spectral region 1590-1610 nm (channel 6) and 2280-2283 (channel 8).

number of flagged pixels in the measurements. In channel 6 the FWHM turned out to be relatively stable except for about three months in 2003 where it dropped down to ~1.2nm. In channel 8 the values show some fluctuations of about ± 4% around a mean value of 0.28 nm. Besides that there are no significant variations, such as strong spikes or drops in the plot. Additionally, there is no peculiarity around mid-2003, as seen in channel 6.

References

Gottwald, M., Bovensmann, H. (Eds): SCIAMACHY - Exploring the Changing Earth's Atmosphere, ISBN 978-90-481-9895-5, DOI 10.1007/978-90-481-9896-2, Springer Dordrecht Heidelberg London New York, 2011.

Lichtenberg, G., Kleipool, Q., Krijger, J.M., et al.: SCIAMACHY Level 1 data: calibration concept and in-flight calibration; Atmos. Chem. & Phys 6, 5347-5367, 2006.

2.4 Sentinel-5 Precursor Level 2 Project

D. Loyola, P. Hedelt, and the S5P-Team

The Sentinel-5 Precursor (S5P), Sentinel-4 (S4), and Sentinel-5 (S5) missions are dedicated to monitoring the composition of the atmosphere for the operational *Copernicus Atmosphere Services* including the monitoring of air quality, stratospheric ozone and solar radiation, as well as climate monitoring. S5P will be a dedicated satellite operated by ESA whereas both S4 and S5 missions will be carried on meteorological satellites operated by EUMETSAT.

The Tropospheric Monitoring Instrument (TROPOMI) is the instrument aboard of S5P. It is conceived as a partnership between ESA and Dutch Space, KNMI, SRON and TNO, on behalf of NSO. TROPOMI is a space-borne nadir viewing spectrometer with bands in the ultraviolet and visible (270 to 495 nm), the near infrared (675 to 775 nm) and the shortwave infrared (2305 to 2385 nm). Both the TROPOMI instrument and the S5P satellite are ready for flight with the launch of S5P currently foreseen for summer 2017.

NO$_2$ column density (10^{15} molec/cm^2)

0.0   15.0

Fig. 2-12: Tropospheric nitrogen dioxide over Germany between 2005 and 2009 as measured by OMI.

TROPOMI combines daily global coverage with a high spatial resolution of 3.5 × 7 km² for focusing on the troposphere where concentrations of trace gas and aerosol species rapidly change. The superior spatial resolution is one of the big assets of TROPOMI when compared with the present sensor generation as represented by GOME-2 on the MetOp platforms where ground pixels are larger by two orders of magnitude. Even the Dutch-Finnish OMI instrument on NASA's Aura satellite, which

already excels with a pixel size of 13 × 24 km^2, will be by far outperformed by S5P. Fig. 2-12 illustrates what can be expected from S5P trace gas retrievals. It shows tropospheric nitrogen dioxide (NO$_2$) over Germany for a 5-year period measured by OMI. High concentrations of NO$_2$ are obvious over large cities and areas with dense population. Even along the main traffic routes indications for considerable air pollution exist. Owing to the significantly better spatial resolution of TROPOMI, air quality monitoring of urban areas and transportation routes will improve considerably. We expect to retrieve maps of air pollution with unprecedented accuracy. The work on such TROPOMI/S5P geophysical products is organized in the two projects described below. It is funded by ESA together with national contributions from The Netherlands, Germany, Belgium and Finland.

S5P Level 2 Working Group

The S5P Level 2 Working Group (L2WG) is responsible for the development of TROPOMI geophysical products including ozone (O$_3$), NO$_2$, sulphur dioxide (SO$_2$), formaldehyde (HCHO), carbon monoxide (CO), methane (CH$_4$), as well as UV, cloud and aerosol products (Fig. 2-13). The L2WG with co-lead by KNMI and DLR is organized in three groups covering: (i) retrieval algorithms, (ii) scientific verification, and ultimately (iii) the data processors to be used in the ground-segment for the generation of the operational S5P products.
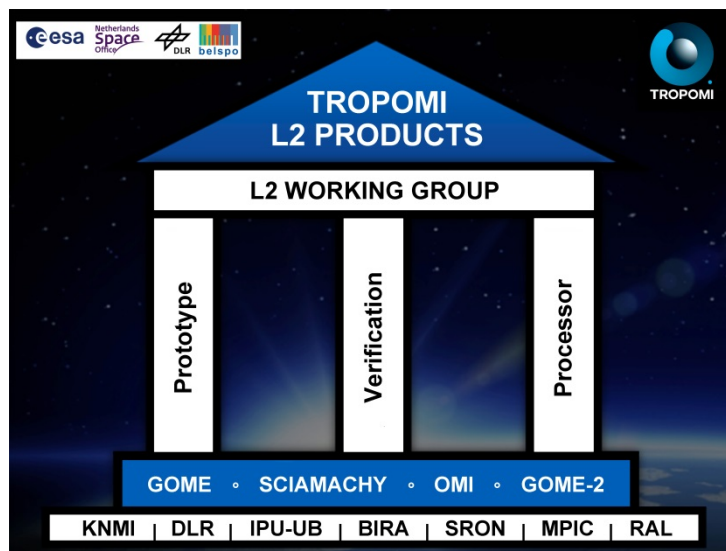
Fig. 2-13: S5P L2WG project organization.

As part of this project DLR-IMF is developing the UPAS processor for S5P. An updated version of UPAS was delivered to ESA by end of 2016 and this version was successfully integrated and tested in the S5P Payload Data Ground Segment system being developed at DLR-DFD. Of the geophysical products listed above, the UPAS system will generate the following S5P operational products: total O$_3$, tropospheric O$_3$, SO$_2$, HCHO, and cloud properties. The S5P L2WG project is coordinated by ESA/ESTEC and it will be concluded by the end of the commissioning phase.

S5P Mission Performance Center

The S5P Mission Performance Center (MPC) project is the element within the ground segment in charge of calibration, validation, end-to-end system performance monitoring, quality control, and maintenance of the level 1 and level 2 data processors. The overall coordinator of the S5P MPC project is KNMI with DLR leading the Expert Support Laboratories (ESLs) responsible for the level 2 activities including the level 2 quality control and validation, and the maintenance of the level 2 processors (Fig. 2-14). The S5P MPC project is coordinated by ESA/ESRIN. It was started in the 2nd quarter of 2016. This project will cover the complete S5P mission with an expected duration of at least seven years.
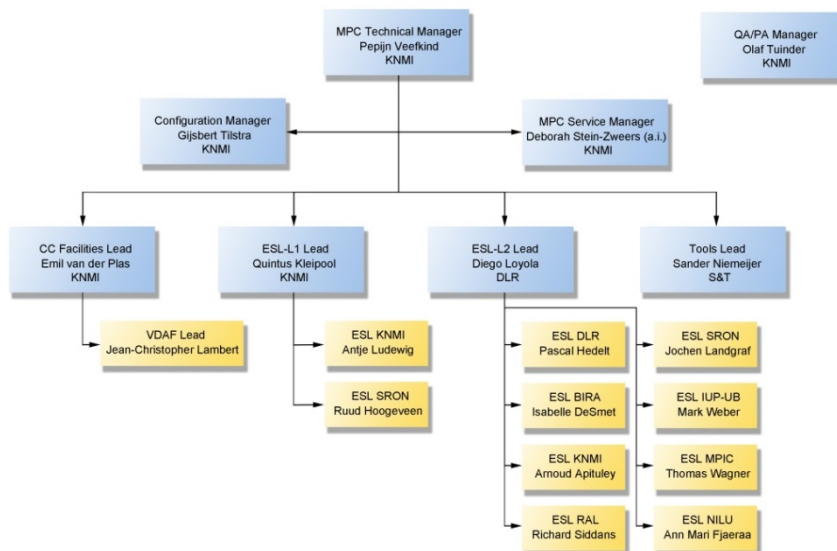
Fig. 2-14: S5P MPC project organization.

2.5 Sentinel-4 Straylight Correction Algorithm

S. Slijkhuis, G. Lichtenberg

Sentinel-4 (S4), ESA/EUMETSAT's future mission for atmospheric sounding can be considered a follow-up to ESA's GOME and SCIAMACHY missions. Its UV-VIS-NIR spectrometer is being developed by Airbus. The accuracies required by ESA for this instrument are very high, and accordingly a high precision is demanded for instrument calibration and level 1b data processing. We support Airbus in the development of the level 1b processing algorithms, especially with regard to spectral calibration and straylight correction.

The proposed straylight correction algorithm splits the straylight into focused "ghost" straylight, and diffuse straylight. The former has been greatly reduced by instrument design. In addition, the correction for focused ghosts is reasonably straightforward. The correction for diffuse straylight is demanding, both for on-ground calibration measurements, and for level 1b processing time. In principle, the signal measured on every CCD pixel generates straylight on all other CCD pixels. This is described by a *straylight kernel*. Neither in the on-ground calibration, nor in the level 1b processing, is it possible to take into account the straylight kernel from every pixel, because this would take far too much time. Some sort of simplification must be made, but at the same time the stringent ESA requirements must be fulfilled.

Airbus has performed simulations of the instrument, to provide us with the expected straylight kernels. However, straylight is very difficult to simulate precisely, and therefore these simulations are no substitute for instrument calibration measurements. But they may give a good impression of how the straylight may approximately look like. We have used these simulations to perform a full closed-loop test of the straylight correction algorithm:

- The Airbus kernels are used to calculate the "true" straylight for an in-orbit ground scene – this gives a CCD image of "measured" atmospheric spectra including straylight.
- The Airbus kernels are used to calculate the straylight for on-ground calibration measurements; CCD images of the calibration source including straylight and the expected measurement noise are generated.
- The algorithm which derives simplified straylight-correction data ("calibration key data", CKD) from the calibration measurements is applied.
- The CKD are used within the level 1b straylight correction algorithm to correct the "measured" atmospheric spectra for straylight.
- It is checked that the level 1b straylight correction meets requirements.

The main difficulty in deriving CKD from on-ground calibration measurements is, paradoxically, that the instrument straylight is very low. This implies that the *straylight kernel*, i.e. the straylight which comes from a single illuminated pixel, is very low. At short distances from the input location, the kernel may be directly measureable, but at larger distances it sinks into the measurement noise (Fig. 2-15).
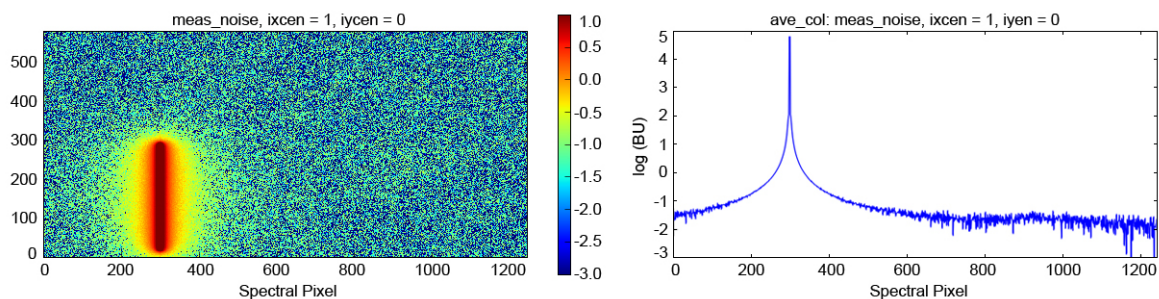
Fig. 2-15: Simulation of an on-ground calibration measurement in the Sentinel-4 UV-VIS channel. Left: image including noise, averaged over many individual measurements, colorbar scale in units of 10log (BU). Right: the image averaged over CCD rows 50-260.

In order to lift the straylight level above the noise, many pixels must be illuminated at the same time (the illumination per pixel is limited by detector saturation; the CCD detector should not be oversaturated to avoid possible damage). In order to derive the CKD straylight kernels, the calibration image must be

16

"deconvolved", such that the image for many illuminated pixels is reduced to an image for a single illuminated pixel (which is the kernel).

Classical deconvolution methods require very high signal-to-noise images, whereas we have very low signal-to-noise. We have developed an iterative method to perform this deconvolution. Starting with a first-guess for the CKD kernel, we calculate the straylight that this kernel yields for the calibration input, compare that to the calibration image, and change the kernel for the next iteration. The simplified assumption is made that, at larger distances from the source, the CKD kernel is spherically symmetric. This is not really the case, but it was shown that the resulting errors stay within the requirements. Due to the large dynamical range in the kernels, by more than 4 orders of magnitude, we do not iterate on the kernel itself, but on the ratio of straylight from all illuminated pixels to the straylight from one illuminated pixel.
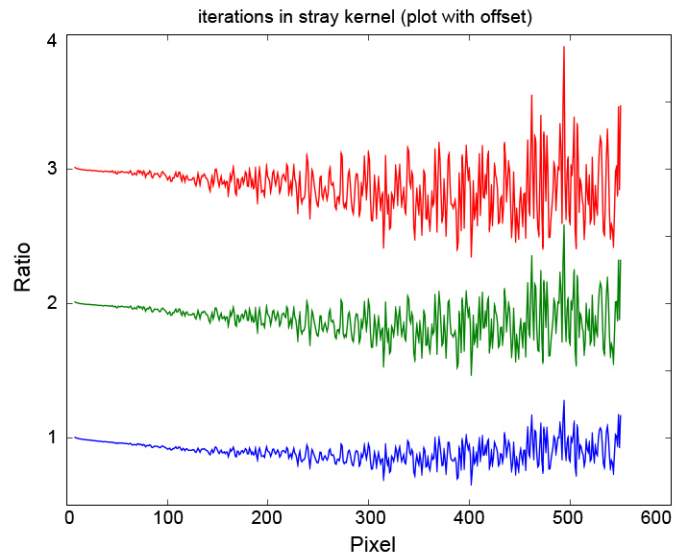
Fig. 2-16: Ratio of straylight kernel after each iteration, to the first-guess kernel, showing the noise amplification. Blue, green, red is for iterations 2, 3, 4 (ratios offset by 1.0 for clarity)

For noiseless calibration images, the method converges to the true solution. For noisy calibration images, we encounter a general problem in deconvolution, namely noise amplification (Fig. 2-16). Noise amplification could be handled by using a proper smoothing of the calibration measurements, and by limiting the number of iterations. In the end, a successful closed-loop of the S4 straylight calibration and processing chain could be demonstrated.

References

Ahlers, B., Bazalgette Courrèges-Lacoste, G., Dobber, M.: Copernicus Sentinel-4/UVN instrument calibration. CALCON, 2014. Available under
http://digitalcommons.usu.edu/cgi/viewcontent.cgi?article=1103&context=calcon

2.6   Sentinel-4 Level 2: Heterogeneous Scene Characterization

S. Slijkhuis, D. Loyola

The retrieval of atmospheric trace gases from spectrometer measurements needs as input an accurate calibration of the instrument. Once measurement spectra have been properly calibrated, the retrieval needs to know the "resolution" of the instrument, as described by the Instrument Spectral Response Function (ISRF). The ISRF describes how a monochromatic (single wavelength) light input is imaged onto the instrument's detector. Usually, a sharp spectral line will be imaged as a more or less Gaussian distribution. This distribution (the ISRF, or *slit function*) arises from optical blur in the instrument, and, more importantly for Sentinel-4, from a convolution with the slit width (more precise: the ISRF may be seen as the slit profile imaged on the detector).

The ISRF is calibrated on-ground, using a homogeneous illumination of the instrument. However, depending on the blur of the telescope system in front of the spectrometer, this may not always be representative for the in-flight situation. In case we have a sharp contrast within the scene, e.g. bright clouds against a dark background, the projection of this scene onto the spectrometer slit (by the telescope system) may cause an unevenly illuminated slit. In this case, the true ISRF is not the convolution of optical blur and slit width, but it is the convolution of optical blur and the illumination profile across the slit. If the slit is illuminated more at one side than the other (e.g. by a cloud front in the image), this will result in an ISRF that is narrower and spectrally shifted. This may have significant

consequences for the trace gas retrieval.

For existing instruments where we perform level 2 processing, i.e. trace gas retrieval, such as GOME-2 or SCIAMACHY, this effect is not significant, because these instruments scan the ground over distances of 40 km or more. Thus, scene contrasts are washed out effectively. However, for the future Sentinel-4 mission, with much higher ground resolution of 8 km, ISRF deformation by heterogeneous, i.e. not evenly illuminated scenes may be important.

ISRF modelling
As part of the contract with ESA to provide a level 2 prototype processor for Sentinel-4, IMF-ATP develops methods to characterize heterogeneous scenes from the measurements, and to mitigate the effects of ISRF deformation on the trace gas retrieval. This follows up on an earlier phase-A/B study for the Sentinel-5 instrument. As a first step, a forward model has been developed to calculate the ISRF for a number of wavelengths in the spectrum, and to simulate measured spectra over heterogeneous scenes. The model incorporates blur of the ground scene by telescope optics, polarization scrambler, and scanning movement. The high-resolution input spectra of dark and bright parts of the scene are blurred by spectrometer optics, pixel-binning, and slit illumination profile. The model is able to perform a spectral recalibration of measurement spectra, to compensate for shifts due to an asymmetrical ISRF, and it calculates the effects of ISRF narrowing (Fig. 2-17).
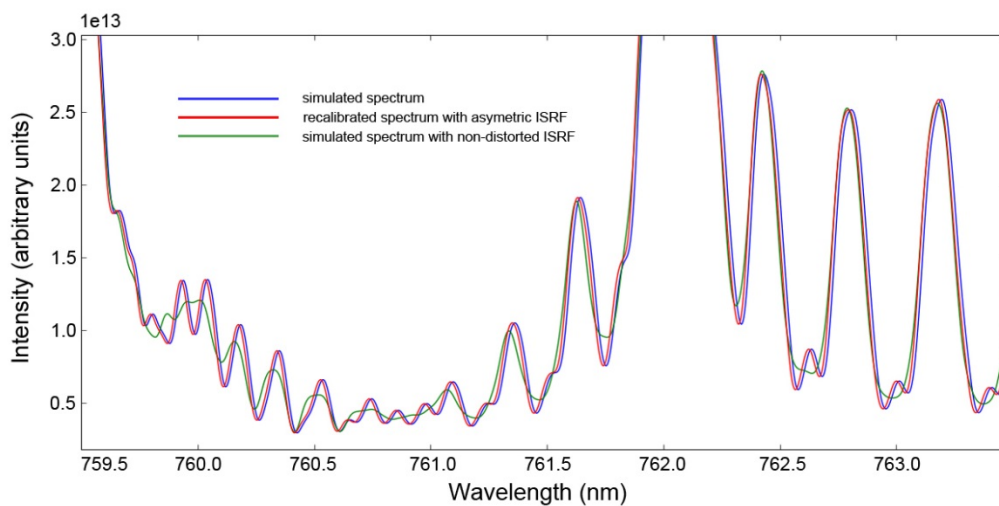
Fig. 2-17: Simulated measurement spectra of the core of the O_2-A band over a strongly heterogeneous scene illustrating the effects of an asymmetric ISRF, contrary to a non-distorted ISRF.

In case the input spectra of the dark and bright scene components have a significantly different small-scale structure, as may happen in strong atmospheric absorption bands, e.g. the O_2-A band, the concept of the ISRF as a spectral convolution kernel breaks down. Also this situation can be handled in the model, by a finite-element treatment of the slit.

Scene characterization
The instrument on Sentinel-4 measures at a higher temporal sampling rate in a few selected wavelength bands, the so-called "High Speed Sampling (HSS)" bands. The forward model has been used to establish a matrix formalism where the slit illumination is calculated as a function of the HSS band intensities. This may then be used to estimate the ISRF for the scene. Since the ISRF is only derived for the HSS band wavelengths, an interpolation to other wavelengths must be done.

Outlook
The forward model will be used to calculate the effect of ISRF deformation for a larger number of heterogeneous scenes and a variety of input spectra. The errors of ISRF estimation, using the HSS band measurements, will be assessed. Mitigation strategies will be proposed, in collaboration with the developers of the Sentinel-4 level 2 trace gas retrieval algorithms.

References

Noël, S., Bramstedt, K., Bovensmann, H., Gerilowski ,K., Burrows, J.P., Standfuss, C., Dufour, E., Veihelmann, B.: Quantification and mitigation of the impact of scene inhomogeneity on Sentinel-4 UVN UV-VIS retrievals, Atmos. Meas. Tech., 5, 1319-1331, 2012.

Caron, J., Sierk, B., Bezy, J.L., Loescher, A., Meijer, Y.: The Carbonsat Candidate mission: radiometric and spectral performances over spatially heterogeneous scenes, International Conference on Space Optics, Tenerife, 2016. available under
http://esaconferencebureau.com/Custom/ICSO/2014/Papers/3.%20Thursday%209%20October/Session%2011C%20Earth%20Atmospher%20Spectometers%201/3.66399_Caron.pdf

2.7 MERLIN Level 0-1 Data Processing

G. Lichtenberg, M. Hamidouche, B. Aberle

MERLIN, the Methane Remote Sensing Lidar Mission, is an effort for measuring the methane (CH_4) content of the atmosphere. It will be the first Integrated Path Differential Absorption (IPDA) Lidar mission in space. CH_4 will be determined with high accuracy by sending two laser pulses to the ground, one with a wavelength centered in the CH_4 absorption at 1645.552 nm (λ_{on}) and one directly outside the absorption at 1645.846 nm (λ_{off}). The ground spot of the MERLIN laser will be around 100 m wide. In order to obtain sufficient signal-to-noise several shots have to be co-added, the baseline at the moment is to co-add the signal for a footprint of 50 km, i.e. to co-add 50 shots. From the comparison of the backscattered intensity of both lines the differential absorption optical depth (DAOD) of CH_4 can be calculated, i.e. the CH_4 content of the atmosphere can be inferred.

MERLIN is a German-French bilateral project. Germany's tasks are the instrument design and manufacture, instrument monitoring (see chapter 2.8) and level 0-1 processing. The responsibilities on the French side comprise the platform, the ground segment for the operational processing and the level 1-2 processing. The algorithms for level 0-1 and 1-2 processing will be defined by both partners in cooperation.

The processing steps can be summarized as depicted in Fig. 2-18. They consist of

- conversion of the raw data to time ordered level 0a data
- so-called "decommutation" of the level 0a data and relevant housekeeping data (HKTM) from the payload operational control processing, satellite positions & attitudes which produces a level 0b in netCDF format
- production of level 1a and level 1b data from the level 0b data, including auxiliary data (e.g. calibration parameters from the calibration data base)
- processing of level 2 and level 3 (re-gridded level 2 data) from level 1b data
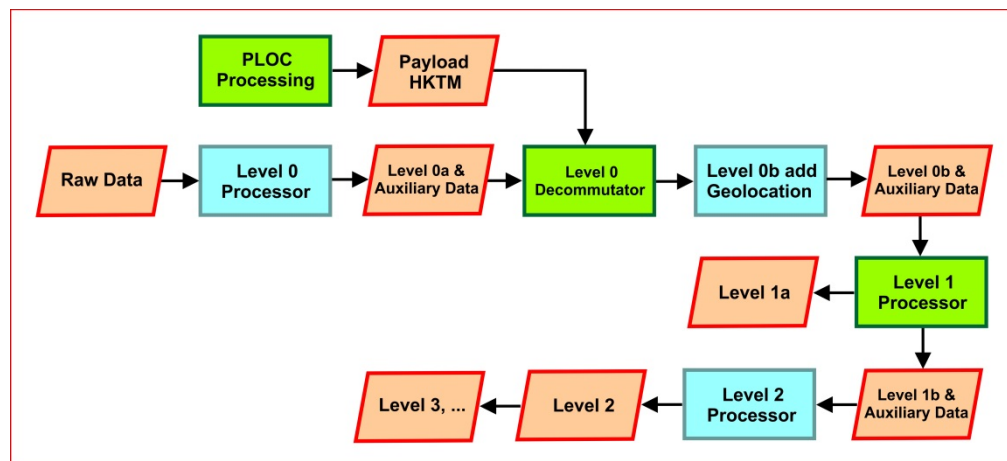
Fig. 2-18: MERLIN processing chain from raw data to level 2 and beyond.

First design of the processor

In 2016 the first version of the Algorithm Theoretical Baseline was finished by IPA and CNES. Based on the algorithms described there, the first (preliminary) design of the level 0-1 processor was developed.

The level 0b to level 1b processor converts decommutated level 0 data to DAODs of CH_4 for a given orbit. Instrumental effects are removed, quality parameters are determined and the DAOD is calculated. During the level 0b-1b processing an intermediate product, the level-1a product is generated that may be exploited by experienced users for spin-off products or for test purposes, etc. Compared to the level 1b product, the level 1a product contains shot based data and additional instrument information and is not yet averaged.

The level 0-1 processing can be conceptually divided into the following tasks:

- Calibration processing: Processing of calibration measurements
- Pipeline Processing: Processing of Earth measurements
    - algorithms on shot arrays
    - algorithms on shot array derived values
    - algorithms for averaging to the targeted resolution
- Determination of the geolocation
- Quality and flagging algorithms (partially integrated in the individual algorithms above)

The data consist of the laser signal versus time index for both wavelengths: for the online wavelength in the CH_4 absorption and the offline wavelength outside the absorption. We call this raw signal "shot arrays". From the shot arrays the backscatter signal, SNR and quality parameters are calculated ("shot array derived values"). Finally the data must be averaged to reduce noise. DAODs are calculated for the single shots and for the averaged signals. Only the latter are used in the operational level 2 processing.
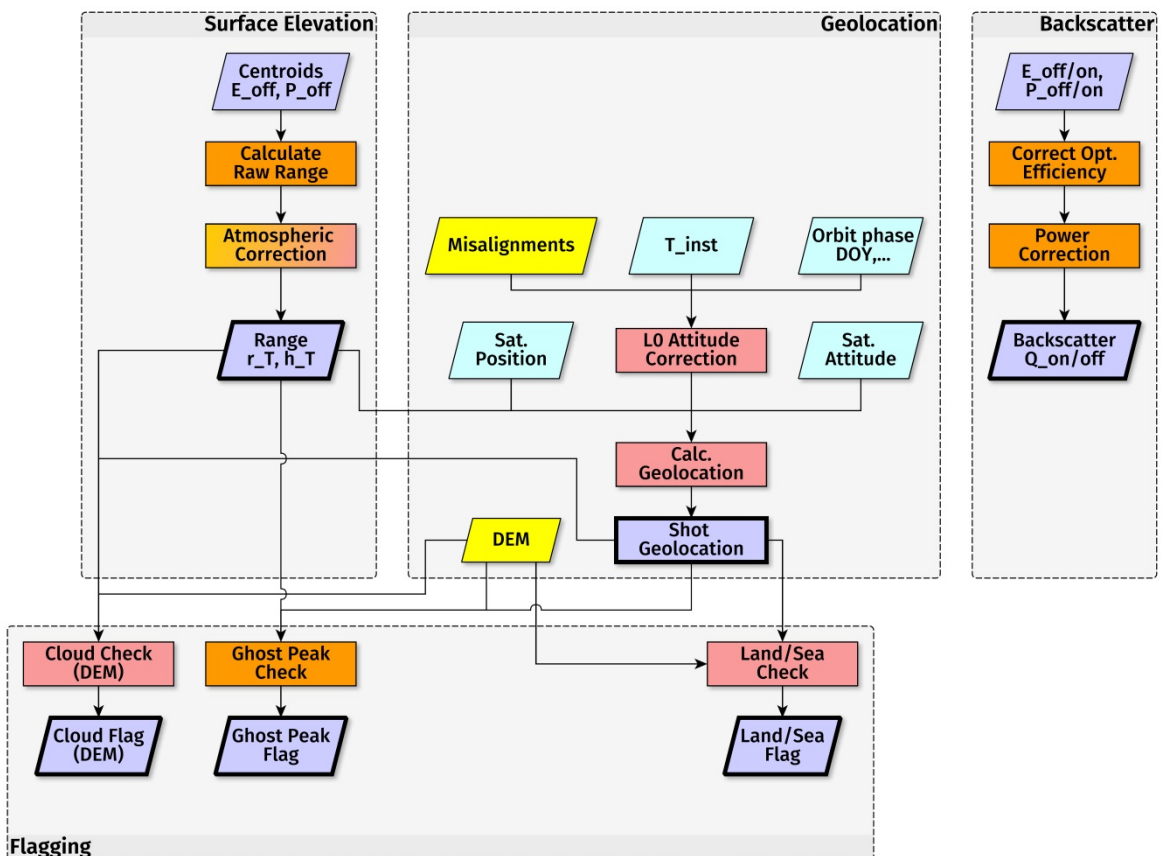
Fig. 2-19: Example flow diagram for the treatment of single shot derived values.

Fig. 2-19 illustrates as an example the flow diagram describing the processing of shot array derived values up to the backscatter coefficients. In this part of the processor, CNES geometric algorithms for the geolocation are combined with DLR algorithms for the calculation of range (altitude of the point of

reflection) and the backscatter coefficient. From the backscatter coefficients for the online and offline signals the DAODs are determined. The processor passed the first design review and the design will be further worked out in the following year.

Estimate of the required computational resources

For allowing CNES to plan the ground segment operations, an estimate of the computational resources is required. While it is presently difficult to make a reliable estimate with many algorithms not yet defined and without having any part of the processor actually implemented, it is possible to obtain a "ballpark number" by building a simple mockup processor. In order to build the mockup processor, we have to consider the following boundary conditions:

- The largest data granule the processor ingests is one orbit (L0 file). Parallelization based on orbit has to be done by starting additional processor instance(s).
- Internal parallelization (within one processing instance) will be done with the OpenMP framework.
- Whenever possible, operations will be done on complete arrays using array operations.

The computational resources were estimated by implementing a realistic number of mathematical operations estimated from the ATBD and run tests with the L1b mockup. We considered the following mathematical operations:

- addition/subtraction of two scalars
- multiplication/division of two scalars
- comparison of two scalars
- addition/subtraction of scalars and array
- multiplication/division of scalars and array
- addition/subtraction of two arrays
- multiplication/division of two arrays
- comparison of array elements with scalar
- sum over array
- mean over array
- other, e.g. Fast Fourier transform (FFT)

The input data were based on a standard orbit and nominal instrument operations (Table 2-1).

Parameter	Symbol	Value
Shot pairs per second	f_{pair}	24
Orbit duration (min)	T_{orb}	95
Orbit velocity (km/s)	v_{orb}	7.055
Pulse pairs per orbit	$N_{pair} = f_{pair} * T_{orb} * 60$	136800
Shots per orbit	$N_{shots} = N_{pair} * 2$	273600
Values per shot (on **or** off)	N_i	4900
Values per orbit	$N_V = N_{shots} \cdot N_i$	1340640000
Number of shots per 50 km	$K = 50/v_{orb} * f_{pair}$	170.09213
Number of averaged DAODs per orbit (50 km)	$L = N_{pair}/K$	804.27002
Number of pre-averaging intervals per (50 km) DAOD	$M = 10$ TBC	10
Number of pre-averaging intervals per orbit	$N_p = L \cdot M$	8042.7002

Table 2-1: MERLIN standard orbit and instrument operations settings.

In the mockup, we created 3 process functions, one for shot related calculations, one for shot derived values and one for averaging operations. In each process function we implemented a loop over all basic arithmetic operations derived from the ATBD. The only complex operation we implemented was the FFT. Interpolation, LUT operations, fitting or polynomial evaluation that all will be needed in the final operational processor were not implemented, because these are not clearly defined at this early stage. We also assumed that we can always operate on arrays instead of looping through the individual array elements. We did not perform any specific optimization by e.g. adjusting the arrays for CPU register sizes. Apart from the algorithms that still need defining, four major functionalities are not implemented in the mockup because of lacking detailed information. These are

- geolocation calculation
- DEM handling
- quality calculation and checking
- calibration algorithms

The following read/write operations were implemented in the mockup: Reading a generated level 0, reading one array of 8192 bytes from the database and writing it to the database with finally extracting a level 1b file. In view of the current uncertainties, we added a margin to our calculations. Our final estimate confirmed that 3 parallel processor instances with 32GB memory are needed in order to be able to process one day of data in under 4 hours. This gives our French partner and us a reasonable clue of how to size the corresponding ground segment subsystems.

2.8 Payload Monitoring for the MERLIN Lidar Mission

M. Hamidouche, G. Lichtenberg, B. Aberle, T. Trautmann

The new generation space-borne Lidar mission MERLIN will make very sensitive measurements of the methane (CH_4) distribution with unprecedented quality and coverage. It will provide 50 km averaged methane column concentrations. Therefore it will offer the necessary sensitivity to probe methane fluxes, over different key geographical areas, with better than 2% accuracy (*Kiemle et al. 2014*). MERLIN will eventually track down the methane sources and sinks on a global scale.

The instrument will be mounted on a satellite platform flying at an altitude of ~ 500 km in a Sun synchronous orbit. The instrument will continuously send and receive a pair of pulses at two different wavelengths. One wavelength λ_{on} is centered on a CH_4 absorption line. The other pulse is a reference at λ_{off} which is slightly shifted by a few 1/10 nm. It is located where the CH_4 absorption is relatively small but yet it is close enough to have a nearly identical interaction with the atmosphere and the reflecting surface. From the back-scattered signals of both pulses (on and off) the DAOD (Differential Absorption Optical Depth) of methane is measured, and thus its column density.

Long-term monitoring of the payload
The Payload Operations Center (PLOC) provides one of the key functions in MERLIN's ground segment. It is in charge of payload mission planning as well as payload monitoring and calibration. Our department contributes to the PLOC with the long term monitoring (LTM) functions. We will develop, maintain, and run the LTM function during both the commissioning and the operational phases. The team expects to regularly interact with MERLIN scientists, the level 0-to-1 processor team (see chapter 2.7), and the instrument designers. Developing and implementing the MERLIN LTM function will build on the experience our department achieved for SCIAMACHY (*Gottwald et al. 2016*). For the routine operations phase of this challenging atmospheric remote sensing mission starting in 2002 up to its end in 2012 we had been responsible for the operation of the instrument including long-term monitoring functions (see chapter 2.2). The lessons learnt in this phase provide a sound basis for also successfully fulfilling the MERLIN LTM requirements.

LTM is an offline function that will track the behavior of the instrument and its subsystems. It will also monitor the instrument's performance in response to scheduled or unexpected events, both of technical or natural origin. This is achieved by analyzing the measurement data (level 0, level 1, level 2) and housekeeping information over different time frames. The corresponding time scales may vary for

different functions and parameters (e.g. daily, weekly or monthly). The timescales can also change when deemed necessary by the LTM team. If a particular parameter shows unexpected temporal behavior, it may require further monitoring on shorter time scales; and therefore allowing the user to probe and constrain the origin of the detected deviation.

The LTM function ensures the health of the instrument on long timescales (e.g. by identifying long-term drifts) and may as well anticipate any deterioration effects. Even though instrument health & safety are not considered one of the main goals of the LTM function, instrument health degradation might appear gradually and therefore could only be noticed over long timescales without becoming obvious in real time.

Ultimately, long term monitoring will generate new feedback to assist existing and/or future data/scientific analysis and the calibration processes. The results of the LTM could imply operations modifications, such as

- modification of payload parameters,
- modification of calibration & data processing tools,
- modification of operation & schedule.

The laser component

One of the main components of the instrument is the laser. Some of its parameters that require long term monitoring are the emitted (Tx) and returned (Rx) pulses. One of the LTM tasks will be making analytical models to check the emitted pulse's shape, i.e. the center position, width, peak, energy, and noise level. This will also help to deduct any return delay and to monitor the repetition rate. Fig. 2-20 shows single pulses of a laser shot pair plotted as a function of bins (time) from level 0 data. In this example, the peak value is ~ 5000 and the noisy baseline is ~ 1000. Their ratio, i.e. signal to noise (SNR), will be monitored to probe the laser behavior over time and over the horizontal traveled/covered distance in km. For consistency, we will also compare and correlate it with Rx's. Monitoring the SNR will allow us to keep track of aging effects but may even have an impact on the interpretation of the measurement data.
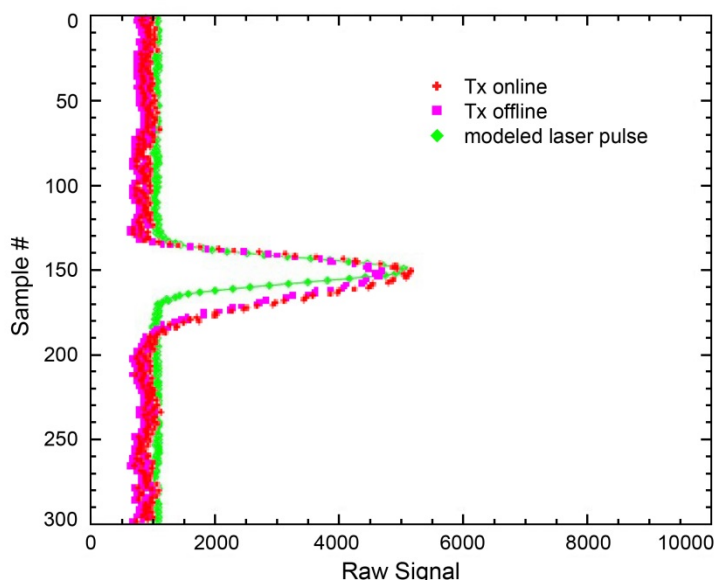
Fig. 2-20: Actual Tx laser pulses on/off together with the modeled pulse including noise.

Furthermore, Rx is another key quantity to monitor in both level 0 and level 1. In fact, over water (sea or lakes), the ground is considered relatively stable (reflectance & height) for back-scattering measurements; and thus, the estimated energy at level 0 over water will be "relatively" close to the actual energy obtained in level 1 products. When measuring over water, we expect to find a nearly linear correlation between the two over time. Detected deviations could be a hint for laser incompliances. Monitoring Rx SNR variations over suitable regions will also allow tracking the mission performance.

Pointing and footprint: Relevance and monitoring

Instrument pointing data are a valuable source of information and will be recorded over the mission lifetime. Together with the footprint positioning they will validate several key parameters such as the instrument sub-system alignments, geolocation, satellite position - including their corrections and eventually the column density measurements due to possible Doppler changes.

We intend to monitor and track the footprint position as part of the LTM. In practice, the MERLIN Lidar signal is expected to show sudden drops and rises while passing and "transiting" into or out of specific

Earth regions such as land/water or desert. When its line of sight crosses such geographical areas, we will compare its signal variation over the "transiting" region against the expected one. Similarly, MODIS surface reflectance data at the CH_4 wavelength in band 6 (*Vermote et al. 2008*) will also be used for relative comparisons with the MERLIN measurements. Signal inconsistencies would be an indication for footprint shifts.

References

Kiemle, C., Kawa, S.R., Quatrevalet, M., Browell, E.V.: Performance simulations for a space borne methane Lidar mission; J. Geophys. Res.,119, 4365-4379, 2014.

Gottwald, M., Krieg, E., Lichtenberg, G., et al.: SCIAMACHY In-Orbit Mission Report, PO-TN-DLR-SH-0034, Issue 1, Rev. 0, 2016.

Vermote, E.F., Roger, J.C., Ray, J.P.: MODIS Surface Reflectance User's Guide, 2008.

2.9 MAX-DOAS Measurements During the CINDI-2 Campaign

Z. Wang, N. Hao, C. Zhang (USTC), K. L. Chan (LMU)

Fig. 2-21: The observation platform during the campaign.

Fig. 2-22: View of the instruments.

The CINDI-2 Campaign (2nd Cabauw Intercomparison campaign for Nitrogen Dioxide measuring Instruments) took place in Cabauw, The Netherlands at CESAR (Cabauw Experimental Site for Atmospheric Research) from August 25 until October 7, 2016. The campaign was aiming at assessing the consistency of MAX-DOAS slant column density measurements of tropospheric species (NO_2, HCHO, O_3, and O_4) relevant for the validation of future ESA atmospheric Sentinel missions, through coordinated operation of a large number of DOAS instruments (MAX-DOAS, Pandora, LP-DOAS, CE-DOAS, mobile DOAS, etc.) from all over the world (*Hendrick et al. 2016*), see Fig. 2-21.

Our department took part in the campaign, in cooperation with the School of Earth and Space Sciences, USTC (University of Science and Technology of China). Two EnviMeS 1d MAX-DOAS instruments, developed at the Heidelberg University, were operated by us during the campaign (Fig. 2-22). Each instrument consists of one telescope and two spectrometers, one for the UV (300-460 nm) and the other for the VIS (410-550 nm) region. The telescope is driven by a step motor and can scan in vertical direction. The spectrometers measure the spectra of scattered sunlight collected by the telescope. The instruments were installed on the roof of the containers on the CESAR remote sensing platform, about 5 m above ground. CESAR is located in a flat

polder, characterized by farmland, in the middle of The Netherlands, about 20 km from Utrecht and 30 km from Rotterdam.

Differential slant column densities measurement and semi-blind intercomparison

During the campaign, the telescopes of all participating MAX-DOAS instruments were set to point at the same direction (287° WNW). They scanned vertically according to a common schedule during the day time. A routine scanning cycle included the elevation angles of 1°, 2°, 3°, 4°, 5°, 6°, 8°, 15°, 30° and 90° (6 ×). Each scan lasted for 1 min and each cycle took 15 min. Between 11:30 and 11:40 UTC in the noon, the instruments took 10 continuous zenith (90°) scans. The average spectra of these 10 scans were used as the reference spectra in calculating the differential slant column densities (DSCDs) during the entire day.

For a better comparison, there were also common settings for calculating the DSCDs of trace gases from the measured spectra (Table 2-2). We calculated the DSCDs using QDOAS developed by the Royal Belgian Institute for Space Aeronomy (BIRA-IASB). Some other groups used DOASIS or other programs. Every night, all the participants submitted their DSCD results of the entire day to the referee, and the results were then inter-compared by the referee.

Band	UV			VIS			Reference
Target species	O_4 and NO_2	O_3	HCHO	O_4 and NO_2	NO_2	O_3	
Wavelength range (nm)	338-370	320-340	336.5-359	425-490	411-445	450-520	
NO_2 (298 K)	×	×	×	×	×	×	Vandaele et al. (1998)
NO_2 (220 K)	×			×	×	×	
O_3 (223 K)	×	×	×	×	×	×	Serdyuchenko et al. (2014)
O_3 (243 K)	×		×				
O_3 (293 K)		×				×	
O_3 non-linear correction terms		×					Puķīte et al. (2010)
O_4 (293 K)	×		×	×	×	×	Thalman and Volkamer (2013)
HCHO (297 K)	×	×	×				Meller and Moortgat (2000)
BrO (223 K)	×		×				Fleischmann et al. (2004)
H_2O				×	×	×	Rothman et al. (2010)
Ring	×	×	×	×	×	×	Chance and Spurr (1997)
Polynomial degree	Order 5	Order 3	Order 5	Order 5	Order 4	Order 5	
Intensity offset	Constant	Order 1	Order 1	Constant	Constant	Order 1	

Table 2-2: Common settings for DSCD calculation (*Hendrick et al. 2016*).

Fig. 2-23 shows the comparison of the DSCD results from different instruments. After a few days optimizing, the consistency between the instruments had been improved, the consistency of O_3, O_4 and NO_2 DSCDs was good, but the uncertainty of HCHO results was still large.

Vertical profiles of aerosol and trace gases retrieval

The vertical profiles of aerosol were retrieved from the DSCDs of O_4 and then the profiles of trace gases were retrieved from the aerosol profiles and the DSCDs of trace gases. Our retrieval used the bePRO algorithm developed at BIRA-IASB. It is based on the optimal estimation method and includes the LIDORT radiative transfer model as the forward model. Fig. 2-24 illustrates the retrieval results of September 27, 2016. The aerosol load during that day was mostly low before 14:00 UTC. After 14:00 UTC there were some broken clouds resulting in some differences between the aerosol profiles retrieved from the two bands. As for NO_2, it can be seen that the results of the two bands were quite similar.
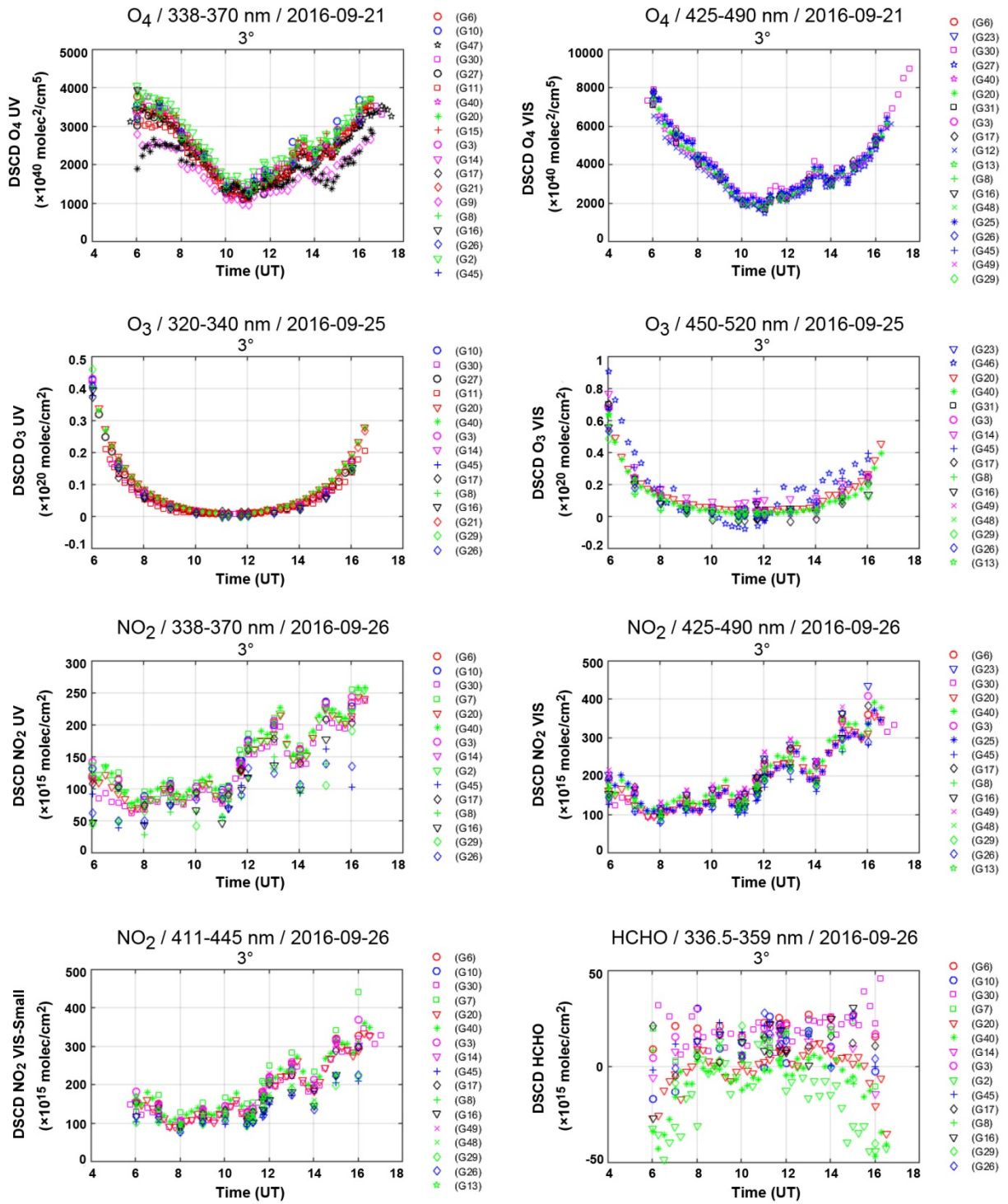
Fig. 2-23: Examples of the intercomparison of DSCDs measured by different instruments.
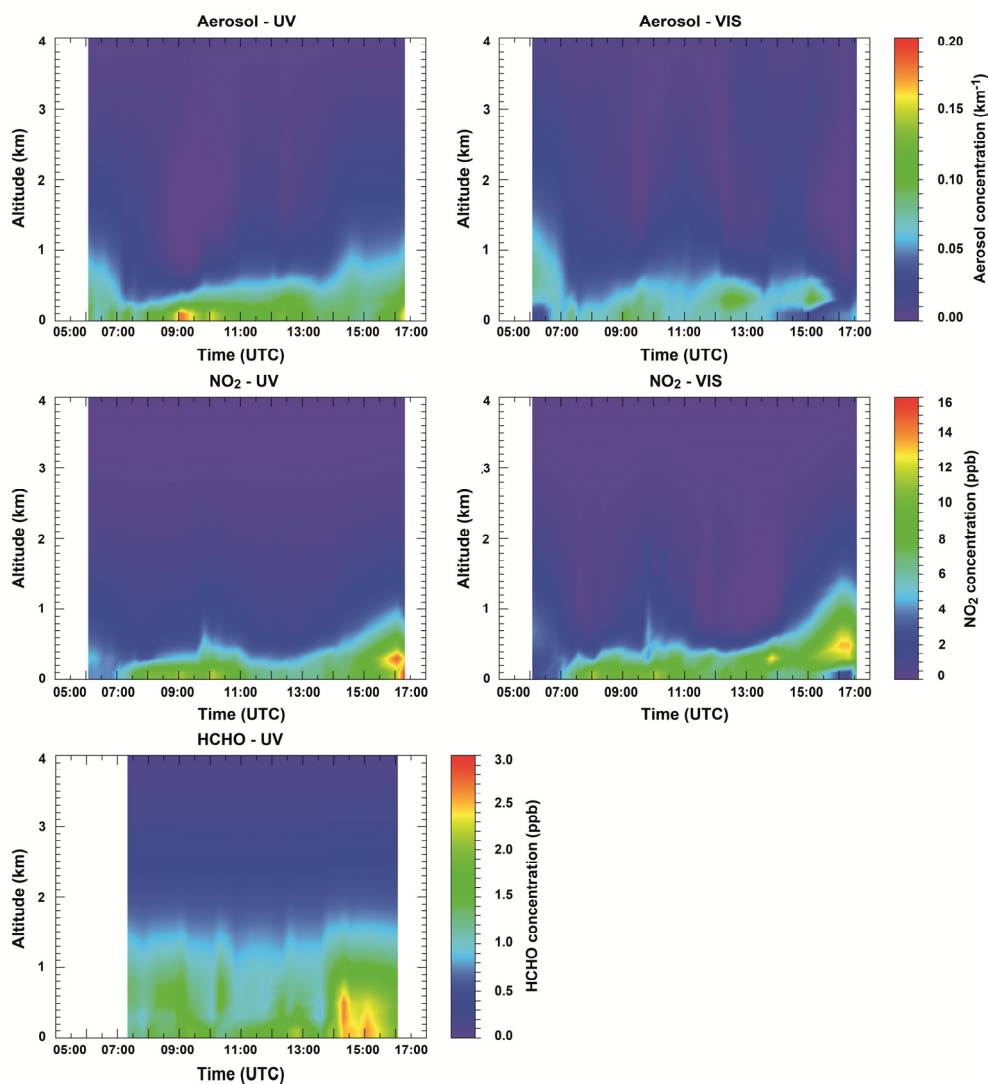
Fig. 2-24: Vertical profiles of aerosol, HCHO and NO₂ on September 27, 2016, retrieved from the data measured by one of our instruments.

References

Chance, K. and Spurr, R.J.D.: Ring effect studies: Rayleigh scattering, including molecular parameters for rotational Raman scattering and the Fraunhofer spectrum. Applied Optics, 36, 5224-5230, 1997.

Fleischmann, O.C., Hartmann, M., Burrows, J.P., and Orphal, J.: New ultraviolet absorption cross-sections of BrO at atmospheric temperatures measured by a time-windowing Fourier transform spectroscopy. J. Photochem. Photobiol. A.: Chem., 168, 117-132, 2004.

Hendrick, F., Van Roozendael, M., Apituley, A., Richter, A., Wagner, T., Friess, U., Kreher, K.: CINDI-2 Semi-blind Intercomparison Protocol, 2016.

Meller, R. and Moortgat, G.K.: Temperature dependence of the absorption cross sections of formaldehyde between 223 and 323 K in the wavelength range 225–375 nm. J. Geophys. Res., 105, 7089-7101, 2000.

Puķīte, J., Kühl, S., Deutschmann, T., Platt, U., and Wagner, T.: Extending differential optical absorption spectroscopy for limb measurements in the UV. Atmos. Meas. Tech., 3, 1155-1174, 2010.

Rothman, L.S., Gordon, I.E., Barber, R.J., Dothe, H., Gamache, R.R., et al.: HITEMP, the high-temperature molecular spectroscopic database. J. Quant. Spectrosc. Radiat. Transfer, 111, 2139-2150, 2010.

Serdyuchenko, A., Gorshelev, V., Weber, M., Chehade, W., and Burrows, J.P.: High spectral resolution ozone absorption cross-sections – Part 2: Temperature dependence. Atmos. Meas. Tech., 7, 625-636, 2014.

Thalman, R., and Volkamer, R.: Temperature dependent absorption cross-sections of O_2-O_2 collision pairs between 340 and 630 nm and at atmospherically relevant pressure. Phys. Chem. Chem. Phys., 15, 15371-15381, 2013.

Vandaele, A.C., Hermans, C., Simon, P.C., Carleer, M., Colin, R., et al.: Measurements of the NO_2 absorption cross-section from 42,000 cm^{-1} to 10,000 cm^{-1} (238-1000 nm) at 220 K and 294 K. J. Quant. Spectrosc. Radiat. Transfer, 59, 171-184, 1998.

3.   Atmospheric Remote Sensing – Methods

3.1   Operational Atmospheric Composition SAF Trace Gas Column Products from GOME-2

P. Valks, N. Hao, P. Hedelt, M. Grossi, S. Liu, K.-P. Heue, R. Lutz, S. Gimeno García, D. Loyola

The operational GOME-2 trace gas column and cloud products from MetOp-A and MetOp-B are provided by IMF-ATP in the framework of EUMETSAT's Satellite Application Facility on Atmospheric Composition Monitoring (AC SAF – *Hassinen et al. 2016*), formerly known as Ozone Monitoring SAF (O3M SAF). The AC SAF trace gas column products are generated operationally at DLR using the GOME Data Processor (GDP), and are used in the near real time (NRT) system of the Copernicus Atmospheric Monitoring Service (CAMS). The current GOME-2 trace gas products include total ozone, total and tropospheric NO_2, SO_2, BrO, formaldehyde (HCHO) and water vapor. In 2016, the new GDP version 4.8 has become operational, and the GOME-2 trace gas column products have been reprocessed for the complete MetOp-A and -B missions (*Valks et al. 2016*).

In the last year of the second Continuous Development and Operation Phase (CDOP-2) of the AC SAF, the focus was on the development of new GOME-2 trace gas products, including OClO and glyoxal columns, as well as NO_2 and water vapor climate products.

GOME-2 OClO columns

An improved OClO retrieval algorithm for both GOME-2A and -B has been developed within the framework of an O3M SAF Visiting Scientist project (*Richter et al. 2015*). The DOAS retrieval is performed in the UV wavelength range 345-389 nm to reduce bias and noise in the OClO slant columns. As correction for residual polarization errors in the level 1 product, the GOME-2 key data parameter *Eta* is fitted as another effective cross-section. Including *Eta* significantly improves the fitting residuals of the OClO fit in the large fitting window. Furthermore, two empirical correction functions (derived from mean DOAS fit residuals) are included as additional (pseudo-)absorption cross-sections in the DOAS fit for GOME-2: a mean residual and a scan angle correction function. These two empirical functions correct for positive offsets and scan angle dependences in the OClO columns. With the improved DOAS algorithm described above, the quality of the GOME-2 OClO columns is clearly superior to the demonstrational results in the CDOP-1. However, an additional offset correction is still needed to account for remaining biases in the OClO columns (e.g. non-zero OClO columns over areas without chlorine activation), the temporal drifts observed mainly in the OClO data from GOME-2A. To that end, a simple but effective normalization is applied on an orbital basis.
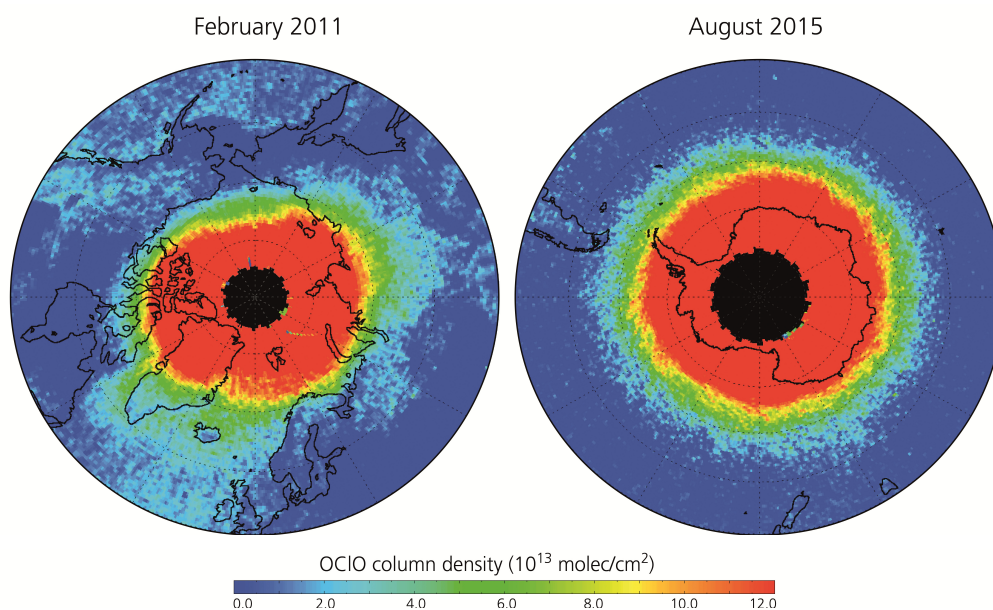

Fig. 3-1: OClO columns over the North Polar region in February 2011 and over the South Polar region in August 2015 based on data from GOME-2A and GOME-2B.

OClO can only be observed at large solar zenith angle and under these circumstances the calculation of an AMF and a vertical column is not useful. Therefore, the GOME-2 data product will only contain (corrected) slant columns of OClO. The offline GOME-2 OClO columns are expected to become operational in the first quarter of 2017 (Fig. 3-1).

GOME-2 NO$_2$ and H$_2$O climate products

In 2016, the new GOME-2 NO$_2$ and water vapor level 3 climate products have been reviewed (*Grossi et al. 2016*). These products contain global monthly mean total and tropospheric NO$_2$ and water vapor columns. An area-weighted gridding algorithm is used for the generation of the level 3 monthly mean products that takes as input the level 2 reprocessed GOME-2 NO$_2$ and H$_2$O column data generated with the GDP (see above). Each level 3 product is produced at a spatial resolution of 0.25° × 0.25° for NO$_2$ and 0.5° × 0.5° for H$_2$O, from the complete set of level 2 orbit files that span a particular month. In addition, a number of statistical summaries and uncertainty estimates are computed for each of these level 3 products, and auxiliary surface and cloud parameters are provided. All level 3 GOME-2 atmospheric products data are organized into user-friendly and self-describing netCDF-4 files, based upon the platform (MetOp-A or MetOp-B).

The monthly level 3 NO$_2$ and water vapor column products from GOME-2 are generated with consolidated algorithms applied in a consistent way to homogeneous (reprocessed) level 1 Fundamental Climate Data Records (FCDR), which qualifies them as Thematic Climate Data Records (TCDRs).

References

Grossi, M., Valks, P., and Liu, S.: Algorithm Theoretical Basis Document for GOME-2 NO$_2$ and H$_2$O Level 3 Climate Products, SAF/O3M/DLR/ATBD/Clim, 2016.

Hassinen, S., Balis, D., Bauer, H., Begoin, M., Delcloo, A., Eleftheratos, K., Gimeno García, S., Granville, J., Grossi, M., Hao, N., Hedelt, P., Hendrick, F., Hess, M.l, Heue, K.-P., Hovila, J., Jønch-Sørensen, H., Kalakoski, N., Kauppi, A., Kiemle, S., Kins, L., Koukouli, M., Kujanpää, J., Lambert, J.-C., Lang, R., Lerot, C., Loyola, D., Pedergnana, M., Pinardi, G., Romahn, F., Van Roozendael, M.l, Lutz, R., De Smedt, I., Stammes, P., Steinbrecht, W., Tamminen, J., Theys, N., Tilstra, L.G., Tuinder, O., Valks, P., Zerefos, C.S., Zimmer, W., Zyrichidou, I.: Overview of the O3M SAF GOME-2 operational atmospheric composition and UV radiation data products and data availability. Atmos. Meas. Tech., 9 (2), 383-407, DOI: 10.5194/amt-9-383-2016, 2016.

Richter, A., Wittrock, F., P. Valks, P.: Evaluation of the possibility to derive reliable OClO slant columns from GOME2b and GOME2a spectra, Visiting Scientist Report, SAF/O3M/IUP/OClO/2, Issue 1, November, 2015.

Valks, P., Loyola, D., Hao, N., Hedelt,P., Slijkhuis, S., Grossi, M., Begoin, M., Gimeno García, S., Lutz, R.: Algorithm Theoretical Basis Document for GOME-2 Total Column Products of Ozone, Minor Trace Gases and Cloud Properties (GDP 4.8 for O3M-SAF OTO and NTO), DLR/GOME-2/ATBD/01, Issue 3, Rev. A, October, 2016.

3.2 Improvement of Total and Tropospheric NO$_2$ Column Retrieval for GOME-2

S. Liu, P. Valks

Nitrogen dioxide (NO$_2$) is an important trace gas in the atmosphere. Over remote regions most of the NO$_2$ is located in the stratosphere, while for polluted hot spots it is primarily located in the troposphere and regarded as an important air pollutant. The Global Ozone Monitoring Experiment (GOME-2) instrument aboard the MetOp satellite platforms provides NO$_2$ measurements on a global scale.

The retrieval of total and tropospheric NO$_2$ column for GOME-2 consists of several steps (*Valks et al. 2011*). First, the differential optical absorption spectroscopy (DOAS) method is applied to determine the NO$_2$ slant columns from GOME-2 in the visible wavelength region. Then initial total NO$_2$ vertical columns are calculated by an air mass factor (AMF) conversion using the LIDORT model and a stratospheric NO$_2$ climatology. To estimate the stratospheric component, a spatial filtering algorithm is applied. Tropospheric air mass factors are computed using monthly averaged NO$_2$ profiles from a 3-D chemistry transport model, and the tropospheric NO$_2$ columns can be determined.

The algorithm improvement focuses on three parts of the retrieval. First, the retrieval of the NO$_2$ slant columns for GOME-2 is performed with the DOAS method in an extended wavelength region (425-497 nm), using updated cross-sections of NO$_2$, water vapor, O$_3$ and O$_4$. To that end, the high-resolution laboratory cross-sections are convolved with the effective GOME-2 slit function. To derive the GOME-2 slit function, a high-resolution reference solar spectrum (*Chance and Kurucz 2010*) is convolved with an asymmetric Gaussian line shape and shifted on the GOME-2 irradiance measurements with the shape and width of the asymmetric Gaussian as fitting parameters. Fig. 3-2 shows the evolution of the fitted GOME-2 slit function width (FWHM).
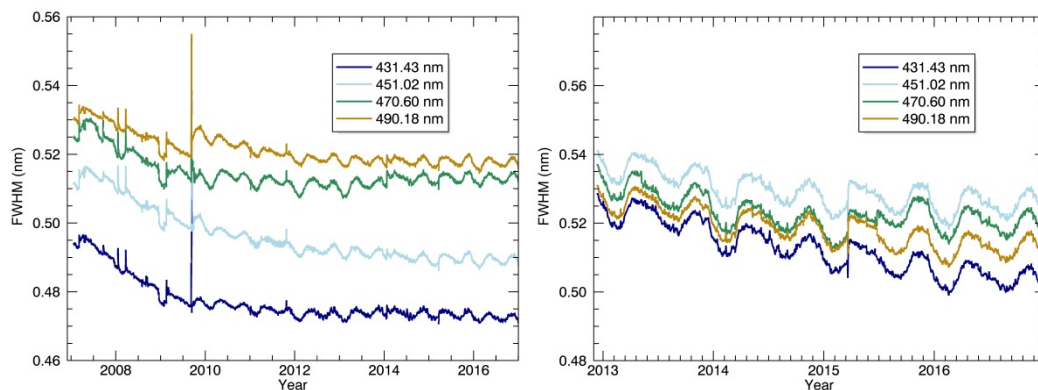
Fig. 3-2: Temporal evolution of the fitted GOME-2 slit function width for GOME-2/MetOp-A (left) and GOME-2/MetOp-B (right).

The retrieved GOME-2 slit functions of both instruments have narrowed after the launch of the instruments in a similar way. A visible seasonal variation (more apparent for GOME-2/MetOp-B) is due to the changing temperature of the optical bench. For GOME-2/MetOp-A, an apparent peak appears in September 2009, when a major throughput test was performed. After the throughput test, the narrowing of slit function width has been slowing down. When applying the effective fitted slit function, the calibration RMS is reduced by about 80% for GOME-2/MetOp-A and 70% for GOME-2/MetOp-B, compared to using the pre-flight (flight model) slit function.

Second, the new Stratospheric Estimation Algorithm from Mainz (STREAM) has been applied to GOME-2 to determine the stratospheric column density of NO$_2$ (*Beirle et al. 2016*). STREAM derives weighting factors for each satellite pixel, which define the contribution from the initial NO$_2$ total columns to the stratospheric field. The stratospheric NO$_2$ component is then derived by weighted convolution and subtracted from the initial total columns to get the tropospheric residues. The tropospheric residues calculated with STREAM and the spatial filtering algorithms are compared in Fig. 3-3.
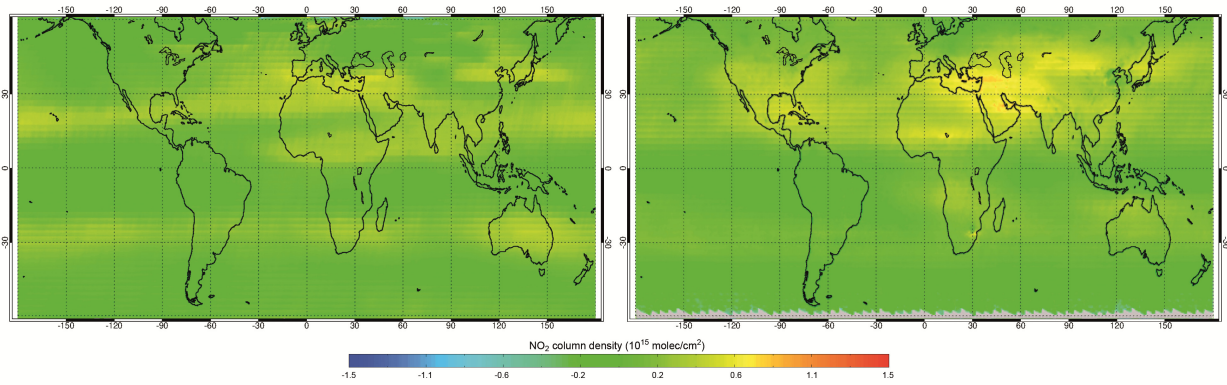
Fig. 3-3: Monthly average difference of NO₂ tropospheric residues from STREAM and the spatial filtering algorithm, measured by GOME-2/MetOp-A in January (left) and July (right) 2008.

The bias in Fig. 3-3 between the tropospheric residues calculated with STREAM and the current spatial filtering algorithm is relatively small above the ocean. In general, the use of STREAM leads to an increase in the tropospheric residues, especially over continents, and this effect is larger in summer.

Third, in the tropospheric AMF calculation, improved a priori NO₂ profiles are obtained from the chemical transport model IMAGES (*Müller and Stavrakou 2005*), instead of the currently used MOZART-2 model. Using simulations performed from the year 2005-2013, the IMAGES model determines the monthly average profiles at the satellite overpass time with a resolution of 2° in latitude and 2.5° in longitude, at 40 layers from the surface to the lower stratosphere. The profile shape has a large effect on the AMF, and hence on the retrieved tropospheric NO₂ columns. Two vertical profiles of NO₂ located in China and Brazil are shown in Fig. 3-4.
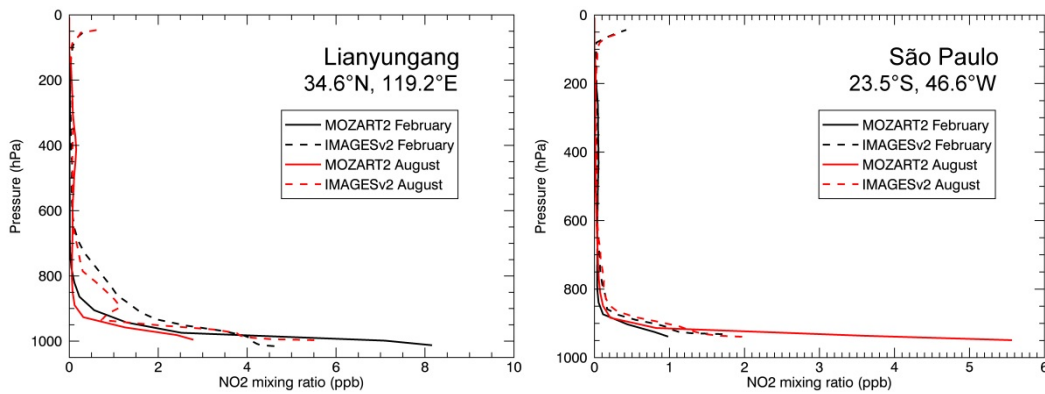
Fig. 3-4: Examples of NO₂ vertical profiles simulated with IMAGES (dotted) and MOZART (solid) model in February (black) and August (red) 2008.
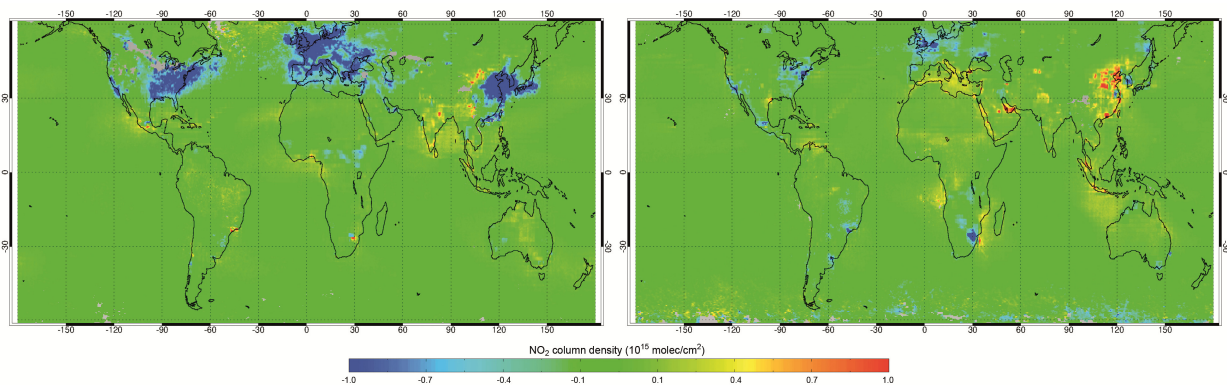
Fig. 3-5: Monthly average difference between tropospheric NO₂ columns retrieved (from GOME-2/MetOp-A data) using IMAGES and MOZART a priori NO₂ profiles in February (left) and August (right) 2008.

Lower surface concentrations are found in winter for IMAGES profiles, and the effect of the NO_2 vertical profiles on the retrieved tropospheric NO_2 columns is illustrated in Fig. 3-5.

The application of the a priori NO_2 profiles from the IMAGES model decreases the tropospheric NO_2 columns by more than 1.0×10^{15} molec/cm^2 over pollution hot spots like US and China in February. Taking Lianyungang (left panel in Fig. 3-4) as an example, lower surface layer concentrations are modelled by IMAGES in February, and therefore a higher sensitivity to tropospheric NO_2 is assumed in the AMF calculation. This results in a decrease in the retrieved tropospheric NO_2 column as shown in Fig. 3-5 (left).

References

Beirle, S., Hörmann, C., Jöckel, P., Penning de Vries, M., Pozzer, A., Sihler, H., Valks, P., and Wagner, T.: The STRatospheric Estimation Algorithm from Mainz (STREAM): Estimating stratospheric NO_2 from nadir-viewing satellites by weighted convolution, Atmos. Meas. Tech. Discuss., doi:10.5194/amt-2015-405, 2016.

Chance, K. and Kurucz, R.L.: An improved high-resolution solar reference spectrum for earth's atmosphere measurements in the ultraviolet, visible, and near infrared, J. Quant. Spectrosc. Radiat. Transf., 111, 1289-1295, 2010.

Müller, J.-F. and Stavrakou, T.: Inversion of CO and NOx emissions using the adjoint of the IMAGES model, Atmos. Chem. Phys., 5, 1157-1186, 2005.

Valks, P., Pinardi, G., Richter, A., Lambert, J.-C., Hao, N., Loyola, D., Van Roozendael, M., Emmadi, S.: Operational total and tropospheric NO_2 column retrieval for GOME-2, Atmos. Meas. Tech., 4, 1491-1514, 2011.

3.3 Validation of Carbon Monoxide Vertical Column Densities from SCIAMACHY Infrared Nadir Observations

P. Hochstaffl, F. Schreier

Based on the Master's Thesis "Validation of Carbon Monoxide Vertical Column Densities Retrieved from SCIAMACHY Infrared Nadir Observations" (*Hochstaffl 2015*) new and advanced methods as well as improvements in harmonizing both, ground-based and SCIAMACHY, datasets for comparison have been studied and implemented. The result is a compilation of Python command-line tools which provide well-defined interfaces to underlying modules in terms of optional parameters and input/output elements. This warrants that the processing steps from the original level 2 retrieval output towards a final comparable product is well documented with respect to the created output and log files. In addition, it ensures that results are reproducible in the interest of good scientific practice.

Modifications implemented
The comparison of CO total columns estimated from SCIAMACHY SWIR channel 8 using the Beer Infrared Retrieval Algorithm (BIRRA, prototype version) to NDACC vertical columns has been shifted, with respect to the Master's thesis, from vertical column densities (VCDs) to dry-air volume mixing ratios (VMRs) as the latter is less sensitive to differences in ground height. Especially over complex terrain environments such as the Alps, this approach is expected to lead to more accurate results as large horizontal altitude gradients are smoothed in the elevation model utilized in the SCIAMACHY level 2 retrieval. The comparison can be performed on any temporal and spatial scale. Moreover, the common approach of comparing measurements within a certain latitude/longitude range has been modified to the comparison of observations within a given great-circle distance. In addition, an inverse temporal and distance weighting algorithm can be applied on measurements within that circle with respect to its acquisition time and its center latitude/longitude – in general collocated with the ground-based (g/b) site.

Many previous studies by different authors (*De Laat et al. 2010*, *Dils et al. 2006*, *Sussmann and Buchwitz 2005*, *Gimeno García et al. 2011*), including the Master's Thesis (*Hochstaffl 2015*), pointed out that the retrieval (especially CO) from SCIAMACHY observations is challenging due to the

degrading performance of channel 8. In order to mitigate this issue, multiannual averaging of both, g/b and satellite-based (s/b) data, was pursued. When comparing independent datasets (mean, correlation etc.) on large temporal scales (with respect to its periodicity of about one year) the removal of linear trends from data is recommended. More specifically (almost) the full-mission SCIAMACHY dataset (and g/b) ranging from 2003 to 2011 had been taken, de-trended, averaged on a monthly basis, distance weighted (optional) and merged to one year (comprising data from nine years). The advantage of this approach is that even for years of bad instrument performance the same demanding filter requirements can be applied in level 2 post-processing mitigating the risk of including bad data for comparison while at the same time allowing for a statistically sufficient amount of data within each temporal interval.
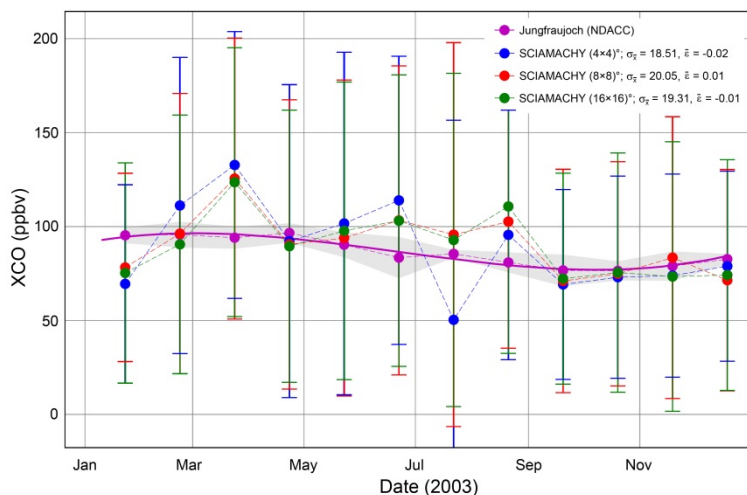
Fig. 3-6: SCIAMACHY dry-air CO VMR's selected within a given (latitude × longitude) area and observations from Jungfraujoch (NDACC) in 2003. Standard error $\sigma_{\bar{x}}$ and relative deviation $\bar{\varepsilon}$ is specified in the corresponding legend.
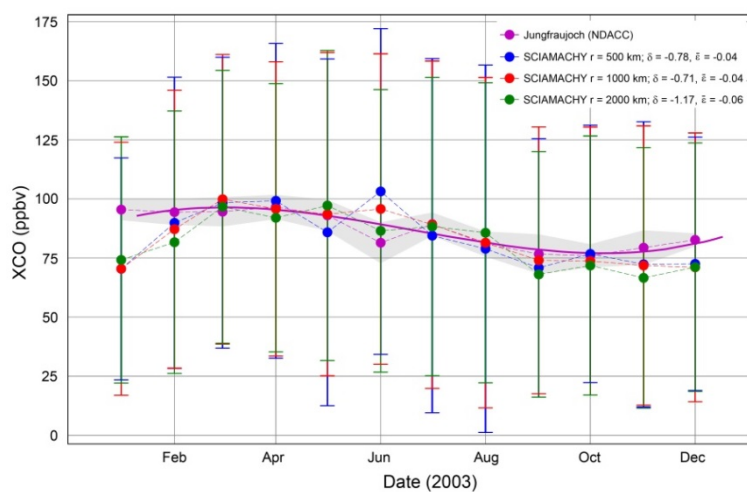
Fig. 3-7: Instead of VMRs selected within a given latitude and longitude, the selection presented here is based on great circle distance from the Jungfraujoch g/b reference site. δ is the weighted sum over the residuals within each time interval.
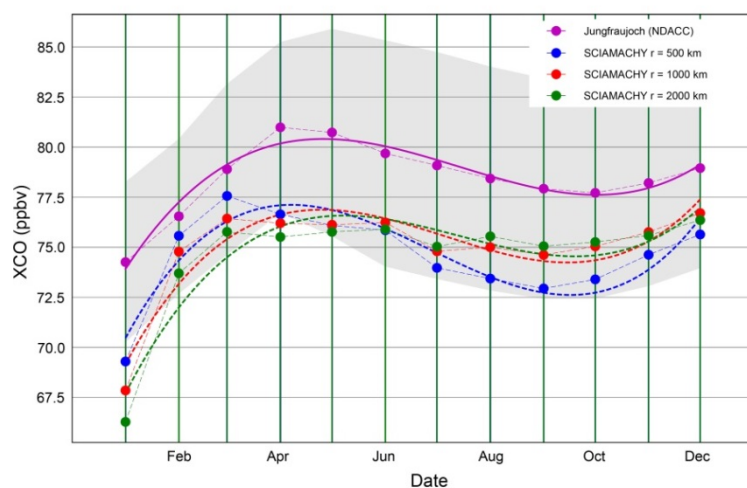
Fig. 3-8: SCIAMACHY and NDACC dry-air VMRs ranging from 2003 to 2011, averaged on a monthly basis and merged to one year, for various sized sampling areas.

34

Results

Fig. 3-6 and Fig. 3-7 reveal that comparing s/b observations within a given great-circle distance from the reference site provides smoother and more representative results compared to a latitude/longitude selection with respect to Jungfraujoch. A very small bias is present but this small offset depends on the selected SCIAMACHY observations. Furthermore, the 30 days – respectively one month – temporal average appeals to deliver the best results for reasonably sized sampling area. Fig. 3-8 shows that proper post processing, particularly filtering, and adequate averaging techniques enable successful retrieval within the g/b standard deviation of SCIAMACHY CO total columns for the whole mission.

References

Dils, B., De Mazière, M., Müller, J.F., et al.: Comparisons between SCIAMACHY and ground-based FTIR data for total columns of CO, CH₄, CO₂ and N₂O. Atmos. Chem. Phys., 6, 1953-1976, doi:10.5194/acp-6-1953-2006, 2006.

Gimeno García, S., Schreier, F., Lichtenberg, G., and Slijkhuis, S.: Near infrared nadir retrieval of vertical column densities: methodology and application to SCIAMACHY. Atmos. Meas. Tech., 4, 2633–2657, doi:10.5194/amt-4-2633-2011, 2011.

Hochstaffl, P.: Validation of Carbon Monoxide Total Columns from SCIAMACHY Near Infrared Nadir Spectra with NDACC/TCCON Ground-Based Measurements. Master thesis, University of Innsbruck, 145 pp, 2015.

*De Laat, A.T.J., Gloudemans, A.M.S., Schrijver, H., et al.*: Validation of five years (2003-2007) of SCIAMACHY CO total column measurements using ground-based spectrometer observations. Atmos. Meas. Tech., 3, 1457-1471, doi:10.5194/amt-3-1457-2010, 2010.

Sussmann, R., and Buchwitz, M.: Initial validation of ENVISAT/SCIAMACHY columnar CO by FTIR profile retrievals at the Ground-Truthing Station Zugspitze. Atmos. Chem. Phys., 5, 1497-1503, doi:10.5194/acp-5-1497-2005, 2005.

3.4   Adapting the OCRA Cloud Fraction Algorithm to the Geostationary Sentinel-4 Mission

R. Lutz, D. Loyola, F. Romahn, S. Gimeno García

The cloud fraction determination in the UVN spectral range with the Optical Cloud Recognition Algorithm (OCRA) has been successfully applied to and operationally used for several instruments like GOME on ERS-2 or GOME-2 on Met-Op A/B. For these heritage instruments, the Polarization Measurement Devices (PMDs) have been used to provide broad band reflectance measurements which have been transformed to color information needed for the OCRA color space approach to calculate the radiometric cloud fraction; for details see *Lutz et al. (2016)*. Subsequently, OCRA has also been adapted to the OMI instrument aboard Aura using a modified two-color approach and, based on these experiences, OCRA will also be used operationally for the soon to be launched TROPOMI instrument on Sentinel-5 Precursor. All these instruments/missions mentioned above have in common that they are flying in low-earth polar orbits, i.e. the illumination conditions (specifically the solar zenith angle – SZA) for a fixed location from one overpass to the next are more or less constant with only smaller variations throughout the year. Also the viewing zenith angles (VZA) are, depending on the instrument's swath width, not too large with values usually going up to roughly 60°.

The situation changes for a geostationary orbit. Since OCRA will also be used operationally for the UVN instrument on the geostationary Sentinel-4 platform, it has to be considered that for a fixed location there is a strong diurnal variation in the solar zenith angle. The Sentinel-4 field of view will focus on central Europe, covering latitudes from roughly 30° N (North Africa, Sahara) up to 65° N (Scandinavia). This corresponds to relatively low viewing zenith angles for the lower latitudes, but VZA values above 60° are already reached for e.g. Northern Germany. For any algorithm based on the heritage polar missions it is therefore important to investigate the behavior under more extreme observational geometries as imposed by the geostationary orbit.

The presence of a cloud-free reflectance composite map is a pre-requisite for the OCRA algorithm. For

the polar-orbiting missions, these composite maps were generated on a monthly basis in order to cover the seasonal changes in the surface conditions (mainly due to snow coverage). In the geostationary case, these monthly maps have been refined to an hourly temporal resolution in order to cover the diurnal change of the SZA. Since the launch of Sentinel-4 still has to await a few years, OCRA has been adapted in a first step to the geostationary SEVIRI instrument.

A comparison of a false-color image with the retrieved OCRA cloud fraction is shown in the panels of Fig. 3-9. In the bottom panel, all regions with SZA > 90° are depicted in grey. As can be seen, the performance of OCRA is very well also for high VZA at high northern latitudes. No trends are visible in the latitudinal direction. However, difficulties manifested by a white "band" of erroneous large cloud fractions appear for geolocations close to the terminator (grey edge). Still, the OCRA retrieval seems to be stable even under twilight conditions with SZAs up to 80-85°. Although this first visible inspection seems quite promising, a more detailed study has to be performed in order to further consolidate the adaptation of OCRA to the geostationary geometry, with special emphasis on high VZA and high SZA as applicable in twilight or low illumination conditions.
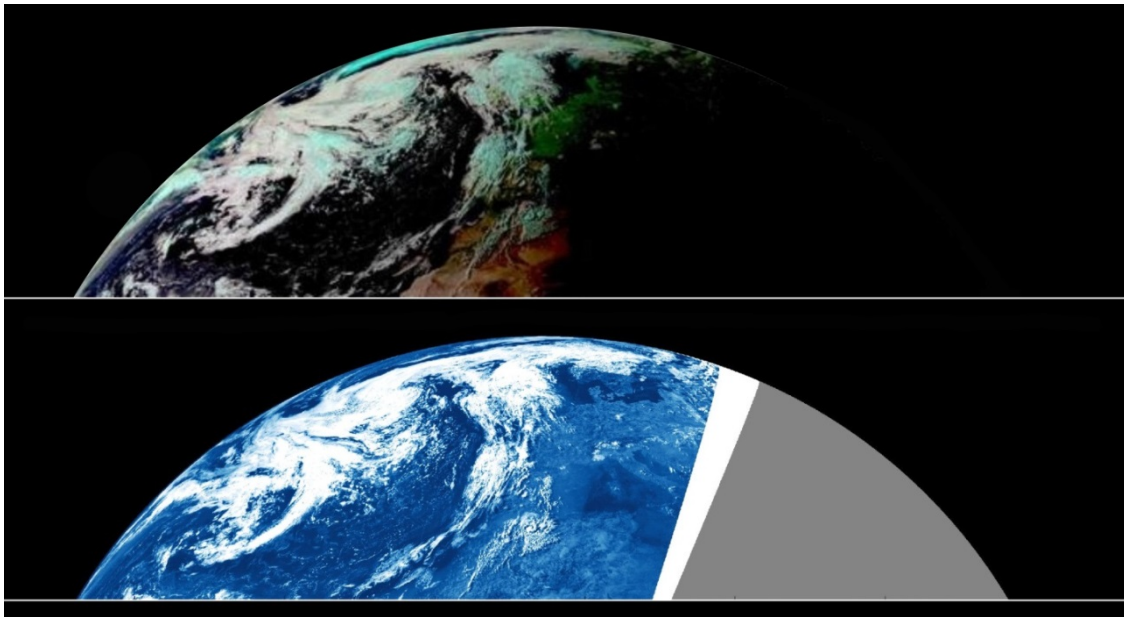
Fig. 3-9: Top: SEVIRI false-color composite image for July 1, 2015, 18:00 UT (image: http://www.icare.univ-lille1.fr/browse/geoview.php). Bottom: SEVIRI cloud fraction from OCRA for July 1, 2015, 18:00 UT.

References

Lutz, R., Loyola, D., Gimeno García, S., Romahn, F.: OCRA radiometric cloud fractions for GOME-2 on MetOp-A/B. Atmos. Meas. Tech., 9, 2357-2379. DOI: 10.5194/amt-9-2357-2016, 2016.

3.5 New UPAS-2 Configuration Concept

F. Romahn, W. Zimmer, H. Bauer, M. Pedergnana

Since the start of its development in 2013, the UPAS-2 processor (Universal Processor for UV/VIS Atmospheric Spectrometers) has become more and more sophisticated over time. A milestone was reached end of 2016 when UPAS-2 was delivered to ESA as the operational processor for the cloud, O_3, HCHO and SO_2 products for the Sentinel-5 Precursor (S5P) mission. Regardless of this success, the development of UPAS-2 is far from over, as it was planned from the beginning that this processor could basically handle an arbitrary number of products and sensors and thereby replace the outdated UPAS processor, which is, however, still operational for some missions. So far, it is able to process GOME-2 data for various products in the context of the Atmospheric Composition Monitoring SAF (AC SAF) as well as cloud and O_3 products for GOME. UPAS-2 will also be used to provide products for the Sentinel-4 mission. Support for SCIAMACHY data in the future is planned as well.

This high flexibility requires that UPAS-2 can be accurately configured for every specific sensor and product it supports. So far, this requirement is only implemented by some command-line options while most of the configuration is specified directly in the source code which can make changes quite cumbersome.

Therefore, over the last months, a new configuration concept for UPAS-2 was designed and is now currently implemented. After an analysis of the current situation in UPAS-2 as well as the UPAS configuration management, the following key aspects of the new concept were identified: Easy extensibility, error proneness and particularly ease of use. The developed configuration concept that addresses those issues is shown in Fig. 3-10.
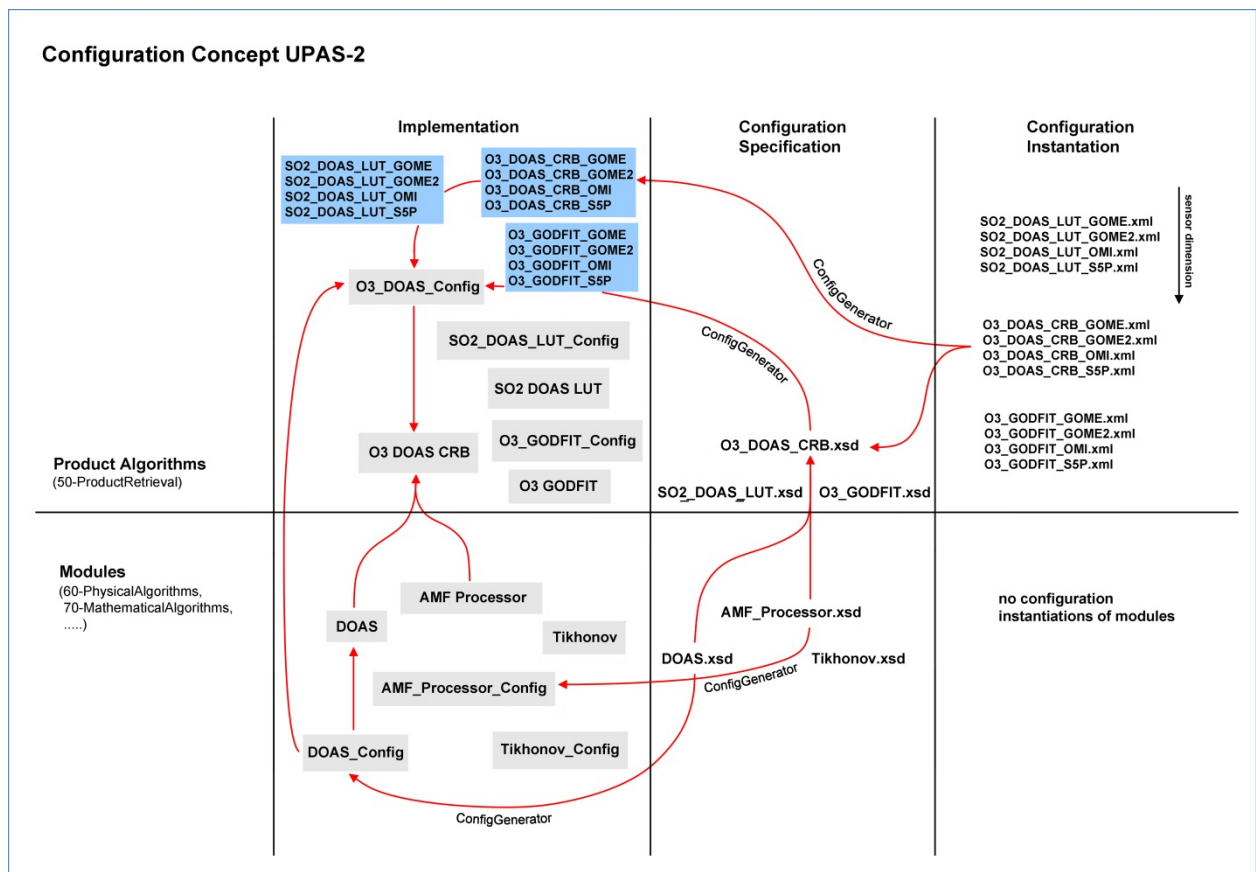
Fig. 3-10: The new configuration concept for UPAS-2.

For each possible combination of a product and a sensor, a default configuration is specified by an xml-file (e.g. "O3_DOAS_CRB_S5P.xml"). Those configurations are described by so-called "xml-schemas (xsd)", that specify their exact structure. For every configurable part in UPAS-2 there is such a schema that can also include other schemas to reflect the hierarchical structure in the source-code. Additionally

to the structure of the configuration, a schema can also define certain restrictions, e.g. to prohibit invalid values for parameters. Every configuration (xml) that is then used by UPAS-2 will always be checked against the corresponding schema (xsd) for validity thus preventing invalid configurations from the very beginning. There is a number of tools (e.g. in Eclipse) that allow easy editing of the xsd- and xml-files. These tools can also generate xml- from the xsd-files. The link between the schema and configuration files and UPAS-2 is finally realized by a Python-script, the ConfigGenerator. This script reads the xsd- and xml-files, checks the validity of the configurations and automatically generates the C++ source code that implements the corresponding configuration-classes and objects. Thus all default configurations for the different sensors and products are implemented in the UPAS-2 binary, as well as methods to write those configurations or read other ones. The ConfigGenerator provides the required ease of extensibility, as it is no longer necessary to modify the source code when the configurations (or their structure) have to be changed. Editing the appropriate configurations or schemas is sufficient. Finally, in order to use a configuration different from the default one, a specific configuration can be provided to UPAS-2 via the command-line. This configuration is then read and will, if valid, replace the internal default configuration. In order to get a valid configuration in the first place, UPAS-2 will also provide a command-line option to write out the default configuration. If needed, the user can then modify this configuration and provide it to UPAS-2 again, i.e. small changes to the default configuration can be realized very fast and conveniently.

Currently, the ConfigGenerator already generates valid source code from the configurations and configuration schemas. This was one of the biggest implementation challenges. Further testing and refinement is still required. However it is planned to finish the implementation of the new UPAS-2 configuration concept during January 2017. Thus one of the last missing building blocks of the UPAS-2 processor will be completed.

3.6   ADM-Aeolus Mie and Rayleigh Algorithm Performance Assessment

K. Schmidt, O. Reitebuch (IPA), D. Huber (DoRIT)

The main goal of the ESA ADM-Aeolus mission consists in the acquisition of global vertical wind profiles from space using Lidar technology to improve the accuracy of weather and climate prediction. The Aeolus satellite will carry a Doppler wind Lidar, called ALADIN (Atmospheric Laser Doppler Instrument), which will probe the lowermost 30 km of the atmosphere at a wavelength of 355 nm. It will measure Doppler shifts in the spectra of the laser light backscattered by moving atmospheric particles such as aerosols, cloud particles, and air molecules. Therefore both a Mie and a Rayleigh spectrometer are used and line-of-sight wind velocities can be derived. The launch is scheduled between November 2017 and January 2018.

Our involvement concerns investigations on the impact of different ALADIN instrument settings and atmospheric scenes on the performance of the Mie and Rayleigh wind results. The atmospheric scenarios under consideration range from ideal constant via variable synthetic to realistic measured conditions. Recommendations for further algorithm refinements and quality control have been derived. A corresponding technical note (*Schmidt et al. 2016*), summarizing the results and recommendations, has been completed and submitted to ESA in 2016.

We used the ADM-Aeolus End-to-End Simulator (E2S – see also chapter 3.7) for simulating the measurement flow for different atmospheric scenarios including wind conditions. Annotated instrument source packet data, suitable for L0-L1a-L1b processing, are the output of these simulations. Comparisons between the input and the resulting L1b Mie and Rayleigh channel winds allow assessing the algorithms and parameter settings.

Fig. 3-11 shows an example of such investigations. It has been obtained for a radiosonde data set measured by KNMI. The radiosonde was launched in De Bilt, The Netherlands, on December 25, 2007 at 12:00 UTC. The profiles of the wind velocity, temperature, pressure, and aerosol and cloud extinction and backscatter coefficients have a very high sampling resolution of 10 m. The maximum altitude of the balloon was 24.175 km so that no data are available beyond this height. The data set has been filled up by KNMI with constant values in the altitude range between 24.185 km and 39.995 km. Note that the

measured wind profiles have strong gradients (see black line on the left hand side of Fig. 3-11). Note furthermore that three clouds were present having a total optical thickness of nearly 0.8. This optical thickness was increased to 0.85 by aerosols additionally present in the cloud region. The maxima of the aerosol extinction and backscatter coefficients were, however, in the lower altitude range of about 0 km to 3 km so that significant Mie channel signals are also obtained here (see *Schmidt et al. 2016* for more details on the atmospheric conditions and instrument settings).
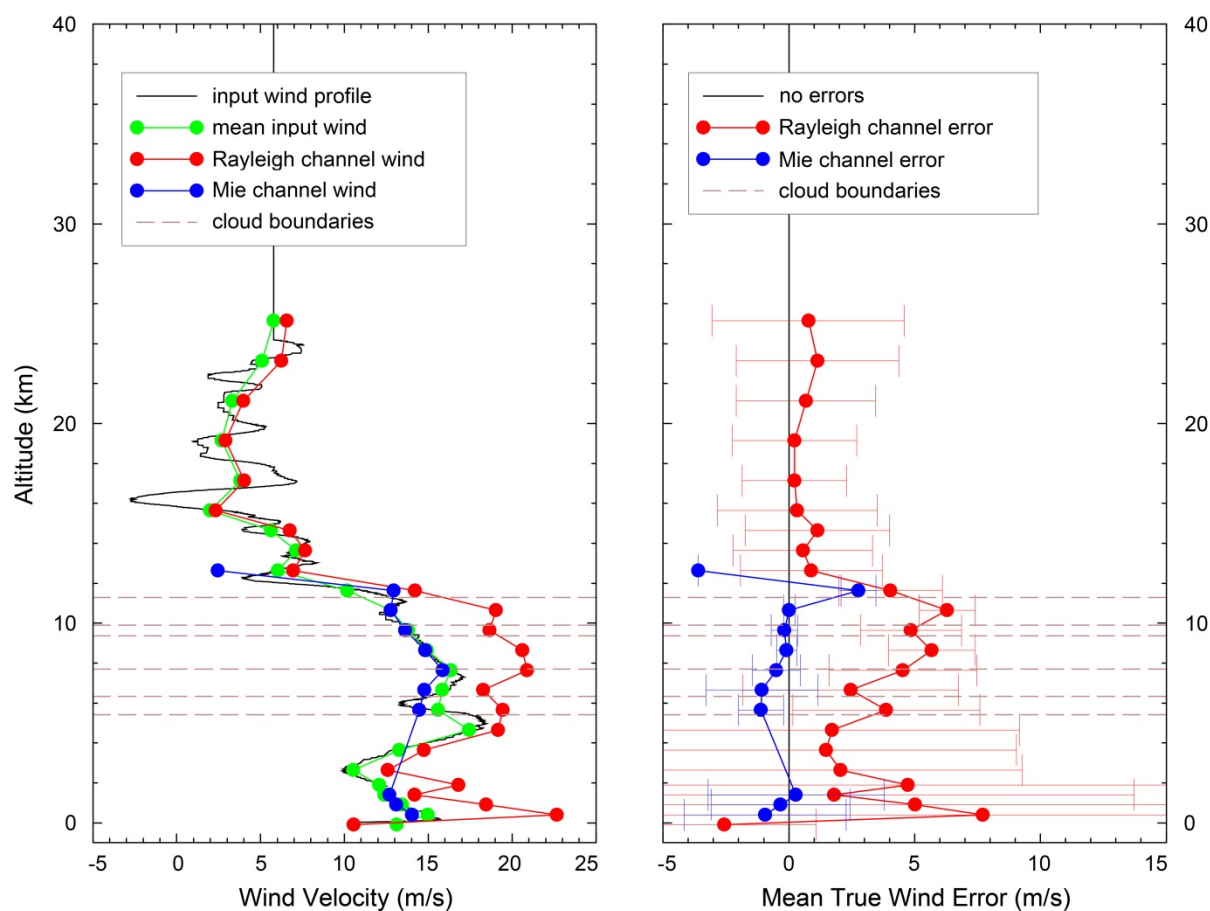
Fig. 3-11: Left: Comparison of the mean Rayleigh (red line) and Mie channel wind profile (blue line), obtained by an (E2S V.3.05 + L1bP V.6.04) simulation, with the input KNMI radiosonde wind velocity profile (black line) and its corresponding mean profile (green line) obtained by averaging over all radiosonde wind values in each L1bP height bin. Right: Obtained mean true wind errors including their standard deviations as error bars. The altitude ranges of the clouds, considered in the simulations, are marked by greyish dashed lines.

Fig. 3-11 demonstrates that reliable L1b Rayleigh channel wind results are obtained above the clouds in the absence of aerosol and cloud particles. Here, the Rayleigh winds (red line) follow the trend of the mean input wind profile (green line). The corresponding mean true wind errors are ≤ 1.1 m/s (see right panel of Fig. 3-11). Larger differences between the L1b Rayleigh winds and the mean KNMI wind profile are seen in and below the clouds (left panel of Fig. 3-11). They are mainly due to the contamination of the Rayleigh channel by the signals of larger aerosol and cloud particles and by the extinction of the Rayleigh signals coming from below the clouds. These discrepancies are seen as large errors in the right panel of Fig. 3-11. On the other hand, the strong aerosol and cloud particle backscattering leads to reliable Mie channel wind results with relatively small errors (blue lines in Fig. 3-11). That means that an appropriate combination of the Rayleigh and Mie channel results reproduces the input radiosonde wind profile.

References

Schmidt, K., Reitebuch, O., and Huber, D.: Technical Note 51.2: Mie and Rayleigh Algorithm Performance Assessment, AE.TN.DLR.5100.2.20161121, V.1.2, 21.11.2016, 2016.

3.7 ADM-Aeolus End-to-End Simulator

M. Meringer, K. Schmidt, T. Trautmann, O. Reitebuch (IPA), D. Huber (DoRIT)

ESA's Atmospheric Dynamics Mission ADM-Aeolus will provide vertical wind profile observations on a global scale to improve the accuracy of numerical weather and climate prediction. The satellite's payload is ALADIN, the Atmospheric Laser Doppler Instrument. It will probe the atmosphere's lowermost 30 km at a wavelength of 355 nm. This Lidar instrument measures Doppler shifts of moving air molecules and macroscopic cloud and aerosol particles. Using a Rayleigh and a Mie spectrometer, line-of-sight wind velocities can be derived. The mission is scheduled for launch in the period from November 2017 to January 2018.

In order to optimize the performance of retrieval algorithms for the mission and to study effects of different instrument settings, an End-to-End Simulator (E2S), originally provided by MDA as *E2S Satellite Simulator*, has been maintained and enhanced for more than a decade. The E2S requires as input various parameters characterizing atmosphere, orbit and payload, and generates downlink data as expected for mission operation. Together with operational data processors this software is used to assess random and systematic error sources and to perform sensitivity studies for the influence of atmospheric and instrumental parameters.

The E2S consists of three main software components: The data preparation component includes the human machine interface that is used to define the input parameters for simulation scenarios. The input parameters are passed as xml files to the data generation component (Fig. 3-12) which actually generates signal, orbit and housekeeping data. Finally the downlink formatter converts the generated data into an Annotated Instrument Source Packet (AISP) product.
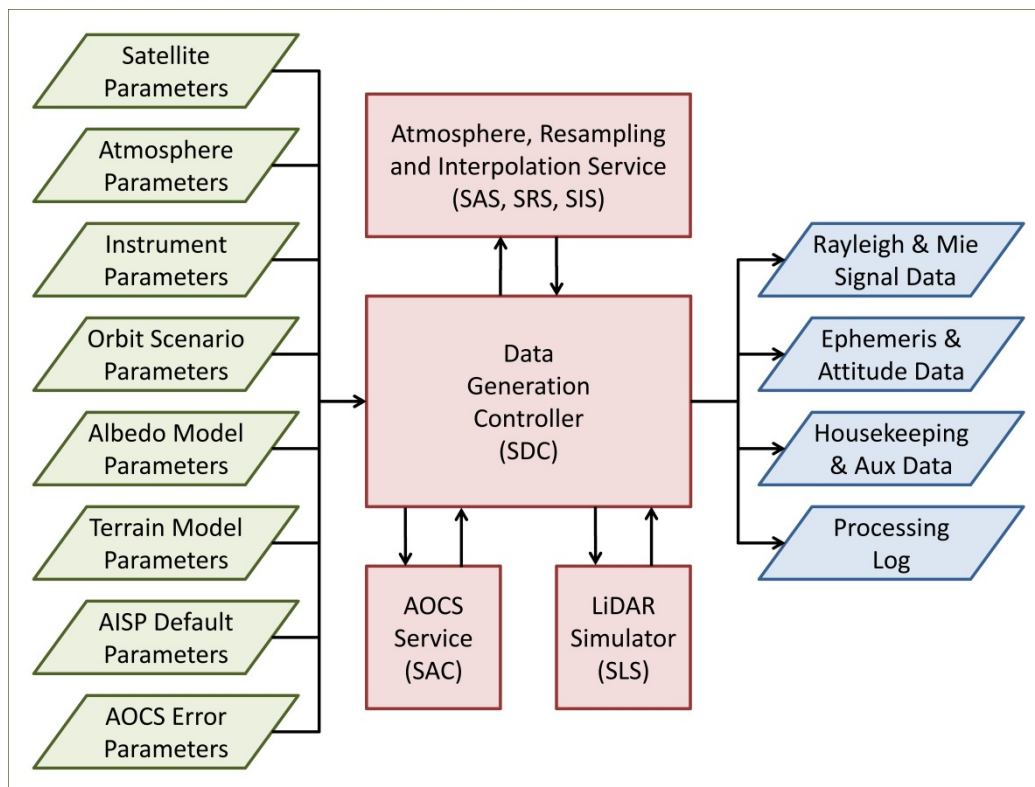
Fig. 3-12: Flowchart of the E2S data generation component.

The data generation component is to a large extent written in MatLab, but also shares some C++ code with the L0, L1a and L1b processors. Sub-components of the data generation component are the data generation controller (SDC) and several so-called services. The SDC coordinates all activities during the data generation process and calls the other services, namely the

- atmosphere service (SAS), which generates atmosphere profiles that correspond to a specific measurement time, using a resampling service (SRS) and an interpolation service (SIS),

- Lidar simulator (SLS), which simulates a set of laser pulses that are transmitted and received by ALADIN through predefined atmospheric layers, and
- Attitude and Orbit Control System (AOCS) service (SAC) that provides orbit- and attitude-related information.

Fig. 3-12 sketches input parameters and output data of the SDC as well as the interaction with the other services. Details are provided in the Detailed Processing Model (*MDA, DLR 2016*), which is continuously updated. Two new revisions of the E2S (3.06 and 3.07) have been delivered to ESA in 2016. Some upgraded and new features of the E2S are listed below:

- Lowering the satellite orbit from 400 km 320 km required adaptions in the AOCS service.
- Including new albedo maps of the ADAM project (*Noveltis 2013*) required code changes in the SDC to automatically switch between nadir and off-nadir maps.
- A random process to simulate non-deterministic rounding during the analog-digital conversion of calculated signals was introduced to the SLS.
- New possibilities have been implemented to compose the reflected transmission function of the Rayleigh spectrometer.

Further deliveries with more advanced features are scheduled for 2017. It is expected that even after launch the E2S will continue to play an important role to better understand details of ALADIN's behavior and to fine-tune retrieval algorithms.

References

MDA, DLR: Aeolus Level 1b Processor and End-to-End Simulator: End-to-End Simulator Detailed Processing Model. ADM-MA-52-1801, 2016.

Noveltis: A Surface Reflectance Database for ESA's Earth Observation Missions (ADAM). NOV-3895-NT-12121, 2013.

3.8   Diagnostics of Tikhonov-type Regularization Schemes for Analyzing MTP Data

J. Xu, J. Zhang (TUM), M. Szajkowski, M. Kenntner (IPA), F. Schreier, A. Doicu, T. Trautmann

The airborne Microwave Temperature Profiler (MTP) was designed to regionally map spatial and temporal aspects of atmospheric temperature around the tropopause region by detecting oxygen emissions between 55 and 60 GHz. Essentially, a measurement cycle comprises 30 brightness temperatures obtained at three frequencies and at ten viewing angles. The retrieval code TIRAMISU (Temperature Inversion Algorithm for Microwave Sounding) built on GARLIC (Generic Atmospheric Radiation Line-by-line Infrared Code) and PILS (Profile Inversion for Limb Sounding) has been developed to estimate vertical temperature profiles from the MTP data. Tikhonov-type regularization schemes are used to stabilize the inversion process in order to obtain a solution with physical meaning. Our study focused on the optimization of regularization configurations in the temperature retrieval by using the synthetic MTP data (*Xu et al. 2016*).

The choice of the regularization parameter is crucial as it balances the residual and the smoothness of the solution. We have assessed the retrieval performance of five well-established parameter selection methods, i.e. the expected error estimation (EEE), the discrepancy principle (DP), the generalized cross-validation (GCV), the maximum likelihood estimation (MLE), and the L-curve (LC). Fig. 3-13 depicts the average absolute differences over 42 Garand atmospheres corresponding to the five parameter selection methods for three noise scenarios. The deviation from the exact profile becomes larger when the noise increases. This tendency is more identifiable in the case of GCV and less identifiable in the case of LC. Both EEE and MLE work reliably and always obtain the two best results.
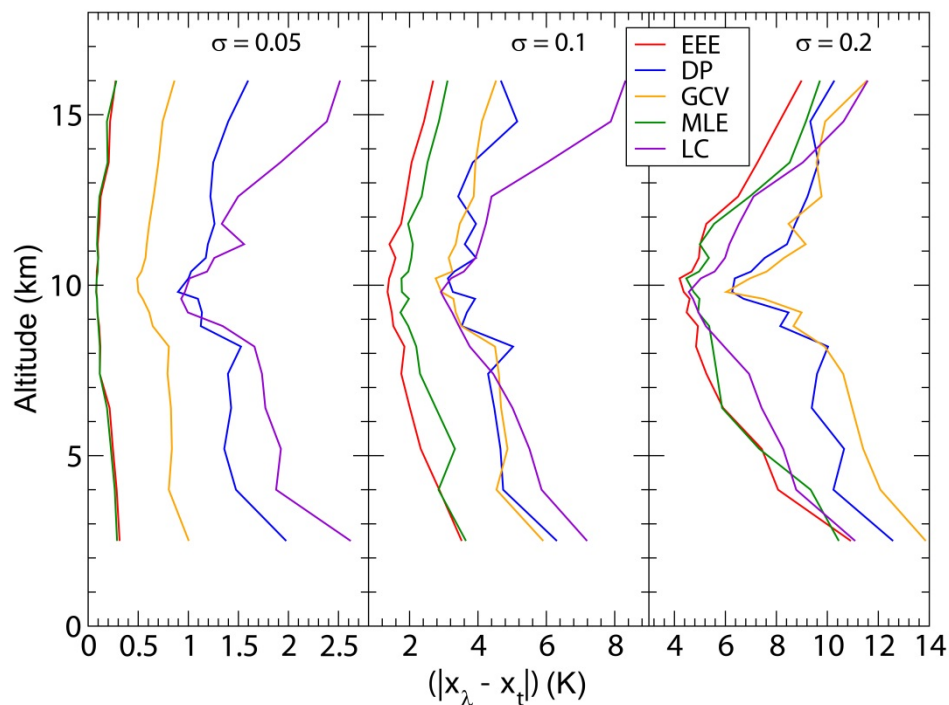
Fig. 3-13: Average absolute temperature difference as a function of altitude over 42 Garand atmospheres for the five regularization parameter selection methods.

Furthermore, the retrieval performance corresponding to different regularization matrices had to be analyzed. A comparison between four matrices, i.e. L0 (identity matrix), L1 (first-order discrete approximation), L2 (second-order discrete approximation), and LC (Cholesky factor of an a priori profile covariance matrix) based on the iteratively regularized Gauss-Newton method has been conducted. In Fig. 3-14, the initial guess is chosen as a height-constant profile (220 K) and the a priori profile is taken as the true profile. LC performs best because the matrix itself is essentially built on the a priori knowledge, whereas the retrieval with L2 seems to be influenced by the measurement noise. Fig. 3-15 presents the retrieval performance of the four regularization matrices under the condition that both the initial guess and the a priori profile are formulated as a scaled version of the true profile. L0 controls the magnitude of the solution and can only retrieve the temperature profile over a narrow range around the

aircraft altitude where the retrieval is more sensitive to the measurement information. Likewise, LC can only derive acceptable results from 8 to 12 km. On the contrary, L1 and L2 can obtain the temperature information over a wider range as both matrices provide the smoothness of the solution. Based on these findings, L1 would be recommended for the real data analysis.

Ongoing efforts to improve the MTP inversion are currently focusing on optimizing the computational efficiency. Furthermore, an extensive intercomparison of the retrieval results from the ML-CIRRUS campaign data between TIRAMISU and the Bayesian statistical method used by JPL is currently carried out. Ground-based observations and in-situ profiles using dropsondes will be used to validate these results.
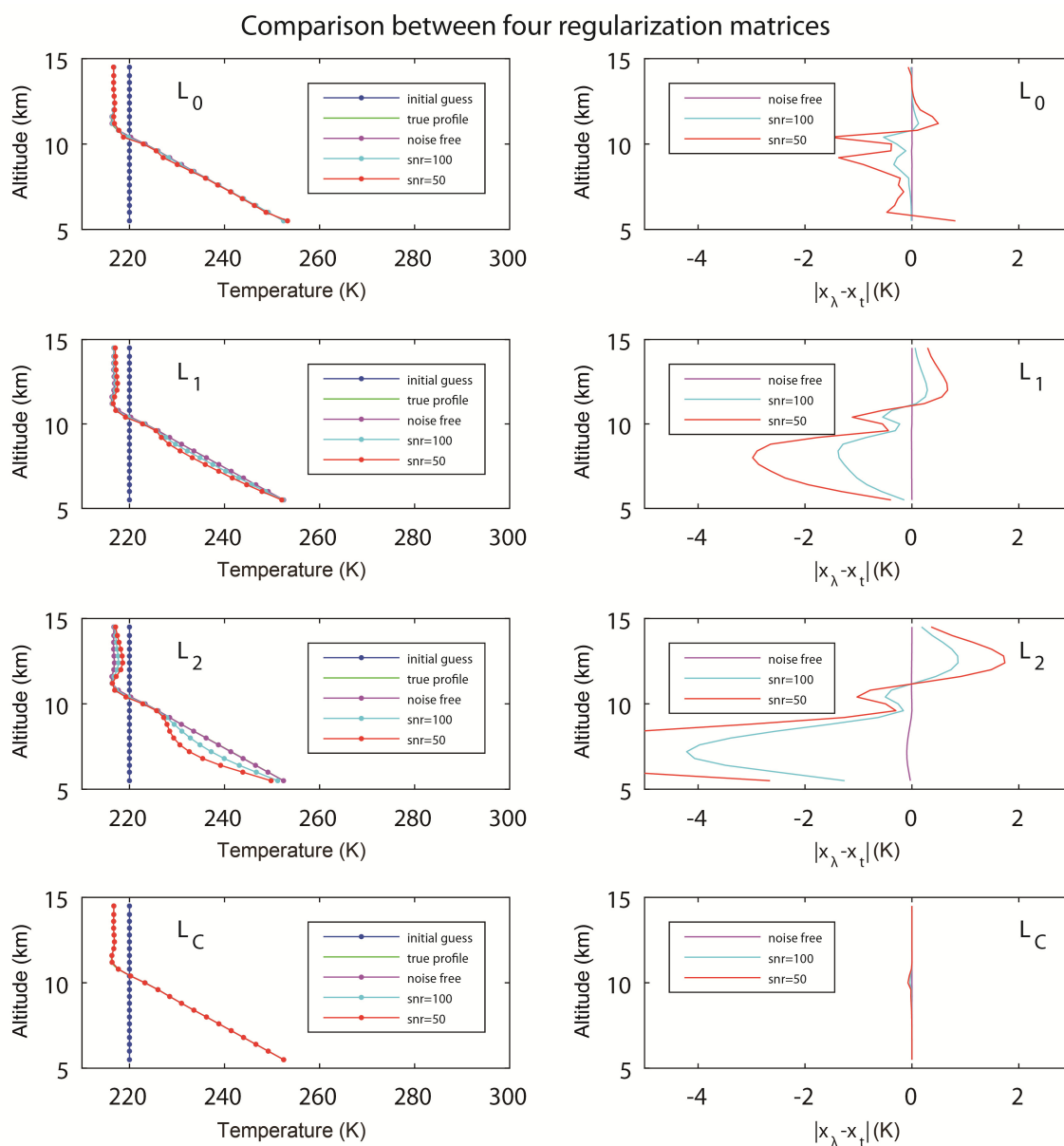
Fig. 3-14: Retrieved temperature profiles and the differences between the retrieved and the true profiles for the four regularization matrices. The results are obtained for the case that the initial guess and the a priori profile are taken as a height-constant profile and the true profile, respectively.
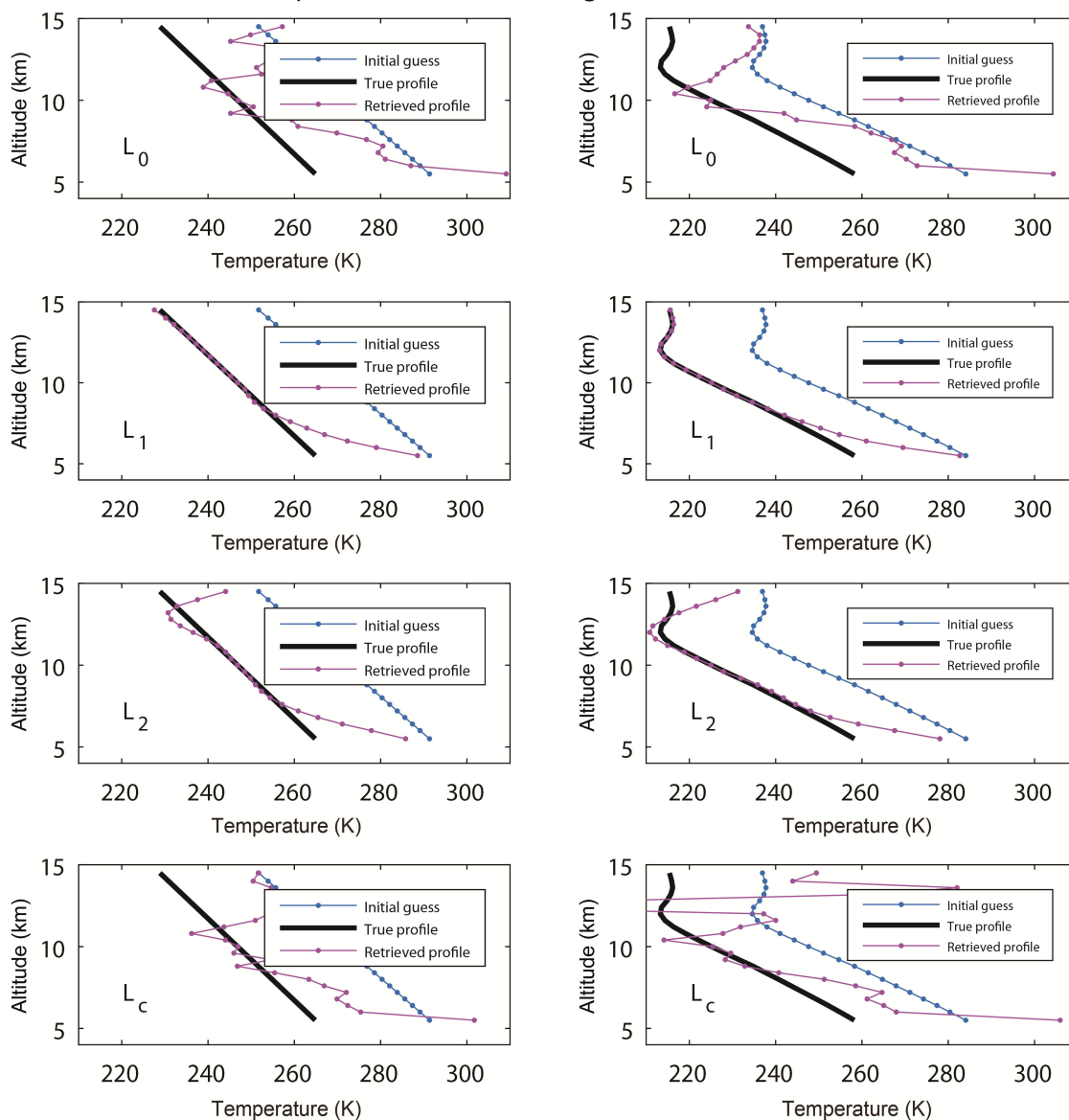
Fig. 3-15: Retrieval results corresponding to the case that the initial guess and the a priori profile are taken as the scaled version of the true profile.

References

Xu, J., Schreier, F., Doicu, A., and Trautmann, T.: Assessment of Tikhonov-type regularization methods for solving atmospheric inverse problems. J. Quant. Spectrosc. & Radiat. Transfer, 184, 274-286, doi:10.1016/j.jqsrt.2016.08.003, 2016.

3.9 Radiative Transfer Model for the Retrieval of Cloud Properties from DSCOVR-EPIC

V. Molina García, S. Sasi, D. Efremenko, A. Doicu and D. Loyola

The launch of the Earth Polychromatic Imaging Camera (EPIC) onboard the Deep Space Climate Observatory (DSCOVR) presents new challenges in the retrieval of atmospheric properties (from aerosols, clouds, etc.) because DSCOVR observes the Earth from the Lagrangian point L1, 1.5 million kilometers far from the Earth within the line Sun-Earth, and the radiances measured by EPIC come from the backscattering region. As a consequence, a standard radiative transfer model based on the discrete ordinate method needs a large number of streams M to describe properly the backward glory region of the phase function.

As EPIC channels contain two pairs of reference and absorption channels in the O_2 A-band and B-band, this sensor is suitable for the retrieval of cloud parameters, e.g. the cloud optical thickness τ_c. We analyzed the requirements for the operational retrieval of cloud parameters from EPIC from a point of view of efficiency and accuracy in three main steps. We investigated how

- the exact Discrete Ordinate method with Matrix Exponential (DOME) and the Matrix Operator method with Matrix Exponential (MOME) behave when delta-M scaling is applied to reduce the number of streams,
- other approximate radiative transfer models behave as compared to the exact models, and
- various acceleration techniques behave to reduce the computation time when convolving the radiances with the instrument response function over the whole bandwidth of every EPIC channel.

Exact radiative transfer models

Reference radiance simulations were performed for channel 9 of EPIC using DOME with line-by-line (LbL) calculation and a number of streams per hemisphere M = 128. Based on this reference, the delta-M scaling technique was applied to the simulations in order to reduce the number of streams to 64, 32, 16 and 8; then, the discrepancies with respect to the reference simulations were computed. The computation times were also tracked.
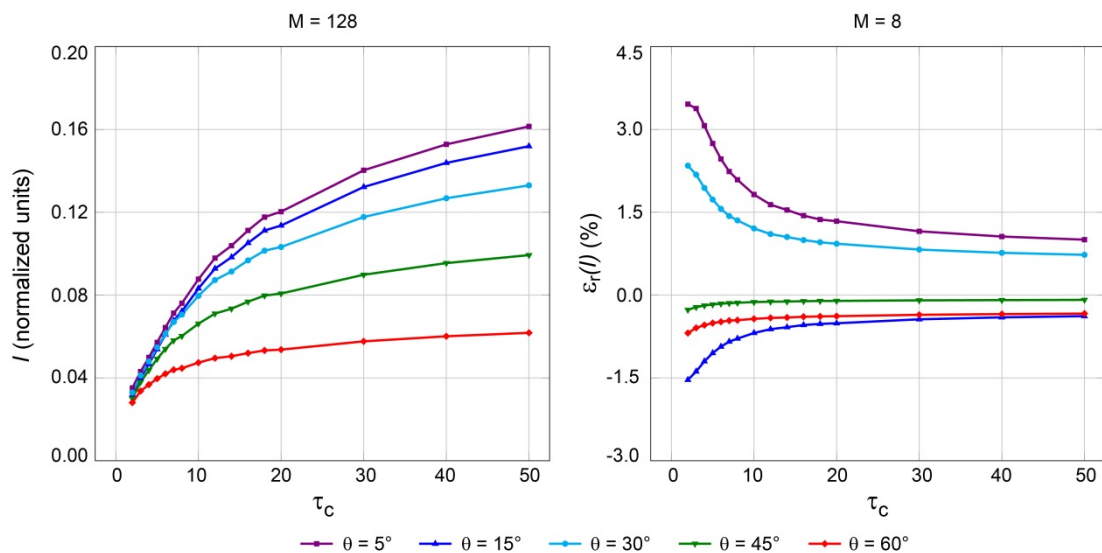
Fig. 3-16: Radiance for the reference simulation M = 128 (left). The right panel shows the relative errors in the simulated radiances when delta-M scaling is applied to reduce the number of streams to M = 8.

In summary, our conclusions can be described as follows (Fig. 3-16 and Table 3-1):

- When the number of streams M increases, the relative errors with respect to the reference decrease, but the computation time increases.
- A number of streams M = 32 is the best compromise between efficiency and accuracy (less than 1.5% of relative error ε_r), but it is still time-consuming (it takes 1.8 hours to compute the

radiances from channel 9 for one value of cloud optical thickness and five viewing angles).
- DOME and MOME perform similarly in terms of efficiency and accuracy, so in the following only DOME is considered.

Streams	8	16	32	64	128
Time	4 min	18 min	1.8 h	15 h	165 h

Table 3-1: Computation times to simulate radiances from channel 9 of EPIC for one value of cloud optical thickness and five viewing angles when the number of streams is reduced using delta-M scaling.

Approximate radiative transfer models

Due to the fact that the exact radiative transfer models DOME and MOME are time-consuming, the accuracy of three approximate models was analyzed for simulations with M = 32 and using LbL calculation: the 4-order asymptotic model, the 0-order (or classical) asymptotic model and the Equivalent Lambertian Cloud (ELC) model. From the point of view of accuracy (Fig. 3-17):

- all the approximate models gave inaccurate results for $\tau_c < 10$,
- the 0-order asymptotic model showed a similar behaviour to the 4-order asymptotic model for $\tau_c > 10$, but a worse one for $\tau_c < 10$ (with relative errors up to 25%), and
- the ELC model was inaccurate for the whole range of τ_c that was analyzed, with relative errors up to 40% for small values of the cloud optical thickness.
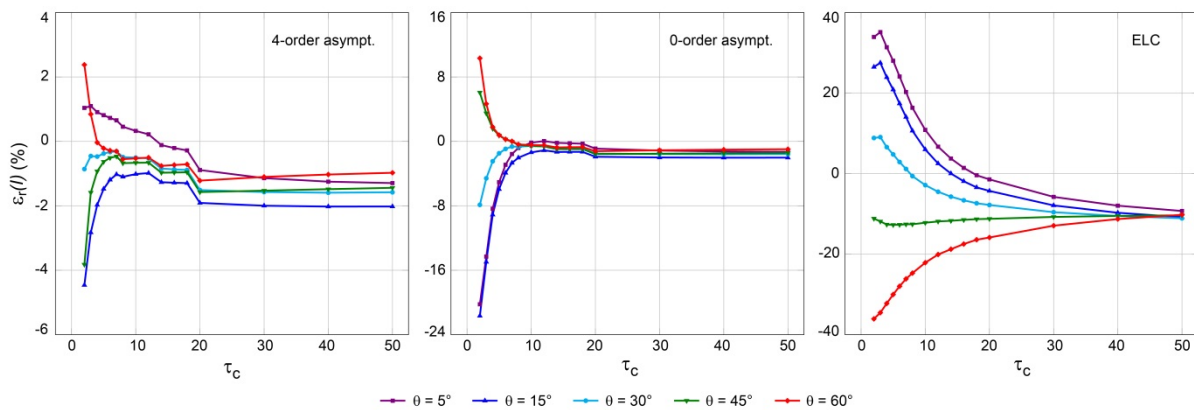
Fig. 3-17: Relative errors in the simulated radiances when different approximated radiative transfer models are applied for M = 32.

Acceleration techniques

In addition to the Padé approximation, the telescoping technique and the truncated-plus-single-scattering (TMS) method, the following acceleration techniques were compared to the LbL calculations for a number of streams per hemisphere M = 32 (Fig. 3-18):

- the correlated k-distribution method,
- the Principal Component Analysis method (PCA), and
- a novel combination of the k-distribution method plus the PCA method.

Quasi-identical relative errors are obtained for every acceleration technique (less than 1.5%). The computation time of the combined k-distribution plus PCA is the most efficient: 18 seconds to compute the radiances from channel 9 for one value of cloud optical thickness and five viewing angles. This result is 5 times faster than the PCA method, 35 times faster than the correlated k-distribution method and 360 times faster than the LbL calculation.
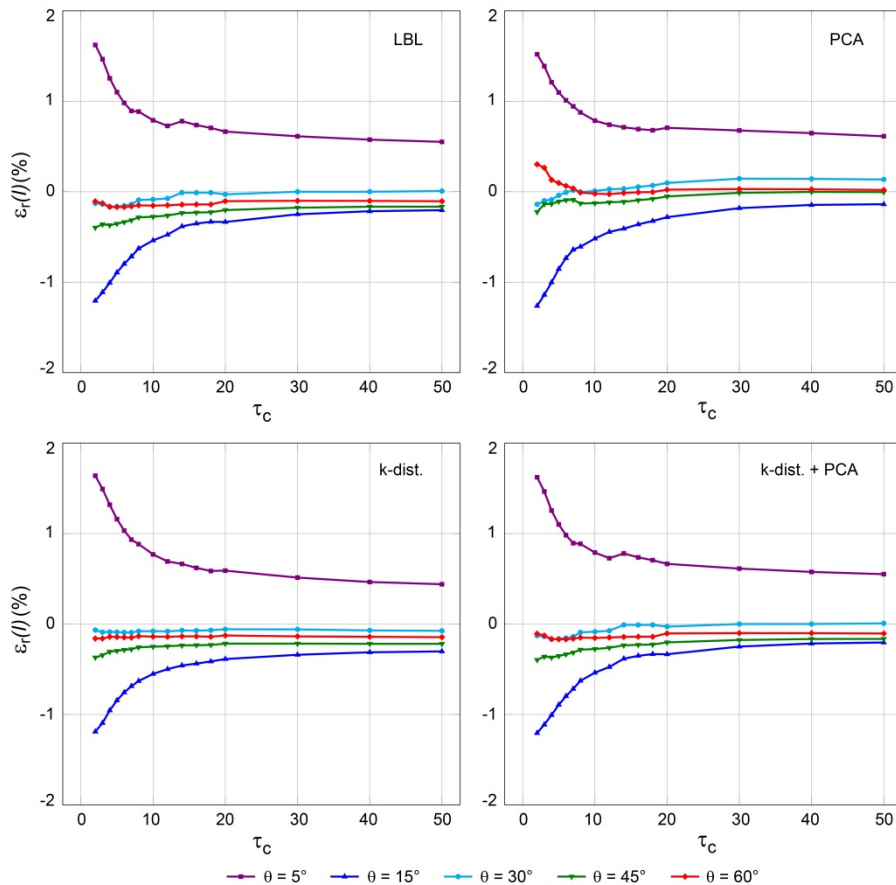
Fig. 3-18: Relative errors in the simulated radiances for M = 32 when LbL calculation is used and when different acceleration techniques are introduced.

As a final summary, the retrieval of cloud parameters from EPIC measurements has to take into account the fact that EPIC measures in the backscattering region, and three main requirements should be considered when developing its operational retrieval processor for cloud parameters: First, the exact models DOME/MOME need at least 32 streams per hemisphere to give accurate results over the whole range of τ_c. Second, the approximate models such as the 4-order and 0-order asymptotic models or the ELC model are not appropriate, as their accuracy is insufficient. Finally, DOME/MOME together with the combined k-distribution plus PCA method fulfills the requirements of accuracy and efficiency.

References

Doicu, A., Trautmann, T.: Discrete-ordinate method with matrix exponential for a pseudo-spherical atmosphere: Scalar case. J. Quant. Spectrosc. & Radiat. Transfer, 110, 146-158. doi:10.1016/j.jqsrt.2008.09.014, 2009.

Efremenko, D., Doicu, A., Loyola, D., Trautmann, T.: Optical property dimensionality reduction techniques for accelerated radiative transfer performance: Application to remote sensing total ozone retrievals. J. Quant. Spectrosc. & Radiat. Transfer, 133, 128-135, doi:10.1016/j.jqsrt.2013.07.023, 2014.

Efremenko, D., Doicu, A., Loyola, D., Trautmann, T.: Acceleration techniques for the discrete ordinate method. J. Quant. Spectrosc. & Radiat. Transfer, 114, 73-81, doi:10.1016/j.jqsrt.2012.08.014, 2013.

Goody, R., West, R., Chen, L., Crisp, D.: The correlated k-method for radiation calculations in nonhomogeneous atmosphere. J. Quant. Spectrosc. & Radiat. Transfer, 42, 539-550, doi:10.1016/0022-4073(89)90044-7, 1989.

Natraj, V., Shia, R., Yung, Y.: On the use of principal component analysis to speed up radiative transfer calculations. J. Quant. Spectrosc. & Radiat. Transfer, 111, 810-816, doi:10.1016/j.jqsrt.2009.11.004, 2010.

3.10 Deriving Ozone Profile Shape from Satellite UV Measurements

J. Xu, D. Loyola, F. Romann, A. Doicu

Reliable ozone profiles are critical to the retrieval of total and tropospheric column products of ozone. Inspired by the success of machine learning techniques, we propose a new algorithm called OPS-FPML (Ozone Profile Shapes retrieval using Full Physics Machine Learning) for deriving ozone profile shapes from ultraviolet (UV) absorption spectra that are measured by space-borne instruments. Our objective is to establish a mapping between the ozone profile shape and the observed UV nadir-viewing spectra using machine learning tools. The main novelty of our study is that we formulate the retrieval problem in a classification framework instead of a conventional inversion one.

The OPS-FPML algorithm consists of the following features:

- We combine two ozone climatologies providing abundant information on ozone profile shapes.
- A semi-supervised k-means clustering algorithm is capable of capturing ozone variability.
- A full physics method based on radiative transfer calculations which is conducted only once and off-line due to the "smart sampling" technique (*Loyola et al. 2016*).
- Principal Component Analysis (PCA) largely reduces the dimensionality of the original input data without significant loss of information.
- A Multi-Layer Perceptron (MLP) with proper configurations largely boosts the classification performance.
- MLP is used to derive the final profile shape scaling to a given total ozone column.
- The application to real data turns out to be very fast with producing promising results.

We have applied the OPS-FPML algorithm to the real GOME-2 measurements and compared the predicted ozone profiles with the ones produced by the RAL retrieval algorithm (RAL-OEM) which is based on the optimal estimation method. In 2008, a thinning in the ozone layer over Antarctica was larger both in size and duration. As for this particular comparison, we selected cases where the total column was measured to be less than 200 DU.

Time (UTC)	Latitude (°N)	Longitude (°E)	OPS Index
03:46	-70.3	58.3	6
03:48	-78.4	83.3	6
13:52	-63.3	-81.3	6
13:56	-78.4	-76.0	6
00:03 (+1)	-74.6	140.6	6
00:05 (+1)	-78.5	131.8	6

Table 3-2: Geolocation of retrieved ozone profiles from MetOp-A/GOME-2 data on October 4, 2008 and the corresponding predicted class index with respect to the OPS-FPML profile.

Table 3-2 summarizes the relevant information and the predicted class index with respect to the OPS-FPML algorithm for the chosen six cases on October 4, 2008. Fig. 3-19 depicts a comparison for the ozone hole in the Antarctic polar region on this particular day. The ozone partial columns derived by both algorithms agree very well in the stratosphere, while some discrepancies are found in the troposphere where the RAL-OEM profiles possess a larger error budget. It is planned to perform further comparison studies incorporating an error characterization (of all possible uncertainties) into the OPS-FPML algorithm.

This new algorithm uses advanced machine learning tools to characterize ozone profile shapes in an efficient manner, naturally paving the way for a new class of algorithm ideally suited to fully exploit the next generation of atmospheric composition sensors starting with TROPOMI/S5P to be launched in summer 2017. The future work will focus on the error characterization and the comparisons with ground-based ozone measurements.
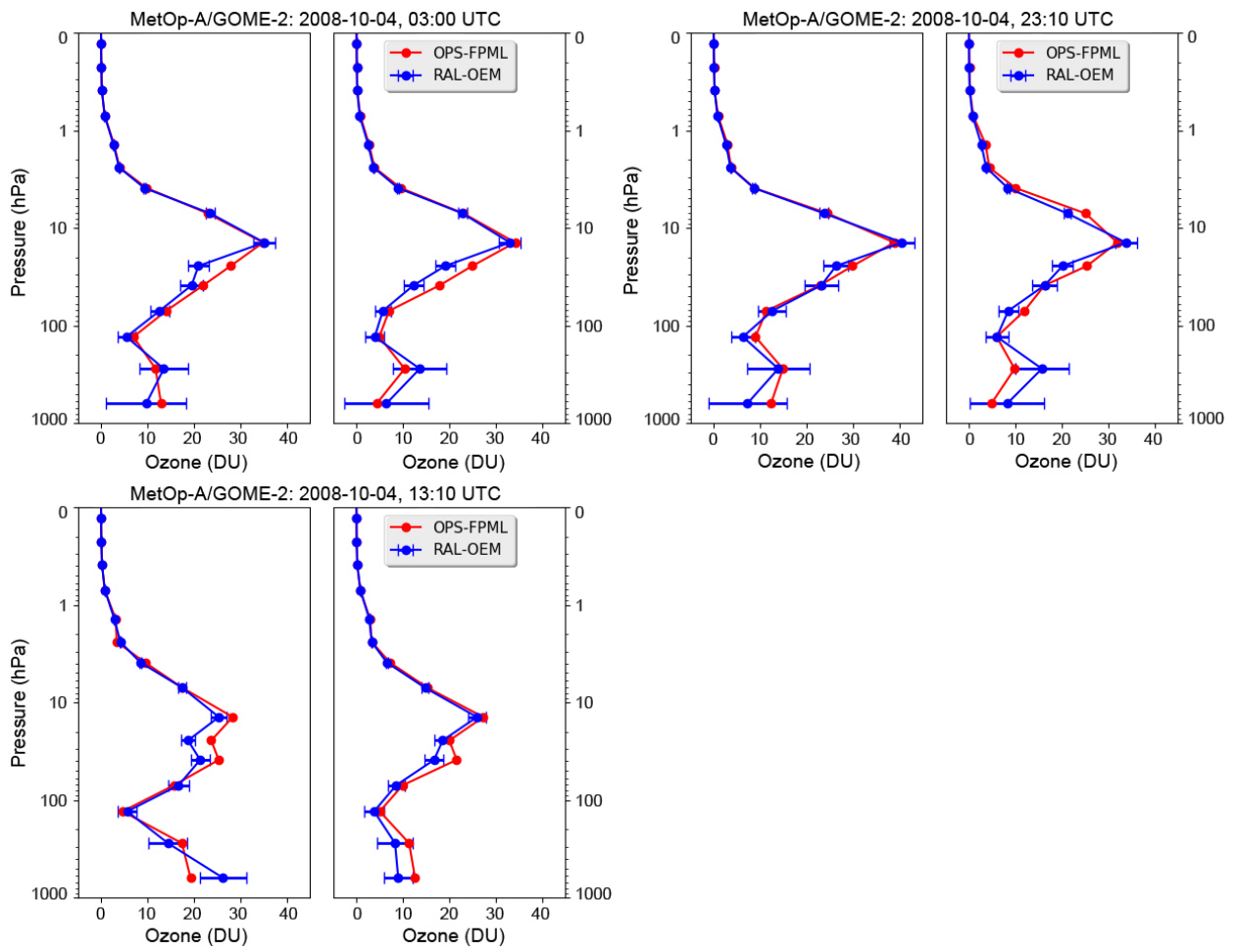
Fig. 3-19: Comparisons of estimated ozone profiles for six random cases from GOME-2 data measured on the early morning, the noon, and the night of October 4, 2008, respectively.

References

Loyola, D., Pedergnana, M., Gimeno García, S.: Smart sampling and incremental function learning for very large high dimensional data. Neural Networks, 78, 75-87, doi:10.1016/j.neunet.2015.09.001, 2016.

3.11 Assessment of some Closed-form Expressions for the Voigt Function

F. Schreier

The Voigt function, defined as convolution of a Lorentzian and a Gaussian function,

$$K(x,y) \;=\; \frac{y}{\pi} \int_{-\infty}^{\infty} \frac{e^{-t^2}}{(x-t)^2 + y^2} \, dt \tag{1}$$

is important in many branches of physics, e.g., atomic and molecular spectroscopy, atmospheric radiative transfer, plasma physics, astrophysics etc. Here x is a measure of the distance to the center peak, and y is essentially the ratio of the Lorentzian and Gaussian width. Unfortunately, the convolution integral cannot be evaluated in closed analytical form and has to be computed numerically, e.g., using series or asymptotic expansions, rational approximations, Gauss-Hermite quadrature, etc. (see e.g. our annual report 2010).

A closed-form solution of the integral can be readily obtained using a simple approximation for the Gauss function. The *Atlas of Functions* (*Oldham et al. 2009*) noted that a triangular defined by

$$g_{\mathrm{af}}(x) \;=\; \begin{cases} 1 - |x|/\sqrt{\pi} & |x| \leq \sqrt{\pi} \\ 0 & \text{else} \end{cases} \tag{2}$$

gives a good approximation with the correct integral value and peak value. Jiménez-Mier suggested "a triangular function of the same width and area" (*Jiménez-Mier 2001*), and two further triangulars can be constructed with the condition of correct integral value and correct half width. A comparison of these approximations with the Gaussian is shown in Fig. 3-20.

The integral of the product of the triangular function and the Lorentzian can be evaluated analytically, leading to a combination of logarithms and inverse trigonometric (arctan) functions. However, despite the closed-form representation of $K(x,y)$ these approximations appear to have little value. For large $y > 10$ the approximation based on the *Atlas of Functions* triangular has a relative accuracy of

Fig. 3-20: Comparison of triangular functions used to approximate the Gaussian.

$$\left| \delta K(x,y) \right| / K_{ref}(x,y) \leq 10^{-3} \tag{3}$$

when compared to a highly accurate reference code. However, for large y the Voigt function is easy to calculate because it is essentially equivalent to the Lorentzian. For smaller y significant errors of these approximations show up for intermediate values of x. Furthermore, except for the approximation based on the *Atlas of Functions triangular* the approximations also fail in the line center. In view of the six function calls required for each x,y (four calls if the logarithms are combined), these approximations are also likely to be less efficient. In fact, evaluation of molecular absorption cross sections for some dozen atmospheric levels were about a factor 4-5 slower with the "triangular Voigt approximation" compared to the Humliček-Weideman combination of rational approximations suggested some years ago (*Schreier 2011*).

In conclusion, this kind of approximation fails to give a useful approach to evaluate the Voigt function accurately except for very large values of the Lorentz to Gauss width ratio y, see *Schreier (2016)* for details. Our timing benchmarks also indicate that these approximations are not competitive from a computational efficiency point of view. The approximations might be useful in certain applications.

Nevertheless, there are numerous more accurate and efficient approximations suitable for a wide range of applications. In particular, rational approximations are easy to implement and can be very efficient.
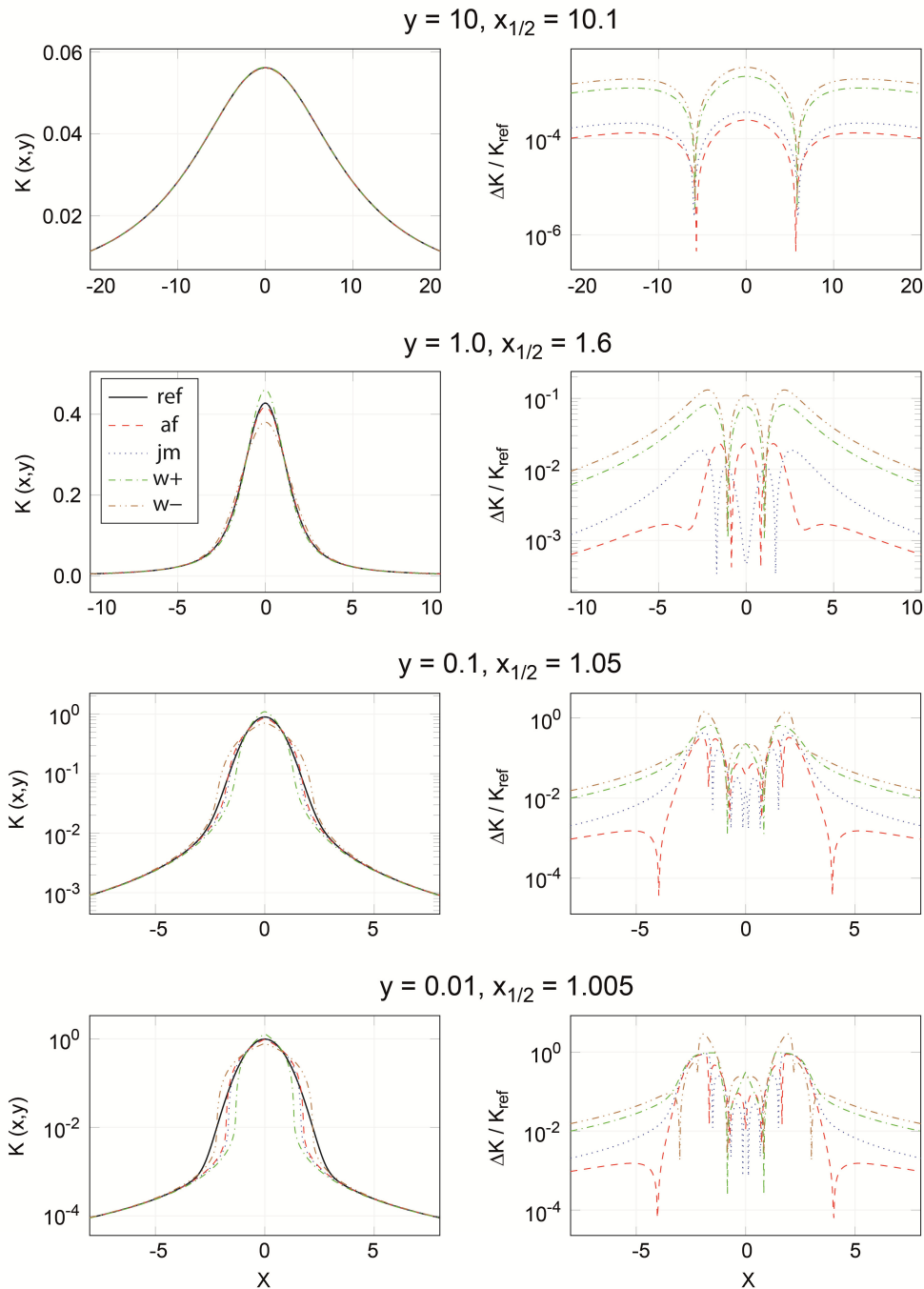
Fig. 3-21: Comparison for y = 10 (top), y = 1, y = 0.1, and y = 0.01 (bottom). Note the different ranges of the x axis. Furthermore a linear K axis is used for the large y cases, whereas a logarithmic axis is used for small y.

References

Oldham K.B., Myland J., Spanier J.: An Atlas of Functions. New York, NY: Springer, 2009.

Jiménez-Mier J.: An approximation to the plasma dispersion function. J. Quant. Spectrosc. & Radiat. Transfer, 70(3), 273-284, 2001.

Schreier F.: Optimized implementations of rational approximations for the Voigt and complex error function. J. Quant. Spectrosc. & Radiat. Transfer, 112, 1010-1025, 2011.

Schreier, F.: An assessment of some closed-form expressions for the Voigt function. J. Quant. Spectrosc. & Radiat. Transfer, 176, 1-5, 2016.

3.12 Computational Aspects of Speed-dependent Voigt Profiles

F. Schreier

Collisional (pressure) and Doppler broadening of molecular absorption lines is conveniently modeled by the convolution of a Lorentz and a Gauss function, i.e. the Voigt function (see chapter 3.11). Inadequacies of this profile have been observed since decades in molecular laboratory spectroscopy. Changes of molecular velocity due to collisions reduce the Doppler broadening (termed *collisional* or *Dicke narrowing*) and the speed-dependence of the relaxation rates alters the Lorentz line shape. In recent years, the increasing quality of atmospheric spectroscopy observations has also indicated the limitations of the Voigt profile. The partially Correlated quadratic Speed-Dependent Hard-Collision profile (pCqSDHCP), or Hartmann–Tran (HT) profile for short, recommended as the appropriate model for high resolution spectroscopy, accounts for both collisional narrowing and speed-dependence (*Tennyson et al. 2014*).

From a computational point, both the Speed-dependent Voigt (SDV) profile and the HT profile can be calculated readily from the complex error function. The SDV profile is essentially given by the difference of two Voigt profiles

$$g_{\text{sdv}}(\nu; \hat{\nu}, \gamma_{\text{L}}, \gamma_2, \gamma_{\text{D}}) \;=\; \frac{\sqrt{\ln 2/\pi}}{\gamma_{\text{D}}} \text{Re}\Big(w(z_1) - w(z_2)\Big) \tag{1}$$

where $w(x+iy)$ is the complex error function whose real part is the Voigt function $K(x,y)$. Here ν is the wavenumber (frequency), $\hat{\nu}$ is the line position, γ_L and γ_D denote the Lorentzian and Doppler width, γ_2 characterizes the speed dependence of the pressure broadening, and z_1 and z_2 depend on these variables. The HT profile also involves the difference of two complex error functions scaled with the square of their arguments. In view of these differences, highly accurate numerical algorithms are required for the computation of the complex error function.

For the SDV profile it has been suggested to use the Humlíček algorithm (*Humlíček 1982*) that, like most other codes, employs four different rational approximations in different regions of the complex z plane. However, a moderately accurate approximation such as Humlíček's with a claimed accuracy of 10^{-4} can be insufficient for a reliable difference computation (Fig. 3-22).
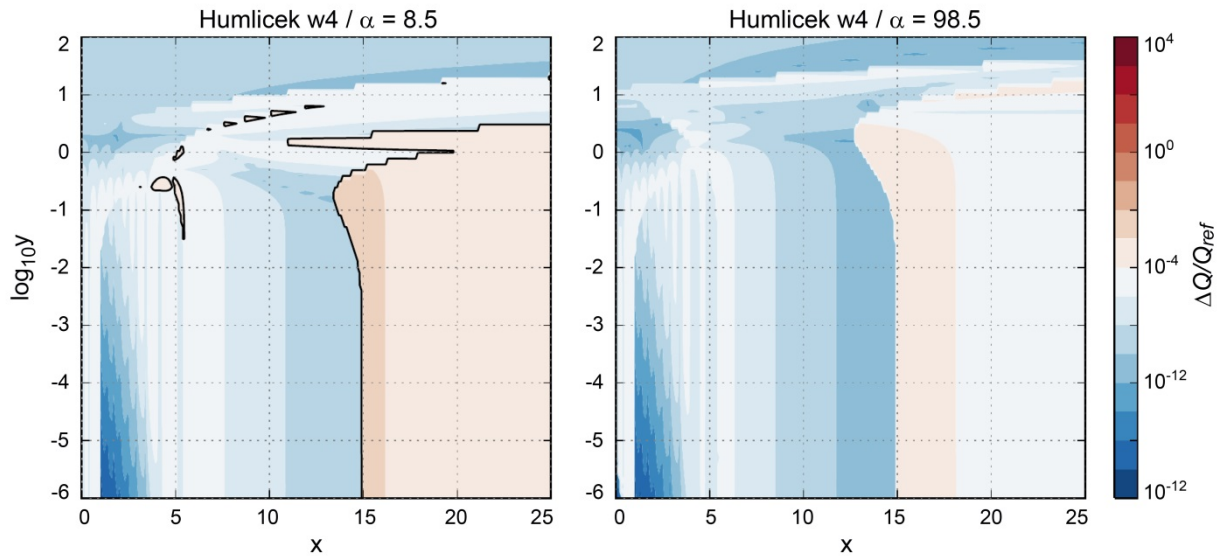
Fig. 3-22: Relative accuracy of the *Humlíček* SDV implementation ($Q = \text{Re}(w(z_1) - w(z_2))$) and $\alpha = \gamma_2/\gamma_L$).

Furthermore, it has been stated that both terms of the difference in equ. (1) have to be computed with the same approximation. However, for a given wavenumber ν and set of line parameters the two arguments z_1 and z_2 can be vastly different, and a rational approximation suitable for a certain z is not necessarily applicable outside its original region. Accordingly, the recommendation to use the same

rational function for both arguments irrespective of their location in the complex plane can lead to substantial errors for one of the two terms in equ. (1).

A slight modification of the Humlíček-Weideman combination suggested some years ago (*Schreier 2011*, see also annual report 2010) enables a highly efficient and accurate algorithm for the complex error function that can be used reliably for the SDV evaluation.

$$
w(z) \;=\; \begin{cases} \dfrac{iz(z^2/\sqrt{\pi}-1.410474)}{(z^2-3)z^2+3/4} & \text{for } |x|+y \geq 5.5 \\[2ex] \dfrac{\pi^{-1/2}}{L-iz} \;+\; \dfrac{2}{(L-iz)^2}\displaystyle\sum_{n=1}^{32} a_n\left(\dfrac{L+iz}{L-iz}\right)^{n-1} & \text{else (with } L = \sqrt{32/\sqrt{2}}) \end{cases} \tag{2}
$$

In contrast to the 2011 implementation, polynomials of higher degree are used here that do not have significant impact on the computational speed. Fig. 3-23 demonstrates that this algorithm provides SDV values with a relative accuracy of six digits or better.
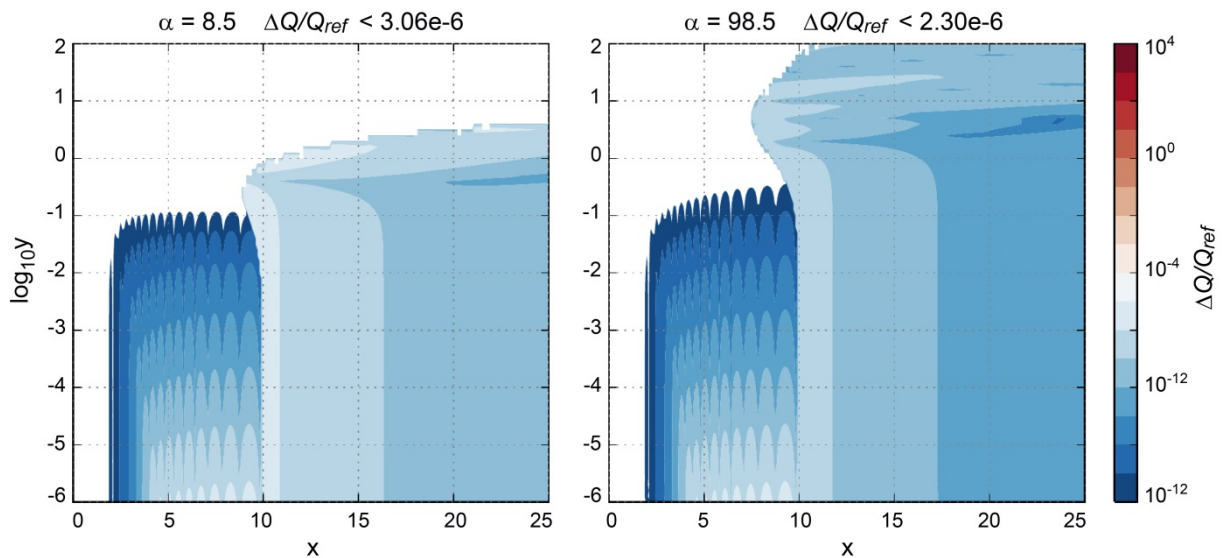
Fig. 3-23: Relative accuracy of the SVD implementation using the Humlíček-Weideman combination.

References

Humlíček, J.: Optimized computation of the Voigt and complex probability function. J. Quant. Spectrosc. & Radiat. Transfer, 27, 437-444, 1982.

Schreier F.: Optimized implementations of rational approximations for the Voigt and complex error function. J. Quant. Spectrosc. & Radiat. Transfer, 112, 1010-1025, 2011.

Schreier, F.: Computational aspects of speed-dependent Voigt profiles. J. Quant. Spectrosc. & Radiat. Transfer, 187, 44-53, 2017.

Tennyson, J., Bernath, P.F., Campargue, A., et al.: Recommended isolated-line profile for representing high-resolution spectroscopic transitions (IUPAC technical report). Pure Appl. Chem., 86(12), 1931-1943, 2014.

3.13 Matrix-exponential Formalism for Deriving Fast Approximate Models

D.S. Efremenko, A. Doicu, V. Molina García, T. Trautmann

The radiative transfer is an important issue for astrophysics, atmospheric physics, meteorology and engineering sciences. Several radiative transfer codes used in the remote sensing community (such as DISORT (*Stamnes 1986*)) are based on the discrete ordinate method (DOM). The latter involves replacing the continuous dependence of the radiance on direction by a dependence on a discrete set of directions. In the classical implementation of DOM of Chandrasekhar, the solution of the system of equations is expressed as a linear combination of characteristic solutions of the discretized problem. Another group of methods is based on the concept of invariant imbedding, which is due to Ambartsumian. He derived an equation for the reflection function of a semi-infinite atmosphere by noting that the reflection function remains unchanged upon addition of a new layer. This technique was further generalized by Chandrasekhar to a finite layer, while *Bellman et al. (1960)* showed that the reflection function derived by using the invariant imbedding satisfies the Riccati equation.

We have proven the mathematical equivalence of the discrete ordinate method, the matrix operator method, and the matrix Riccati equations method by means of an eigenvector representation of the matrix exponential. That means, the matrix exponential formalism gives the framework for the unification of the discrete ordinate method, the matrix operator method, and the matrix Riccati equations method.

Of special interest are analytical models since they are much faster and more convenient for theoretical considerations than numerical models based on discrete ordinate schemes. For optically thin layers, the matrix exponential can be efficiently evaluated by using the Padé approximation or its Taylor series expansion. These techniques were described by *Waterman (1981)*. Another set of models was derived for optically thick layers. They are often referred to as asymptotic models and enable the representation of the radiance field through simple analytical formulas. *Nakajima and King (1992)* derived the expressions of the functions and constants that occur in the asymptotic theory by using the *eigendecomposition* method, and proposed to use the asymptotic formulas in the framework of the discrete ordinate method when the layer optical thickness exceeds a certain value.

Despite the variety of computational techniques, they all can be derived on the base of the matrix exponential formalism. In particular, the discrete ordinate approach of Nakajima and King was adapted to our framework, and was applied to derive the asymptotic expressions of the reflection and transmission matrices for large values of the optical thickness. Besides, we obtained higher-order corrections of the reflection and transmission matrices for moderate values of the optical thickness, reconsidered Waterman's approximation by including an additional term in the expression of the reflection matrix, and derived a parametrization of the asymptotic functions and constants for a water-cloud model with a Gamma size distribution. The practical conclusion is that the approximate models can speed up the computational process. An efficient radiative transfer code should incorporate built-in routines that automatically work when the optical thickness of a homogeneous (sub-)layer becomes too small or too large. On the other hand, the nth-order Padé and Taylor series approximations and the nth-order iterative approximation can be used for the initialization of the doubling method in radiative transfer, while the asymptotic form of the reflection function can be used in a cloud parameter retrieval algorithm. In the latter case, the computational process is organized as follows:

(I)   replace the atmosphere below the cloud bottom by an equivalent Lambertian surface of albedo A,
(II) compute the reflection function of a layer with an underlying Lambertian surface albedo by means of the asymptotic theory, and
(III) use the cloud reflection function as a bidirectional reflection function in a discrete ordinate model to compute the radiance field of the atmosphere above the cloud top.

References

Bellman, R., Kalaba, R., Wing, G.: Invariant imbedding and mathematical physics - I: Particle processes. J. Math. Phys., 1, 280-308, 1960.

Nakajima, T., King, M.D.: Asymptotic theory for optically thick layers: application to the discrete ordinates method. Appl. Opt, 31(36), 7669-7683, 1992.

Stamnes, K.: The theory of multiple scattering of radiation in plane parallel atmospheres. Rev. Geophys., 24(2), 299-310, 1986.

Waterman, P.C.: Matrix-exponential description of radiative transfer. J. Opt. Soc. Amer. 71(4), 410-422, 1981.

3.14 Python Tool for Radiative Transfer Calculations

D.S. Efremenko, V. Molina García, T. Trautmann

Radiative transfer (RT) model simulations are an important component of atmospheric correction and trace gas retrieval algorithms. Radiative transfer as an educational discipline is included in master programs of several education institutions. A well-known RT code DISORT supplied with the textbook of *Thomas and Stamnes (2002)* provides a foundation in both the theoretical and practical aspects of radiative transfer. To run simulations for realistic atmospheric scenarios, the atmospheric state (e.g. trace gas profiles, temperature profiles, aerosol profiles) needs to be converted into optical properties (arrays of optical thicknesses, single scattering albedos and phase functions), which are used as input to a RT code (see Fig. 3-24).
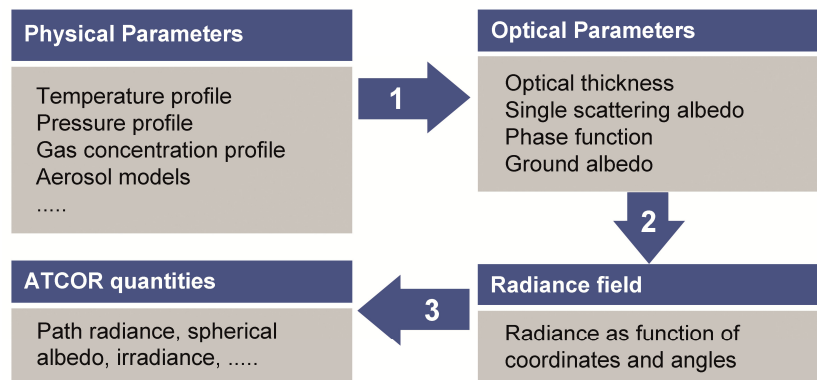
Fig. 3-24: The computational chain required for atmospheric correction.

We have developed a tool for RTM simulations within a flexible and easy-customizable environment. It incorporates:

- a radiative transfer solver,
- a set of routines for accessing spectroscopic and aerosol databases,
- a collection of climatological gas profiles,
- and some auxiliary routines.
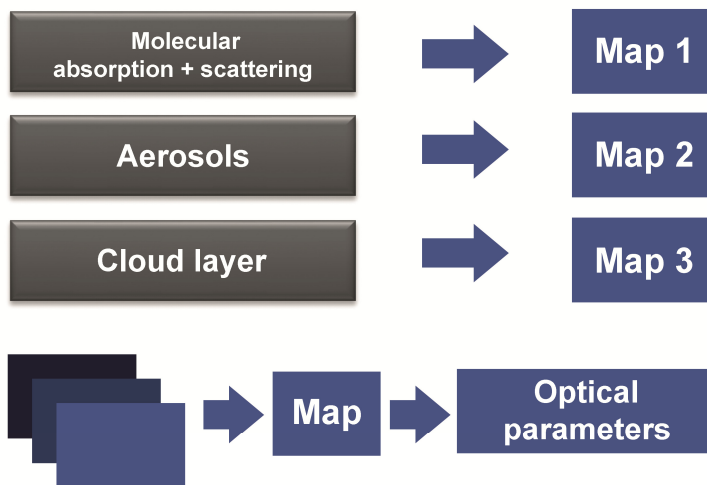
Fig. 3-25: The concept of maps derived from atmospheric constituents.

The RT solver is based on the discrete ordinate with matrix exponential (*Doicu and Trautmann 2009*) and is extended to the coupled atmosphere-ocean scenes. In addition, it can also treat a specular reflection from the surface (a "mirror" case) and the rough interface between atmosphere and ocean according to the Cox-Munk model. The RT solver is implemented in Python which provides code readability and allows us to manage both low level details and the high-level Python API. Our solver is based on the NumPy routines and most of the for-loops are avoided by using vectorization and matrix calculus. The performance of the Python code is approximately only 20% lower than that of C++ implementation.

The solver is equipped with tools for modeling the atmospheric state. The interfaces to the OPAC database (*Hess et al. 1998*) of aerosol models and the molecular spectroscopic database HITRAN are provided. The computations of optical properties of the atmosphere are based on the concept of "maps". Class Map contains a table of scattering, extinction and absorption coefficients together with expansion coefficients of phase functions for each atmospheric level. Molecular scattering, molecular absorption, aerosol and cloud models provide maps, which are then mixed into a new map corresponding to all atmospheric constituents. The optical parameters are derived from the resulting map (see Fig. 3-25).

The current version covers the UV-VIS-NIR spectral ranges. The atmospheric state can be constructed in an interactive mode by assembling available components by means of corresponding Python routines. We plan to develop interfaces for accessing the MIESCHKA code (*Rother et al. 1999*) for computing scattering properties for spherical and non-spherical particles.

References

Doicu, A., Trautmann, T.: Discrete ordinate method with matrix exponential for a pseudo-spherical atmosphere: Scalar case. J. Quant. Spectrosc. & Radiat. Transfer, 110, 146-158, 2009.

Hess, M., Koepke, P., Schult, I.: Optical Properties of Aerosols and Clouds: The Software Package OPAC. Bull. Amer. Meteor. Soc., 76 (5), 831, 1998.

Rother, T., Havemann, S., Schmidt, K.: Scattering of plane waves on finite cylinders with noncircular cross sections. Progress in Electromagnetic Research, 23, 79-105, 1999.

Thomas, G., Stamnes, K.: Radiative Transfer in the Atmosphere and Ocean, Cambridge University Press, 2002.

4.   Atmospheric Remote Sensing – Applications

4.1   Extended ESA-CCI GOME-type Total Ozone Essential Climate Variable: Climate Applications

M. Coldewey-Egbers, D. Loyola

In the past year we continued our work related to the GOME-type *Total Ozone Essential Climate Variable (GTO-ECV)* data record which has been created within the framework of the European Space Agency's Climate Change Initiative (ESA-CCI). Within phase 2 of the Ozone_cci project the existing GTO-ECV data record (*Coldewey-Egbers et al. 2015*) has been extended in time and a new sensor has been added.

Total ozone column observations from GOME (Global Ozone Monitoring Experiment), SCIAMACHY (Scanning Imaging Absorption Spectrometer for Atmospheric Chartography), GOME-2A, and OMI (Ozone Monitoring Instrument) have been combined into one homogeneous time series, thereby taking advantage of the high inter-sensor consistency having been achieved through the application of a common retrieval algorithm. Remaining small biases among individual instruments have been removed by using an inter-sensor calibration approach in which OMI is used as the reference standard. The extended data record spans the 20-year period from July 1995 to June 2015.

Compared to the ground-based measurement standard (Brewer, Dobson as well as other UV-VIS instruments) the gridded global monthly mean total ozone columns showed an excellent agreement and long-term stability for almost all latitudes. A small number of outliers were found which is mostly related to spatial and temporal sampling issues. In conclusion, the GTO-ECV CCI level 3 validation exercise demonstrated that the GTO-ECV product easily meets the ESA-CCI user requirement levels based on GCOS, the Global Climate Observing System. Therefore it is suitable for a variety of applications; two of these are illustrated below.

Monitoring the long-term evolution of total ozone

In Fig. 4-1 (adapted from *Weber et al. 2016*) the total ozone annual means from different data sources incl. ESA-CCI GTO-ECV are shown for 1970-2015 in various zonal bands: near global (60°S-60°N), mid-latitudes in both hemispheres (35°-60°), and the inner tropics (20°S-20°N). Also shown are the polar time series in March (Northern Hemisphere, 60°N-90°N) and October (Southern Hemisphere, 60°S-90°S), the months when polar losses are largest in each hemisphere. Poleward of 60°S, a record low October mean was observed in 2015 (Fig. 4-1, bottom panel).
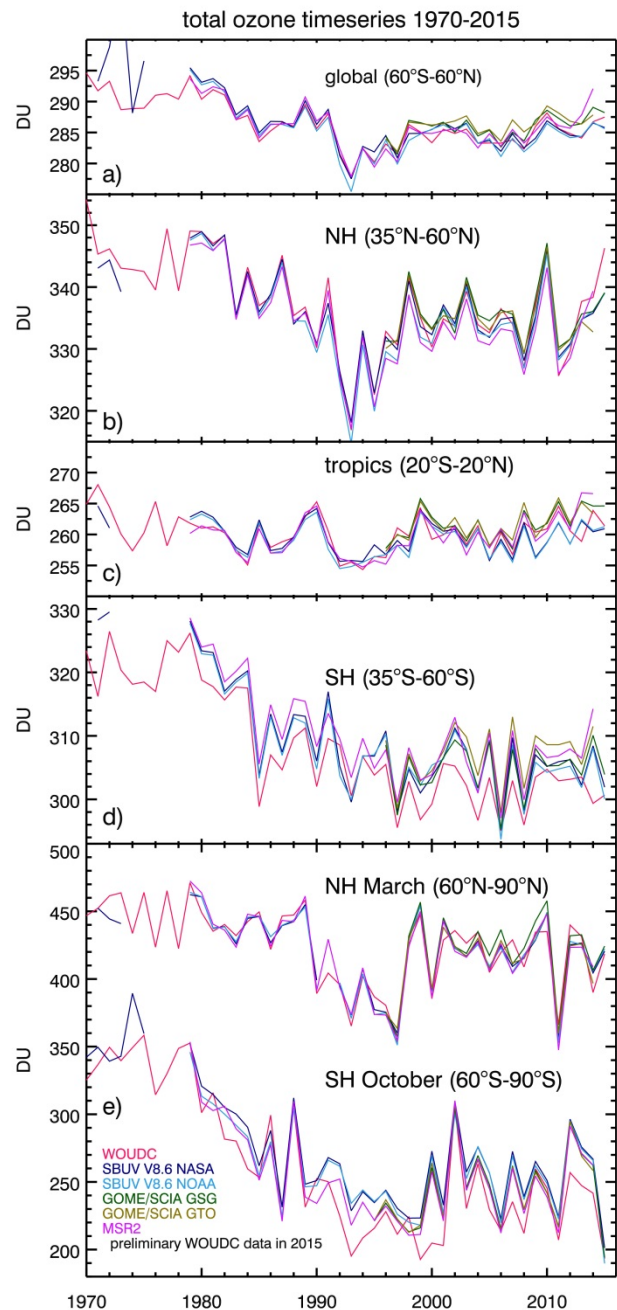

Fig. 4-1: Time series of annual mean total ozone in (a-d) four zonal bands and (e) polar ozone in March (Northern Hemisphere) and October (Southern Hemisphere). Data are from different sources; details see text.

Weaker-than-usual dynamical wave activity in the Southern Hemisphere winter diminished transport from the tropics, reducing ozone at Southern Hemisphere middle latitudes and in the collar region of the polar vortex, and permitting a very stable and cold polar vortex. The high vortex stability and low temperatures resulted in larger-than-usual polar ozone losses and a near-record ozone hole in terms of size and persistence. Ozone annual mean columns at mid- to polar latitudes (35°-90°) in each hemisphere are largely determined by winter/spring ozone levels. These vary considerably with changes in stratospheric meteorological conditions. The year-to-year variability seen in all ozone time series also reflects quasi-biennial oscillation (QBO)-related variations extending from the tropics into the extra-tropics.

In general total ozone columns in 2015 were close to the 1998-2008 average for most of the globe. From Fig. 4-1 it is clear that the Montreal Protocol and its amendments have been successful in stopping the multi-decadal decline in stratospheric ozone by the late 1990s (WMO, 2014). However, at most latitudes, it has not yet been possible to determine a statistically significant increase in total column ozone or lower stratosphere ozone because the expected small increases are masked by large inter-annual variability (e.g., *Coldewey-Egbers et al. 2014*).

In the tropics, no discernible long-term trends in total column ozone have been observed for the entire 1970-2015 period (Fig. 4-1, middle panel). In this region ozone trends in the lower stratosphere are mainly determined by tropical upwelling (related to changes in sea surface temperature). In a changing climate an increase in tropical upwelling is expected which will lead to a continuous decline in ozone (*WMO 2014*).

Comparison with new chemistry climate model simulations
Two simulations performed with version 2.51 of the European Centre for Medium-Range Weather Forecasts – Hamburg (ECHAM) / Modular Earth Submodel System (MESSy) Atmospheric Chemistry (EMAC) model have been confronted with the GTO-ECV data record. A detailed description of the model system and its different setups can be found in *Jöckel et al. (2016)* and references therein. We investigate two hindcast simulations (1980-2013) with specified dynamics, i.e. meteorology nudged towards reanalysis data. The nudging is applied for the prognostic variables divergence, vorticity, temperature, and surface pressure, in which the nudging strength varies with altitude. Sea surface temperatures and sea ice concentrations are taken from reanalysis data, too. The so-called "RC1SD-base-07" simulation includes the nudging of the global mean temperature, whereas this is omitted in the second simulation "RC1SD-base-10". *Jöckel et al. (2016)* provide a first evaluation of the modeled ozone distributions by comparing with observations such as satellite measurements and ozone sonde data. They found that total ozone columns are overestimated for all latitude bands with the bias generally increasing from north to south. The simulation RC1SD-base-07 with temperature nudging agrees better with the observations than the corresponding simulation without nudging the global mean temperature.

Fig. 4-2 shows the monthly mean differences between model simulations and GTO-ECV data (left) and ozone anomalies for simulations and GTO-ECV (right) as a function of time for different latitude bands: 60°N-60°S, 60°N-30°N, 30°N-30°S, and 30°S-60°S, from top to bottom. Anomalies have been calculated with respect to the multi-year average from 1998 to 2012. Total ozone is overestimated for both simulations. The bias is larger in the Southern Hemisphere than in the Northern Hemisphere. Nudging the global mean temperature (RC1SD-base-07, yellow curves) reduces the bias between model and observation, in particular in the tropics and the middle latitudes of the Southern Hemisphere. The reduction in the Northern Hemisphere is smaller, because the bias is reduced only in the troposphere, whereas in the stratosphere it is enlarged (*Jöckel et al. 2016*).

Ozone anomalies (Fig. 4-2, right column) show an excellent agreement between simulations (both nudging versions, yellow and red curves) and observations (green curves). During the overlap period, interannual variability is very well captured by the model system, and extreme values are well reproduced in most cases. As for the latitude bands shown in Fig. 4-2 the model has a positive bias for total ozone columns in both polar regions (not shown). The bias is significantly reduced when the nudging includes the global mean temperature. Furthermore, the model is able to capture ozone anomalies in high latitudes and in extreme cases such as the record low ozone values in the Arctic in March 2011 and in 2002 when the Antarctic vortex was disturbed and split up into two parts.
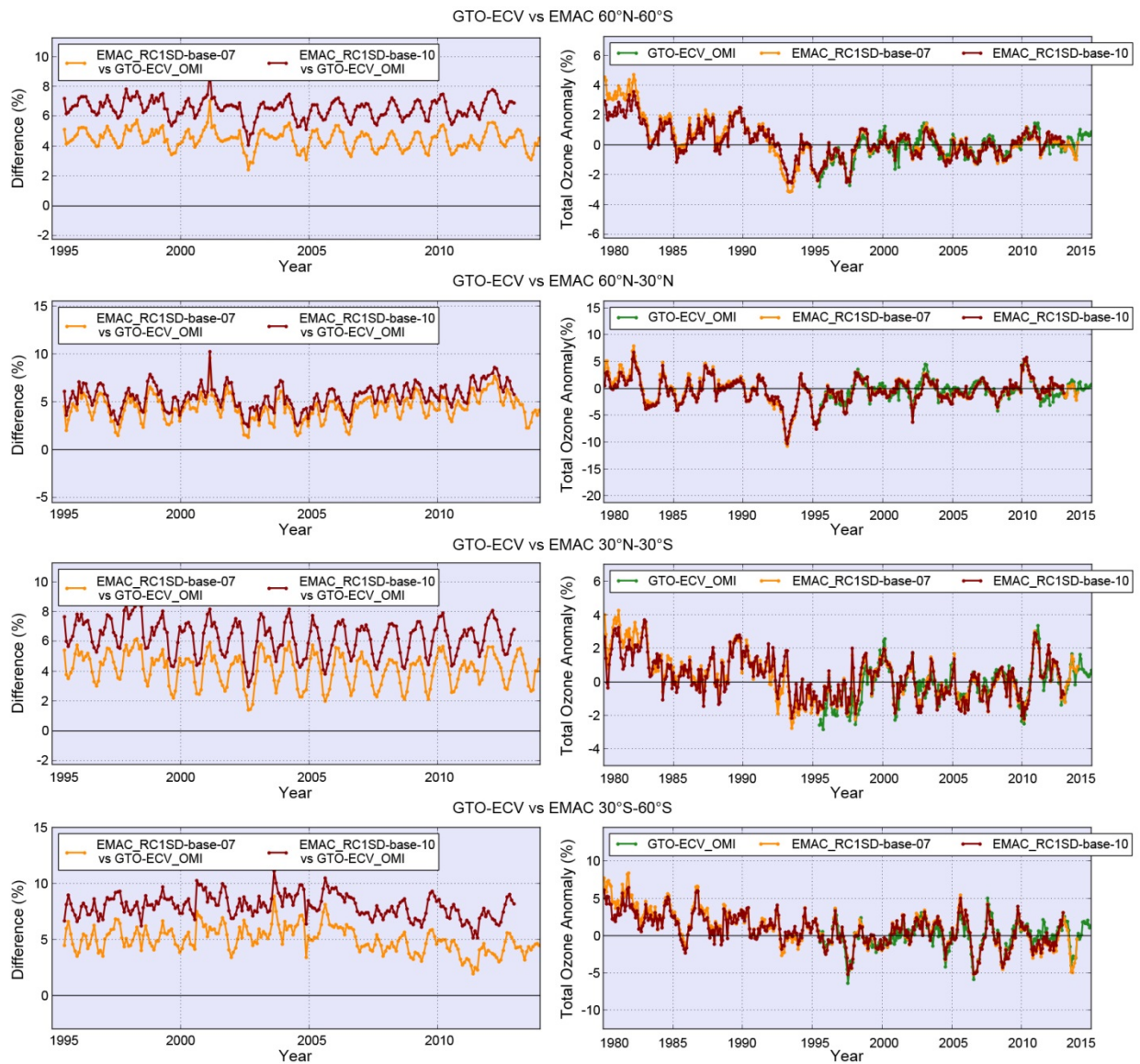
Fig. 4-2: Left column: Difference (%) as a function of time from 1995 to 2013 between EMAC model simulations and GTO-ECV total ozone data. Right column: Total ozone anomalies (%) from 1980 to 2015. From top to bottom: Latitude belts 60°N-60°S, 60°N-30°N, 30°N-30°S, and 30°S-60°S. Red: RC1SD-base-10, yellow: RC1SD-base-07, and green: GTO-ECV satellite data.

References

Coldewey-Egbers, M., Loyola, D., Braesicke, P., Dameris, M., Van Roozendael, M., Lerot, C. and Zimmer, W.: A new health check of the ozone layer at global and regional scales. Geophys. Res. Lett., 41, 4363-4372, doi:10.1002/2014GL060212, 2014.

Coldewey-Egbers, M., Loyola, D., Koukouli, M., et al.: The GOME-type Total Ozone Essential Climate Variable (GTO-ECV) data record from the ESA Climate Change Initiative. Atmos. Meas. Tech., 8, 3923-3940, doi:10.5194/amt-8-3923-2015, 2015.

Jöckel, P., Tost, H., Pozzer, A., Kunze, M., et al.: Earth System Chemistry integrated Modelling (ESCiMo) with the Modular Earth Submodel System (MESSy) version 2.51. Geosci. Model Dev., 9, 1153-1200, doi:10.5194/gmd-9-1153-2016, 2016.

Weber, M., Steinbrecht, W., Roth, C., Coldewey-Egbers, M., et al.: Stratospheric Ozone. In: State of the Climate in 2015. Bull. Amer. Meteor. Soc., 97, 7, S49-S51, 2016.

WMO: Scientific Assessment of Ozone Depletion: 2014. WMO Global Ozone Research and Monitoring Project – Report No. 55, Geneva, Switzerland, 2014.

4.2   Anthropogenic SO₂ Emissions Detected by GOME-2

P. Hedelt

Since the beginning of 2007, the GOME-2 instrument aboard MetOp-A allows for measurements of global anthropogenic and volcanic SO_2 emissions. Now, a decade later, this data represents a huge and continuous repository of SO_2 measurements. Since 2012 the second GOME-2 instrument aboard MetOp-B complements the GOME-2 measurements aboard MetOp-A, allowing for a daily global measurement of SO_2 in Earth's atmosphere. In 2018 the last of the three-satellite EPS programme, MetOp-C, will be launched ensuring that the GOME-2 SO_2 dataset will be growing until at least 2022 when the currently foreseen end of the EUMETSAT Polar System (EPS) mission will be reached.

The SO_2 dataset allows for long-term monitoring of anthropogenic sources, like power plants, metal smelting industries and oil and gas refineries. Anthropogenic SO_2 emissions originate when burning sulfur-contaminated fossil fuels (e.g. sulfur-rich coal) and refining sulfate ores. Anthropogenic SO_2 is predominantly injected into or slightly above the planetary boundary layer (PBL). Although space-borne UV remote sensing is sensitive to the lower atmosphere, strong Rayleigh absorption, O_3 absorption (which interferes with the SO_2 measurements), as well as clouds exacerbate the detection of PBL SO_2 sources. Thus, only very strong anthropogenic SO_2 emissions are visible in daily measurements. This is mostly the case for Norilsk (Northern Russia), one of the most polluted cities in the world (mainly because of intense mining of heavy metals), as well as for the Beijing area in China, with a huge amount of power plants using sulfur-rich coal. These sources provide a total vertical SO_2 column which is close to the GOME-2 SO_2 noise level of about 1 DU. Nevertheless, when averaging over a long timeframe even weak emission sources can be identified.

When averaging GOME-2 SO_2 data over the last 10 years (from January 2007 until the end of 2016) enhanced anthropogenic SO_2 emissions over selected regions become obvious, in which clearly the position of power plants and refineries are visible. For the generation of the regional maps SO_2 total columns retrieved by the GDP4.8 algorithm were used. In order to average the data, a common 0.1° × 0.1° grid was generated and data not flagged as volcanic SO_2 with a cloud-fraction < 0.2 was averaged within a 60 km smoothing radius (see also *Fioletov et al. 2013*). The global catalogue of large SO_2 sources from *Fioletov et al. (2016)* was used to mark the position of power plants, industry and oil and gas refineries in the regional maps presented in Figs. 4-3 to 4-5.

The averaged GOME-2 data in Fig. 4-3 shows increased SO_2 values close to major coal-fired power plants in northern India. They are the dominant SO_2 emission sources in India, often built in the vicinity of large cities. There is no regularization on the emission of SO_2, unlike in the US, Europe and China, hence the installation and operation rate of SO_2 emission control devices is very low. In the recent years, the total installed capacity, power generation and fuel consumption increased dramatically (*Lu et al. 2013*). In the Middle East power plants and industry use abundant oil and gas deposits. The main emission of SO_2 is found in the Persian Gulf (Fig. 4-4), likely from gas flaring from offshore oil and natural gas facilities, which is used to dispose gases such as H_2S for safety, operational and economic reasons (*Krotkov et al. 2016*).

China has the world's highest SO_2 emissions, mainly from coal-fired power plants (responsible for about 70% of its energy consumption). Particularly the industrial areas using sulfur-rich coal in the North China Plain (around 35°N, 118°E), Sichuan Basin (around 28°N, 107°E) as well as close to the megacities around Shanghai (around 32°N, 120°E) are clearly visible in the averaged GOME-2 data shown in Fig 4-5. According to *Li et al. (2010)* and *Lu et al. (2011)* the overall SO_2 loading has decreased over the recent years, mainly attributed to economic recession and emission control measures before the Olympic Games in Beijing in 2008 as well as the increasing installation of de-sulfurization devices.

Our future work will be to calculate time series of SO_2 emissions for those locations displayed in Figs. 4-3 to 4-5 where a clear signal in the averaged GOME-2 data is present. This will permit studying trends in the emissions, a prerequisite for quantifying air pollution and the efficiency of implemented countermeasures.
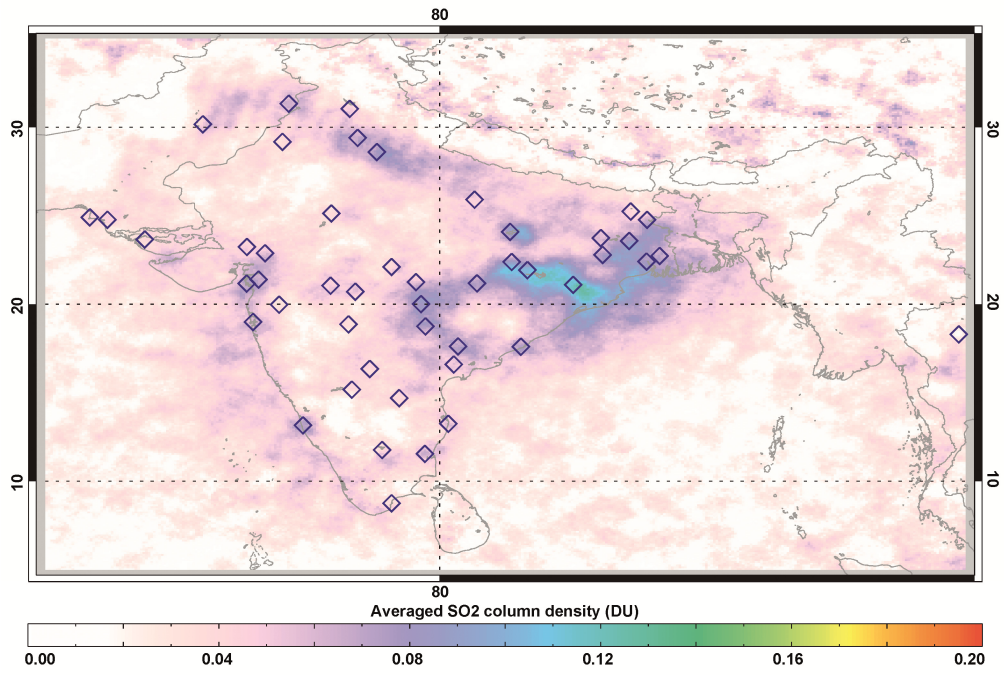
Fig. 4-3: 10 year average GOME-2 SO$_2$ regional map of India. The position of coal-fired power plants is shown.
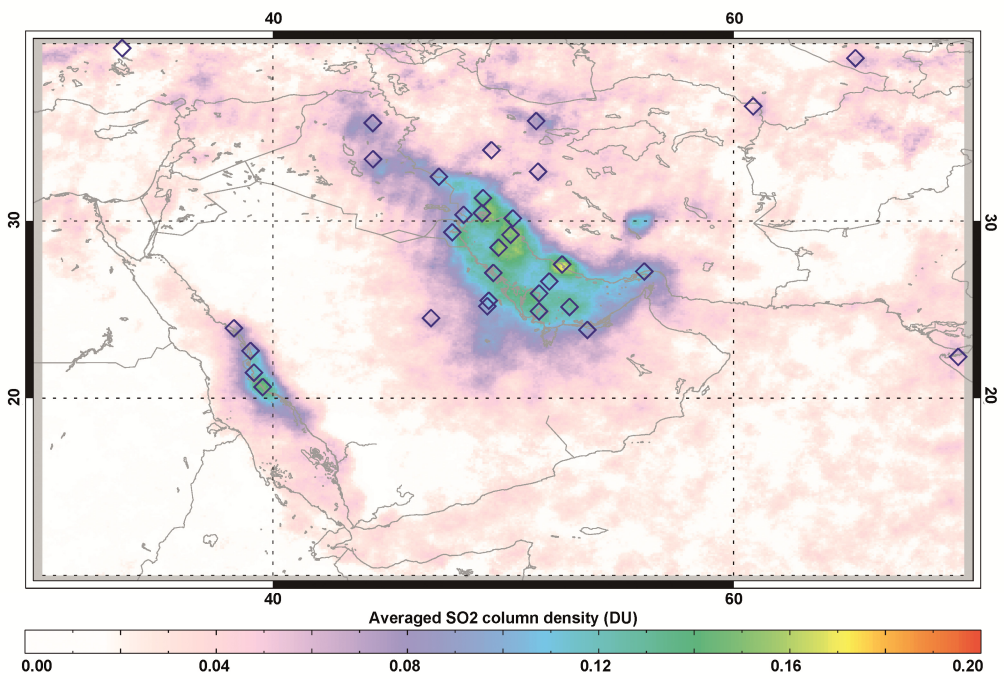
Fig. 4-4: Same as Fig 4-3 but for the Middle East region. The position of a selection of power plants and oil and gas refineries is indicated.
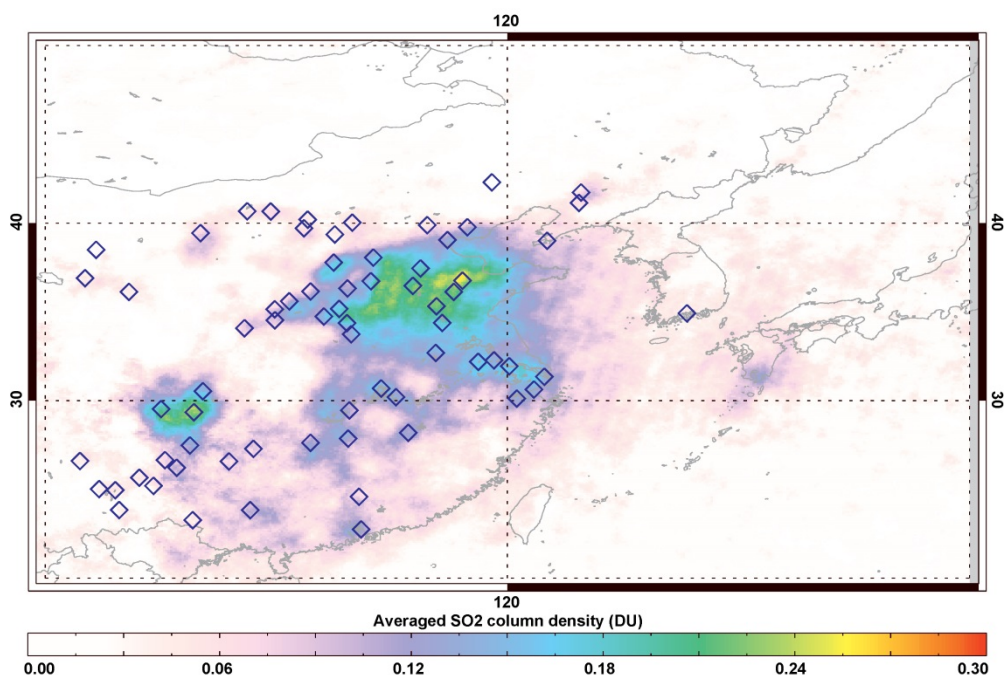
Fig. 4-5: Same as Fig. 4-3 but for China. The position of coal-fired power plants is shown.

References

Fioletov, V., McLinden, C.A., Krotkov, N.A. et al.: A global catalogue of large SO$_2$ sources and emissions derived from the Ozone Monitoring Instrument. Atmos. Chem. Phys., 16, 11497-11519, 2016.

Fioletov, V.E., McLinden, C.A., Krotkov, N.A. et al.: Application of OMI, SCIAMACHY, and GOME-2 satellite SO$_2$ retrievals for detection of large emission sources. J. Geophys. Res.-Atmos., 118, 11399-11418, doi:10.1002/jgrd.50826, 2013.

Krotkov, N.A., McLinden, C.A., Li, C., et al.: Aura OMI observations of regional SO$_2$ and NO$_2$ pollution changes from 2005 to 2015. Atmos. Chem. Phys., 16, 4605-4629, 2016.

Li, C., Zhang, Q., Krotkov, N.A., et al.: Recent large reduction in sulfur dioxide emissions from Chinese power plants observed by the Ozone Monitoring Instrument. Geophys. Res. Lett, 37, L08807, doi:10.1029/2010GL042594, 2010.

Lu, Z, Streets, C.G., De Foy, B.: Ozone Monitoring Instrument observations of interannual increases in SO$_2$ emission from Indian coal-fired power plants during 2005-2012. Environ. Sci. Technol. 47, 13993-14000, doi:10.1021/es4039648, 2013.

Lu, Z., Zhang, Q., Streets, C.G.: Sulfur dioxide and primary carbonaceous aerosol emissions in China and India, 1996-2010. Atmos. Chem. Phys., 11, 9839-9864, doi:10.5194/acp-11-9839-2011, 2011.

4.3 Tropospheric Ozone Columns in Relation to El Niño and Fires

K.-P. Heue, D. Loyola, P. Valks, M. Coldewey-Egbers

The weather phenomenon El Niño changes the sea surface temperature in the Pacific Ocean, which is followed by changes in air pressure, cloud cover distribution and wind directions. Thereby it also affects the tropospheric ozone distribution in the tropics. The largest influence of the El Niño Southern Oscillation (ENSO) is observed over the Pacific Ocean, South East Asia and the Indian Ocean but also South America is affected. In the past this has been used to derive an Ozone ENSO Index (OEI, see *Ziemke et al. 2010*).

El Niño is also known for causing dry winters in South East Asia. This is the traditional burning season in that region, and during El Niño years the fires are often larger and sometimes uncontrolled. Large fires emit ozone precursors such as NOx ($NO+NO_2$) and volatile organic compounds (VOCs). Both the precursors and ozone can be transported over long distances (several 1000 km). Thereby the ozone concentration in the troposphere may be increased.

Tropospheric ozone column data
The retrieval of the tropical tropospheric ozone column (TTOC) based on satellite total ozone observations is described elsewhere (*Valks et al. 2014*, *Heue et al. 2016*). Here we used the data set generated in the framework of ESA's Ozone-CCI project and published in *Heue et al. (2016)*. The convective cloud differential method was applied to the ozone and cloud data from the European satellite instruments GOME, SCIAMACHY, GOME-2A/B and the Dutch-Finnish OMI sensor on NASA's Aura platform. The tropical tropospheric ozone columns between 20°S and 20°N were harmonized with respect to instrumental biases or drifts using SCIAMACHY as reference (*Heue et al. 2016*). Thereby a consistent time series for more than 20 years (1995 to 2015) was created. A typical distribution of the average ozone mixing ratio in June, July, and August is shown in Fig. 4-6.
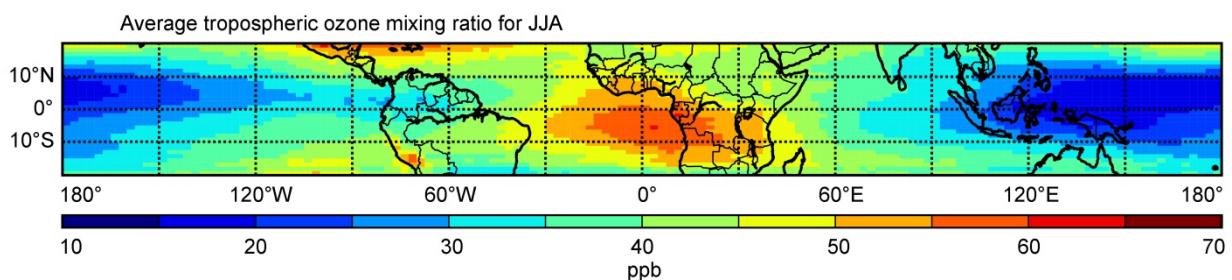
Fig. 4-6: Average tropospheric ozone mixing ratio for the months June, July, and August for the period 1995 to 2015.

Correlations to ENSO and QBO
After the harmonization a trend for 20 years of tropical tropospheric ozone could be derived. We found an increase in tropospheric ozone of 3.5% per decade (*Heue et al. 2016*). The dataset contains additional information on the influence of several climatological parameters on the tropospheric ozone distribution. We calculated the anomalies of the ozone columns and correlated them to the different climatological indices. To determine the anomalies the trend was subtracted, and for each month the data of the last 20 years were averaged. The anomalies equal the differences between the monthly mean ozone column and the de-trended data. The data were averaged to a 5° × 5° resolution.

Fig. 4-7 shows the correlation between the tropospheric ozone column and the Multivariate ENSO Index (MEI, https://www.esrl.noaa.gov/psd/enso/mei/). A strong anti-correlation or correlation was found over the Pacific Ocean, and South East Asia and the Indian Ocean, respectively. When the correlations were compared to those of the Quasi Biennial Oscillation (QBO, http://www.geo.fu-berlin.de/met/ag/strat/produkte/qbo/singapore.dat) it was obvious that the influence of the El Niño on the TTOC is larger compared to the QBO.

Fires
Agricultural and forest fires emit large amounts of NO, NO_2 and VOCs. These species are known to be precursors of tropospheric ozone. Half of the yearly burned area worldwide is burned on the African continent (*Giglio et al. 2013*). Therefore it is not surprising that the maximum in tropospheric ozone is found over Africa and downwind over the Atlantic Ocean (Fig. 4-6).

In a first study we tried to estimate the direct impact of the tropical fires on the TTOC. Burned area data are available from the Global Fire Emissions Database (GFED4) for the period 1996 to 2015 (http://www.globalfiredata.org/, *Giglio et al. 2013*). A Gaussian filter was applied to the fire data to consider transport of ozone and its precursors, thereby also the influence of the fires downwind of the sources, e.g. over oceans, becomes visible. Also the fire data were averaged to a 5° × 5° resolution. We correlated the anomalies in the fire data to the ozone anomalies (as described above).
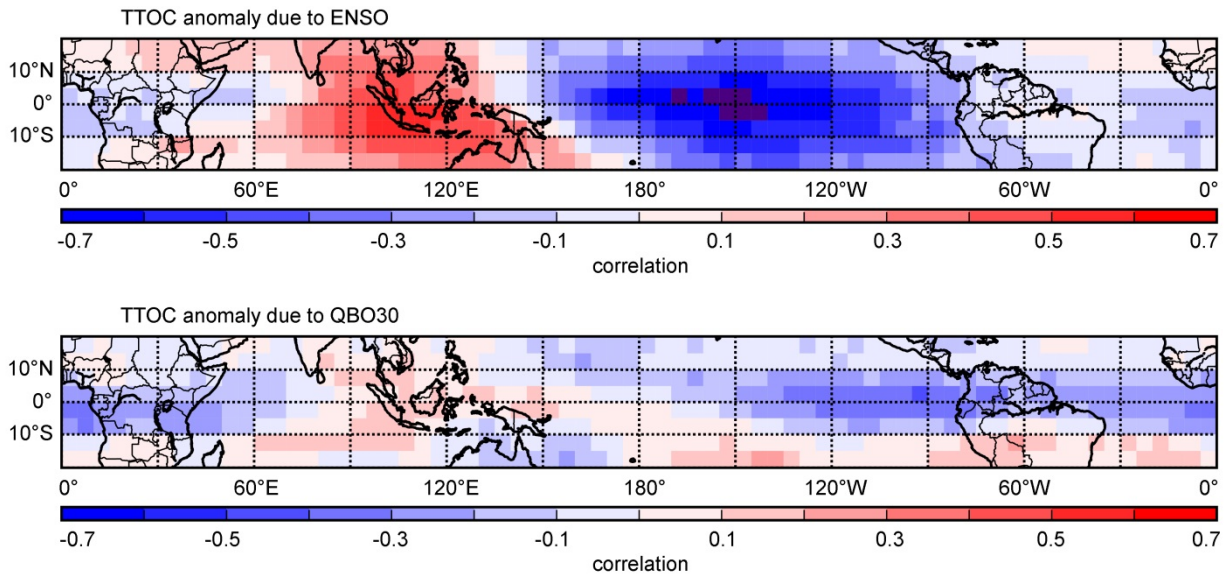
Fig. 4-7: Correlation between the Multivariate ENSO Index (MEI) and the TTOC (top). The bottom panel shows the same plot but for the Quasi Biennial Oscillation index.
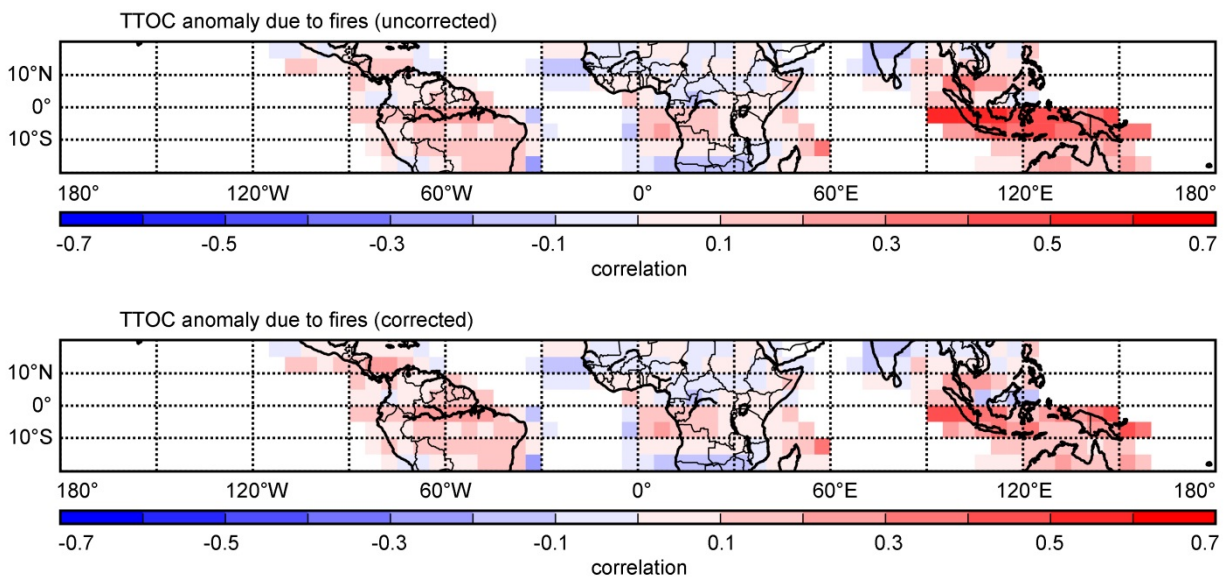
Fig. 4-8: Correlation between tropospheric ozone and burned area. Top: not corrected for ENSO correlations, bottom: corrected for ENSO correlations.

The anomaly correlation plot shown in Fig. 4-8 shows a good correlation between the tropospheric ozone and the burned area over South East and Equatorial Asia. However, for the Amazonian rainforest and also for Africa the correlation is surprisingly low.

The TTOC over Asia correlates with both ENSO (Fig. 4-7) and the fires. The fires in this region also correlate with the El Niño (not shown here). So the weather phenomenon El Niño causes both an anomaly in the fire activity and an anomaly in the tropospheric ozone. On the other hand the enhanced fire activity leads to higher ozone levels. We used the correlation to the ENSO effect to introduce a correction term for both TTOC and fires.

The correlations in South East Asia get slightly worse after introducing this correction term (Fig. 4-8, bottom). For Africa and South America only small changes are observed. Nevertheless the strongest correlations can be observed over Equatorial Asia. For more detailed studies the wind direction will replace the Gaussian filter and the observations of some of the ozone precursors like NO_2 or HCHO might also be taken into account. In Equatorial Asia most of the burned area was covered with forests before the fires, contrary to Africa where roughly 80% had been savanna. Different types of fuel impact the fire emissions and thus the ozone production. However the correlations (Fig. 4-8) over Africa hardly changed if only the forest fires are considered.

Fig. 4-9 shows the linear correlations between the TTOC and the burned area data for three selected grid cells, one for each region of the world. In some cases the correlation is based on a large number of data points close to zero in burned area and TTOC anomaly space and only a few data points correspond to an enhanced burned area.
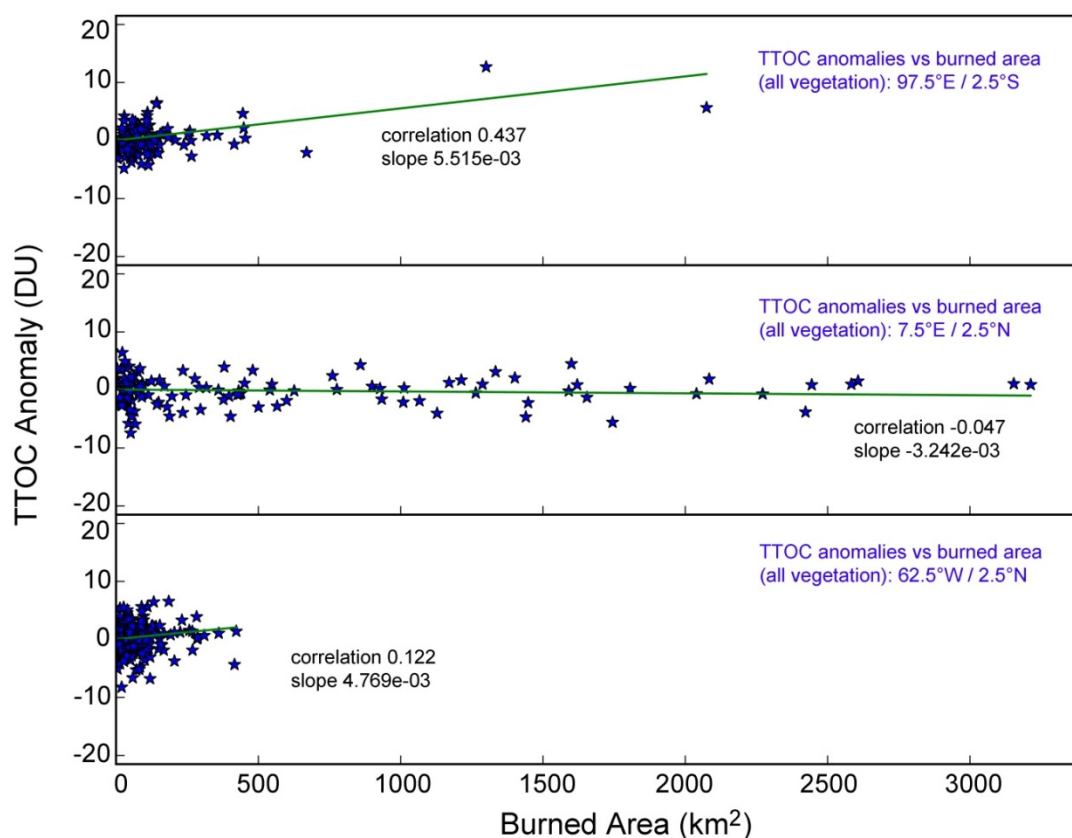
Fig. 4-9: Linear fits for three selected grid points: Indonesia (top), Central Africa (middle), Amazonia (bottom). The GFED4 data set also allows distinguishing between different land cover types. Here only the total burned area is considered.

References

Giglio, L., Randerson, J.T., van der Werf, G.R.: Analysis of daily, monthly, and annual burned area using the fourth-generation global fire emissions database (GFED4). J. Geophys. Res. Biogeosci., 118, 317-328, doi: 10.1002/jgrg.20042, 2013.

Heue, K.-P., Coldewey-Egbers, M., Delcloo, A., Lerot, C., Loyola, D., Valks, P., Van Roozendael, M.: Trends of tropical tropospheric ozone from 20 years of European satellite measurements and perspectives for the Sentinel-5 Precursor. Atmos. Meas. Tech., 9, 5037-5051, doi: 10.5194/amt-9-5037-2016, 2016.

Valks, P., Hao, N., Gimeno García, S., Loyola, D., Dameris, M., Jöckel, P., Delcloo, A.: Tropical tropospheric ozone column retrieval for GOME-2. Atmos. Meas. Tech., 7, 2513-2530, doi: 10.5194/amt-7-2513-2014, 2014

Ziemke, J.R., Chandra, S., Oman, L.D., Bhartia, B.K.: A new ENSO index derived from satellite measurements of column ozone. Atmos. Chem. Phys., 10, 3711-3721, doi: 10.5194/acp-10-3711-2010, 2010.

4.4   SOFIA: Science at 14 km Altitude

M. Hamidouche

SOFIA, the Stratospheric Observatory For Infrared Astronomy, consists of a reflective telescope of 2.5 meter effective diameter mounted in a modified Boeing 747SP aircraft (Fig. 4-10). It is a joint project of NASA and DLR. NASA provided the 747SP highly modified aircraft while DLR delivered the telescope. This telescope assembly was designed and built by the German companies MAN-Technologie and Kayser-Threde under DLR contract. Operations costs and observing time are shared by the United States (80%) and Germany (20%).

Flying at altitudes up to 43.000 ft. (14 km), SOFIA observes from above more than 99% of Earth's atmospheric water vapor at wavelengths ranging from 0.3 μm to 1600 μm (*Hamidouche et al. 2010*). The SOFIA science instrument suite includes imaging cameras and spectrographs as well as imaging cameras with spectrometers. SOFIA's first generation instruments comprise seven sensors – five American and two German. With the variety of its science sensors as well as its capabilities, SOFIA plays a major role in addressing several scientific questions including the study of star and planet formation and the physics and chemistry of the interstellar medium.

Fig. 4-10: The joint DLR and NASA SOFIA observatory flying with the telescope door wide open (top). The bottom panel shows SOFIA on the tarmac of NASA Armstrong (Palmdale) about an hour before take-off for an observing night.

Furthermore, SOFIA contributes considerably to Education and Public Outreach (EPO) by providing students and teachers as well as non-research visitors with a possibility to fly on SOFIA. In fact, SOFIA was designed and has the capability to allow visitors to get close to the working observatory and to interact with astronomers while acquiring and processing astronomical data in flight.

SOFIA flights

SOFIA's home base is Palmdale (California, USA) where it usually takes off and lands. Exceptions exist during special campaigns, e.g. on southern hemisphere flights New Zealand acts as host. A typical flight is characterized as follows: The instrument selected for flight is prepared in the morning before the flight or earlier. The input data required for a successful observation run such as position files, observing scripts, etc. are loaded while the aircraft is still grounded. A few hours before take-off weather conditions are checked again to ensure a safe flight with good observing conditions. SOFIA's maximum flight time is 10 hours from take-off until landing with somewhat shorter timespans in summer. Take-off is scheduled in the evening hours so that observations can occur at night. Once it reaches the flight altitude of 35.000 ft., and after sunset, SOFIA opens the cavity door to expose the telescope to the sky. The observations start about half an hour after the door was opened which allowed the telescope to cool off. A few hours before the end of the flight, SOFIA would reach its highest altitude of 43.000 ft. At the end and an hour before sunrise, the observations finish and the descent starts (*Klein 2011*).

Besides any technical constraints or airspace limitations, the flight plan is dictated by the scheduled astronomical targets. Their positions in the sky are the major parameters in defining the round-trip flight

route. Figure 4-11 shows a flight plan of SOFIA. The plan illustrates different flight legs with their starting times (in UTC) and the name of the observed source during the leg. Each leg is carefully planned for each target based on its coordinates.
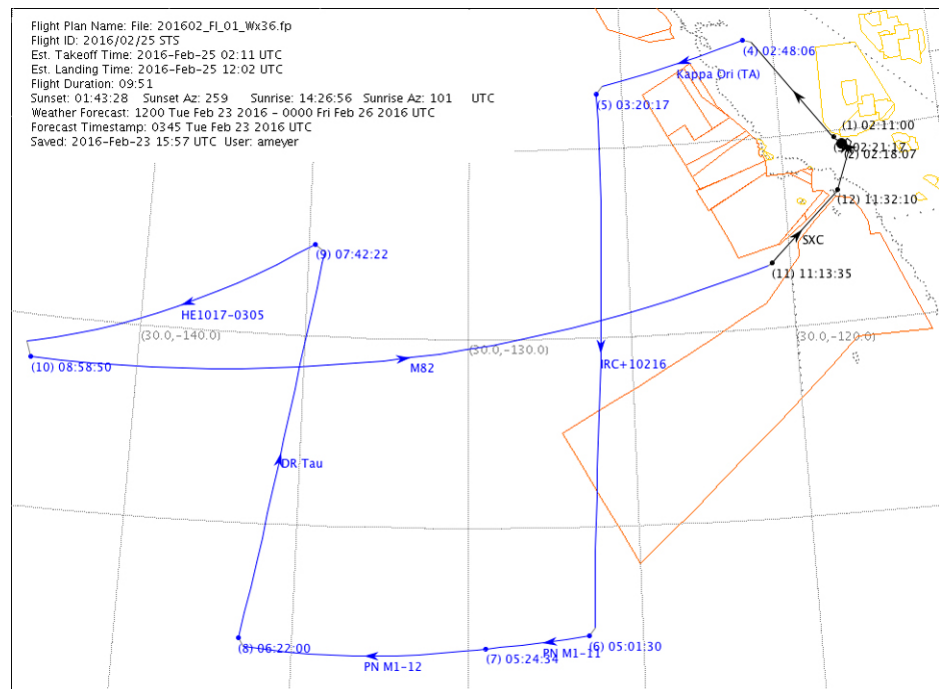
Fig. 4-11: SOFIA flight plan on February 25, 2016. We took-off and landed in Palmdale (California) with spending most of the flight time over the Pacific Ocean. The flight duration was 09:51. The airplane reached its highest altitude of 43.000 ft. at 08:58:50 UTC (Leg 10, target: galaxy M82).

The FIFI-LS instrument

FIFI-LS (Far Infrared Field Imaging Line Spectrometer) is one of SOFIA's national instruments. It was developed by the Max-Planck-Institut für extraterrestrische Physik, University of Stuttgart, and the University of Illinois (USA). FIFI-LS offers simultaneous spectroscopy with two nearly independent channels with a wavelength coverage of 51-110 µm and 110-210 µm at moderate spectral resolution $\lambda/\Delta\lambda \approx$ 1000 to 2000 depending on the wavelength (*Klein et al. 2010*). Each channel has a field of view of 5 × 5 spatial pixels of projected sizes of 6" and 12" in the short-wave and long-wave channel, respectively. The 2D detector contains a 3D-data cube in each channel (Fig. 4-12). The data are a combination of a 2D spatial map and a 1D spectrum, i.e. it provides a far-infrared spectrum per spatial pixel. FIFI-LS can probe different gas components in the far-infrared. Due to its two nearly independent channels, FIFI-LS is able to observe two separate spectral lines of an astronomical source simultaneously.

FIFI-LS was shipped from Stuttgart (Germany) to NASA Armstrong Aircraft Operation Facility in Palmdale (CA, USA) in 2013. It started its commissioning flights aboard SOFIA in 2014. In winter 2016, I joined the SOFIA observing campaign (flight series) with the FIFI-LS instrument aboard (Fig. 4-13) as a guest scientist and to support the SOFIA outreach program, since a group of visitors including

Fig. 4-12: FIFI-LS instrument measurements provide a 3D cube like data. The 2D observations (maps, coordinates XY) can be extracted for each wavelength (λ), i.e. spectral pixel (top slice). Likewise far-infrared measured spectra can be extracted for each spatial pixel (side slice).

reporters and educators with different professional backgrounds participated in this campaign. As a DLR scientist and with SOFIA experience from my previous science activities and collaborations on the FIFI-LS instrument development, my task during this campaign included assisting the outreach program of the campaign by interacting with the visitors, mainly by clarifying the role and the benefits of a stratospheric observatory and how the Earth atmosphere affects ground based observations and blocks infrared radiation from space. It was a real pleasure having been back where I worked in the past. Seeing the FIFI-LS science instrument in action with SOFIA having meanwhile matured to a capable astronomical observatory was really very exciting.
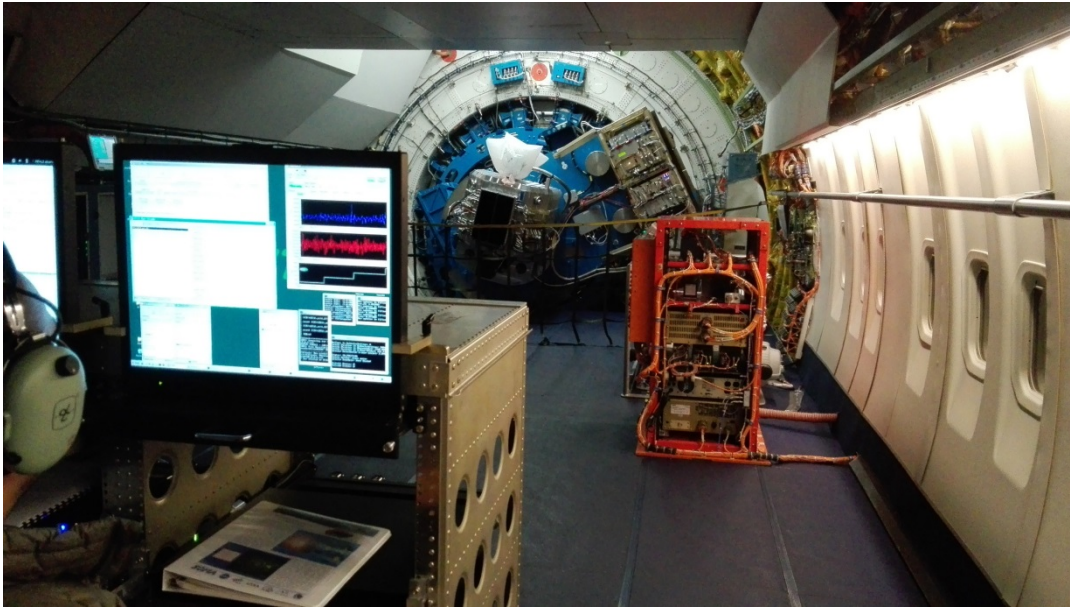
Fig. 4-13: Inside SOFIA during a flight looking towards the back where the telescope is located. FIFI-LS instrument is seen mounted on the telescope focal plane.

References

Hamidouche, M., Young, E., Marcum, P., Krabbe, A.: Stratospheric Observatory for Infrared Astronomy. SF2A Conference Proceedings, 2010.

Klein, R.: SOFIA Flight Planning. First German SOFIA Workshop, Stuttgart, 2011.

Klein, R., Poglitsch, A., Raab, W., Geis, N., Hamidouche, M., Looney, L.W., Hönle, R., Nishikida, K., Genzel, R., Henning, T.K.: FIFI LS getting ready to fly aboard SOFIA. Proceedings of SPIE, 7735, 2010.

4.5 Computational Exploration of Chemical Space for Astrobiology

M. Meringer, H.J. Cleaves (ELSI)

How the transition of disorganized, inanimate matter to organized, living systems took place on our planet and might have occurred on other bodies of our solar system or elsewhere in the universe is one of the fundamental questions studied in the field of Astrobiology. The only instance of life known so far is the terrestrial one, and all living organisms on Earth share many of the same biochemical foundations with respect to reproduction and metabolism. These biochemical foundations rely on a small pool of biomolecules, which represent a minute subset of plausible structural analogs, which themselves form only a very small fraction of all possible chemical compounds in chemical space.

We believe that one key to understanding the origins of life is to study biomolecules in context of their surrounding neighborhood in chemical space. Using unique software tools, so-called structure generators (*Meringer 2010*), we are able to construct well defined subsets of chemical space exhaustively. These virtual compound libraries are then computationally analyzed with respect to the physico-chemical properties of their constituents. The first targets of these studies were amino acids and nucleotide analogs. Results have been published in a series of original research papers (*Meringer et al. 2013, Ilardo et al. 2015, Cleaves et al. 2015*) and a summary of these findings, including some new perspectives, has recently been submitted (*Meringer and Cleaves, submitted*).

While these first studies were focused on the monomeric building blocks of functional biomolecules (DNA and protein), which are responsible for the reproductive and catalytic capabilities of living organisms, our recent research turned towards the core of intermediary metabolism, the tricarboxylic acid (TCA) cycle. The TCA cycle, also known as citric acid cycle, is a cyclic series of chemical reactions used by all aerobic organisms to release stored energy. Its reverse counterpart, the rTCA cycle (Fig. 4-14), operates in several microorganisms, in which it serves as a mechanism for fixing CO_2 into biomass. These microorganisms tend to cluster near the root of the tree of life, suggesting that this was perhaps the original CO_2 fixation process in biology.
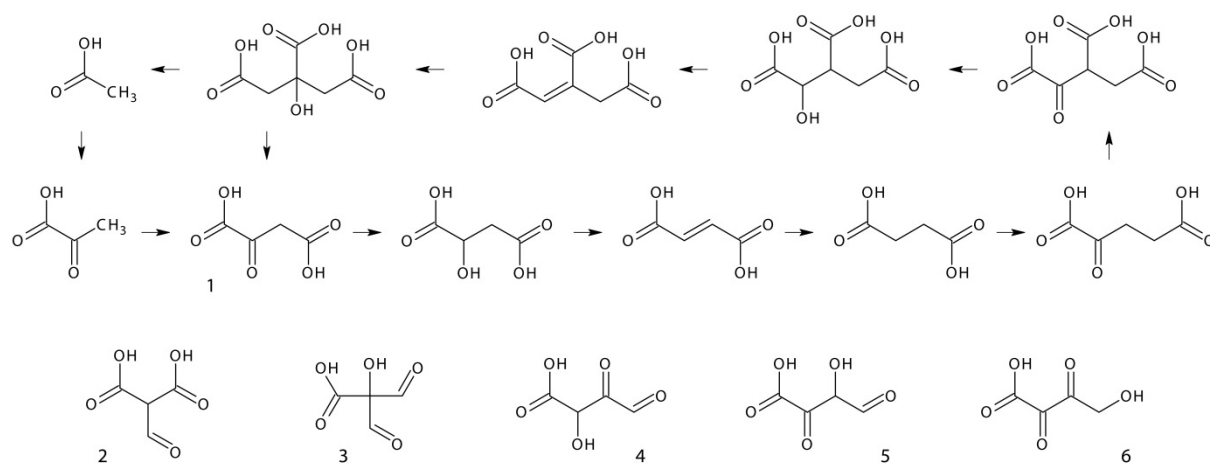
Fig. 4-14: The upper part shows the rTCA cycle as represented in *Morowitz et al. (2000)*. For rTCA cycle member Oxaloacetate (1) there are five more isomers (2-6) present in our generated library. Only one of them (2) is included in today's largest chemical structure databases, PubChem and Reaxys.

In 2000 Morowitz et al. published results of a computer experiment (*Morowitz et al. 2000*) showing that by the use of a simple set of structural constraints derived from physical and chemical considerations, a small set of 153 chemical compounds, including all 11 intermediates of the TCA cycle, were retrieved from the 3.5 million member Beilstein database. That a small number of selection rules could define such a constrained subset of obvious biological importance was considered as evidence that this approach would prove useful in the study of biogenesis.

However, it is well known that structure databases represent only a tiny subset of possible chemical structures, and that among other problems they suffer a certain bias of human interest, e.g. pharmaceutical utility or other economic ambitions (*Meringer and Cleaves, submitted*). In order to

obtain a complete, unbiased picture of the structure space surrounding the rTCA cycle intermediates, we used the structural constraints given in *Morowitz et al. (2000)* as input for our structure generation software. This way we obtained a library of 876 compounds, more than five times larger than the set proposed by Morowitz et al., and still more than three times larger than the union of corresponding compounds in today's most comprehensive structure databases.
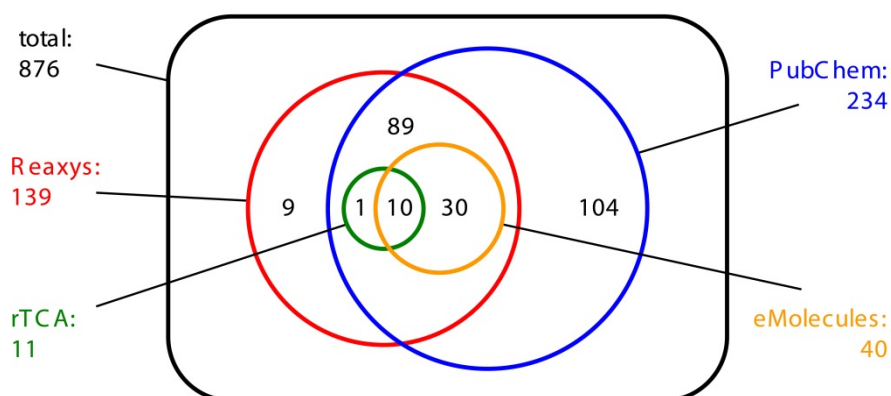
Fig. 4-15: A Venn diagram of our generated library showing subsets covered by chemical structure databases Reaxys (the successor of Beilstein), PubChem (the largest freely accessible structure database), eMolecules (a database of commercially available compounds), and the 11-membered set of rTCA cycle intermediates.

Fig. 4-15 shows a Venn diagram of these sets and the bottom row of Fig. 4-14 depicts isomers of an rTCA cycle intermediate, which are exclusively found in our computer-generated library. Full details of this study are currently prepared for publication (*Meringer and Cleaves, in preparation*). Next steps include the automated search within our generated library for other cyclic chains of reactions that could function as alternatives for the rTCA cycle in metabolisms of biologies beyond the terrestrial one.

References

Meringer, M.: Structure Enumeration and Sampling. Handbook of Chemoinformatics Algorithms. Edited by J.-L. Faulon and A. Bender, Chapman & Hall: 233-267, 2010.

Meringer, M., Cleaves, H.J. and Freeland, S.J.: Beyond Terrestrial Biology: Charting the Chemical Universe of α-Amino Acid Structures. J. Chem. Inf. Model. 53(11): 2851-2862, 2013.

Ilardo, M., Meringer, M., Freeland, S.J., Rasulev, B., Cleaves, H.J.: Extraordinarily Adaptive Properties of the Genetically Encoded Amino Acids. Scientific Reports 5: 9414, 2015.

Cleaves, H.J., Meringer, M., Goodwin, J.T.: 227 Views of RNA: Is RNA Unique in Its Chemical Isomer Space? Astrobiology 15(7): 538-558, 2015.

Meringer, M., Cleaves, H.J.: Exploring Astrobiology Using in Silico Molecular Structure Generation. Submitted to Phil. Trans. R. Soc. A.

Morowitz, H.J., Kostelnik, J.D., Yang, J., Cody, G.D.: The Origin of Intermediary Metabolism. Proc. Natl. Acad. Sci. 94(14): 7704-7708, 2000.

Meringer, M., Cleaves, H.J.: Computational Exploration of the Chemical Structure Space of Possible Reverse Tricarboxylic Acid Cycle Constituents. In preparation.

4.6 Characterization and Retrieval of Atmospheric Parameters of Terrestrial Extrasolar Planets Around Cool Host Stars

F. Schreier, S. Städt, H. Rauer (TU Berlin)

More than two decades after the discovery of the first extra-solar planet there are several thousand exoplanets known, mostly large objects such as "hot Jupiters", but also some Earth-like planets in the habitable zone, i.e. in the region around the host star where the planet could host liquid water on the surface. Characterizing atmospheres of hot Super-Earths orbiting M-dwarf stars is the next logical step in the search for Earth-like worlds. The main challenges are (1) to explore the range of possible conditions (temperature, pressure, composition, etc.) and (2) to retrieve the state of the atmosphere from spectroscopic observations.

A collaborative research project with TU Berlin (TUB), funded by the Deutsche Forschungsgemeinschaft (DFG), has the objective to refine and apply both the chemistry-convection-climate code developed by TUB to study atmospheres near the inner edge of the habitable zone and versatile solvers developed by IMF for the ill-posed inverse problem to estimate atmospheric parameters from spectra. This project continues the collaboration of the research groups in Berlin and Oberpfaffenhofen established 2005 for the analysis of Venus transit observations and further intensified in the framework of the Helmholtz Research Alliance *Planetary Evolution and Life*.

Fig. 4-16: Artist's impression of the super-Earth GJ1214b (Image: ESO/L. Calçada).

Combining the TUB and IMF expertise, the following questions will be addressed with a focus on low-mass, terrestrial planets in the inner part of the habitable zone of M-dwarfs:

- Which are the key parameters affecting climate, habitability, and biosignatures? How do chemistry and climate impact the atmospheres?
- What will atmospheric spectra look like? How are they affected by stellar and planetary properties?
- Which properties can be observed spectroscopically? What atmospheric state parameters can be retrieved by remote sensing?

The three main scenarios to be considered are characterized by different atmospheric conditions:

- Super-Earths with steam atmospheres in the inner habitable zone,
- Super-Earths with H_2-rich atmospheres,
- Super-Earths with CO_2-rich atmospheres.

Apart from further improvements of IMF's high resolution infrared radiative transfer code GARLIC our main work packages are devoted to development and application of the retrieval code:

- State vector definition: The atmosphere is described by continuous functions of altitude, latitude, and longitude describing pressure, temperature and composition that need to be discretized. However, only disk-averaged spectra are available, so a full 1D or even 3D atmospheric representation is unrealistic. Thus, for a manageable inverse problem the parameters to be retrieved have to be carefully selected, i.e. the *atmospheric state vector* should be as small as possible.
- Constraints, a priori and initial guess: In addition to the usual constraints such as positivity or

smoothness, our aim is to identify additional constraints from atmospheric physics and chemistry. A priori information from climatology etc. frequently used in Earth remote sensing is not available here. However, knowledge of the planetary system, e.g. type of central star and orbital parameters, can be used as input for Berlin's 1D coupled radiative-convective-chemical model to generate an atmospheric scenario useful as an initial guess.

- The retrieval code will be developed on the basis of IMF's radiative transfer code and nonlinear (regularizing) least squares solvers. Stochastic methods are a possible alternative, but might be too time consuming for more than a handful of parameters.

- Retrieval runs: For an assessment of physical and instrumental limitations on the retrieval performance, simulations will be conducted with synthetic spectra for different resolutions and noise levels. Furthermore, a re-analysis of disk-averaged spectra of solar system planets (e.g., Earth and Venus) is planned. Finally, exoplanet observations of hot and warm Neptunes and Super-Earths, e.g., GJ1214b or GJ3470b, will be analyzed.

5. Documentation

5.1 Journal Papers

Afanas'ev, V.P., Gryazev, A.S., Efremenko, D., Kaplya, P.S. Ridzel, O.Y.: Determination of atomic hydrogen in hydrocarbons by means of the reflected electron energy loss spectroscopy and the X-ray photoelectron spectroscopy. Journal of Physics: Conference Series, 748 (1), 012005, IOP Publishing. DOI: 10.1088/1742-6596/748/1/012005, 2016.

Afanas'ev, V.P., Gryazev, A.S., Efremenko, D., Kaplya, P.S., Lyapunov, N.V.: Differential inverse inelastic mean free path determination on the base of X-ray photoelectron emission spectra. Surface Investigation X-Ray, Synchrotron and Neutron Techniques, 10 (5), 906-911, DOI: 10.1134/S1027451016050037, 2016.

Afanas'ev, V.P., Efremenko, D.S., Kaplya, P.S.: Analytical and numerical methods for computing electron partial intensities in the case of multilayer systems. Journal of Electron Spectroscopy and Related Phenomena, 210, 16-29, DOI: 10.1016/j.elspec.2016.04.006, 2016.

Beirle, S., Hörmann, C., Jöckel, P., Liu, S., Penning de Vries, M., Pozzer, A., Sihler, H., Valks, P., and Wagner, T.: The STRatospheric Estimation Algorithm from Mainz (STREAM): estimating stratospheric NO2 from nadir-viewing satellites by weighted convolution. Atmos. Meas. Tech., 9, 2753-2779, doi:10.5194/amt-9-2753-2016, 2016.

Boynard, A., Hurtmans, D., Koukouli, M., Goutail, F., Bureau, J., Safieddine, S., Lerot, C., Hadji-Lazaro, J., Wespes, C., Pommereau, J.P., Pazmino, A., Zyrichidou, I., Balis, D., Barbe, A., Mikhailenko, S., Loyola, D., Valks, P., Van Roozendael, M., Coheur, P.-F., Clerbaux, C.: Seven years of IASI ozone retrievals from FORLI: validation with independent total column and vertical profile measurements. Atmos. Meas. Tech., 9 (9), 4327-4353, DOI: 10.5194/amt-9-4327-2016, 2016.

Efremenko, D.S., Schüssler, O., Doicu, A., Loyola, D.: A stochastic cloud model for cloud and ozone retrievals from UV measurements. J. Quant. Spectrosc. & Radiat. Transfer, 184, 167-179, DOI: 10.1016/j.jqsrt.2016.07.008, 2016.

Gottwald, M., Floricioiu, D.: Kryosphäre im Wandel. Polarforschung mit Radarsatelliten. Physik in unserer Zeit, 47 (2), 66-74, DOI: 10.1002/piuz.201690024, 2016.

Gottwald, M.: 184 crateres d'impact sur la Terre. Pour la Science, 90, 26-31, 2016.

Hassinen, S., Balis, D., Bauer, H., Begoin, M., Delcloo, A., Eleftheratos, K., Gimeno García, S., Granville, J., Grossi, M., Hao, N., Hedelt, P., Hendrick, F., Hess, M.l, Heue, K.-P., Hovila, J., Jønch-Sørensen, H., Kalakoski, N., Kauppi, A., Kiemle, S., Kins, L., Koukouli, M., Kujanpää, J., Lambert, J.-C., Lang, R., Lerot, C., Loyola, D., Pedergnana, M., Pinardi, G., Romahn, F., Van Roozendael, M.l, Lutz, R., De Smedt, I., Stammes, P., Steinbrecht, W., Tamminen, J., Theys, N., Tilstra, L.G., Tuinder, O., Valks, P., Zerefos, C.S., Zimmer, W., Zyrichidou, I.: Overview of the O3M SAF GOME-2 operational atmospheric composition and UV radiation data products and data availability. Atmos. Meas. Tech., 9 (2), 383-407, DOI: 10.5194/amt-9-383-2016, 2016.

Heue, K.-P., Coldewey-Egbers, M., Delcloo, A., Lerot, C., Loyola, D., Valks, P., Van Roozendael, M.: Trends of tropical tropospheric ozone from 20 years of European satellite measurements and perspectives for the Sentinel-5 Precursor. Atmos. Meas. Tech., 9, 5037-5051, DOI: 10.5194/amt-9-5037-2016, 2016.

Kalakoski, N., Kujanpää, J., Sofieva, V, Tamminen, J., Grossi, M., Valks, P.: Validation of GOME-2/Metop total column water vapour with ground-based and in situ measurements. Atmos. Meas. Tech., 9, 1533-1544. DOI: 10.5194/amt-9-1533-2016, 2016.

Koukouli, M.E., Balis, D.S., van der A, R J., Theys, N., Hedelt, P., Richter, A., Krotkov, N., Li, C., Taylor, M.: Anthropogenic sulphur dioxide load over China as observed from different satellite sensors. Atmospheric Environment, 145, 45-59. DOI: 10.1016/j.atmosenv.2016.09.007, 2016.

Loyola, D., Pedergnana, M., Gimeno García, S.: Smart sampling and incremental function learning for very large high dimensional data. Neural Networks, 78, 75-87, DOI: 10.1016/j.neunet.2015.09.001, 2016.

Lutz, R., Loyola, D., Gimeno García, S., Romahn, F.: OCRA radiometric cloud fractions for GOME-2 on MetOp-A/B. Atmos. Meas. Tech., 9, 2357-2379, DOI: 10.5194/amt-9-2357-2016, 2016.

Rother, T.: Violation of a Bell-like inequality by a combination of Rayleigh scattering with a Mach-Zehnder setup. J. Quant. Spectrosc. & Radiat. Transfer, 178, 66-76, DOI: 10.1016/j.jqsrt.2015.09.002, 2016.

Safieddine, S., Boynard, A., Hao, N., Huang, F., Wang, L., Ji, D., Barret, B., Ghude, D., Coheur, P.-F., Hurtmans, D., Clerbaux, C.: Tropospheric Ozone Variability during the East Asian Summer Monsoon as Observed by Satellite (IASI), Aircraft (MOZAIC) and Ground Stations. Atmos. Chem. Phys., 15, DOI: 10.5194/acpd-15-31925-2015, 2016.

Schreier, F.: An assessment of some closed-form expressions for the Voigt function. J. Quant. Spectrosc. & Radiat. Transfer, 176, 1-5, DOI: 10.1016/j.jqsrt.2016.02.016, 2016.

Weber, M., Steinbrecht, W., Roth, C., Coldewey-Egbers, M., Degenstein, D., Fioletov, V.E., Frith, S., Froidevaux, L., de Laat, J., Long, C., Loyola, D., Wild, J.: Stratospheric Ozone. In: BAMS State of the Climate in 2015. Bull. Amer. Meteor. Soc., 97(8), 49-51, 2016.

Xu, J., Schreier, F., Doicu, A., Trautmann, T.: Assessment of Tikhonov-type regularization methods for solving atmospheric inverse problems. J. Quant. Spectrosc. & Radiat. Transfer, 184, 274-286, DOI: 10.1016/j.jqsrt.2016.08.003, 2016.

5.2 Conference Presentations

Afanas'ev, V.P., Gryazev, A.S., Efremenko, D., Kaplya, P.S.: Extraction of differential inverse inelastic mean free paths in solids from electron energy loss spectra. International Conference Micro- and Nanoelectronics – 2016, Zvenigorod, Russia, 2016.

Afanas'ev, V.P., Gryazev, A.S., Kaplya, P.S., Ridzel, O.Y., Efremenko, D.: Software tools for profile analysis of multi-layered systems by using the elastic peak electron spectroscopy. 14th International Baltic Conference on Atomic Layer Deposition, St. Petersburg, Russia, 2016.

Coldewey-Egbers, M., Aberle, B., Slijkhuis, S., Loyola, D., Dehn, A.: New GOME Level-1 Product: In-Flight Calibration and Degradation Correction. ESA Atmospheric Composition Validation Evolution (ACVE), Frascati, Italy, 2016.

Coldewey-Egbers, M., Loyola, D., Braesicke, P., Dameris, M., Van Roozendael, M., Lerot, C., Balis, D., Koukouli, M.E.: The extended GOME-type Total Ozone Essential Climate Variable data record - global and regional trends from the past 20 years. ESA Living Planet Symposium, Prague, Czech Republic, 2016.

Coldewey-Egbers, M., Loyola, D., Dameris, M., Braesicke, P., Van Roozendael, M., Lerot, C., Koukouli, M.E., Balis, D.: The ESA-CCI total ozone climate data record 1995-2015: investigation of long-term trends and variability. SPARC Workshop Stratospheric Change and its Role for Climate Prediction (SHARP), Berlin, Germany, 2016.

Coldewey-Egbers, M., Loyola, D., Van Roozendael, M., Lerot, C., Braesicke, P., Dameris, M., Koukouli, M.E., Balis, D., Zehner, C.: The GOME-type Total Ozone Essential Climate Variable - the first 20 years of an accurate global ozone data record (1995-2015). Quadrennial Ozone Symposium (QOS), Edinburgh, United Kingdom, 2016.

Dameris, M., Coldewey-Egbers, M., Loyola, D., Van Roozendael, M.: ESA Climate Change Initiative - Provision of long-term data sets for climate research. ODAS 2016 (ONERA DLR Aerospace Symposium), Oberpfaffenhofen, Germany, 2016.

Delcloo, A., Heue, K.-P., Keppens, A., Coldewey-Egbers, M., Lerot, C., Hubert, D., Verhoelst, T., Loyola, D., Valks, P., Lambert, J.-C., Witte, J., Thompson, A.M., Van Roozendael, M.: Validation Of The ESA-CCI Harmonized Tropospheric Ozone Column Data Product, Using Balloon Sounding Data. ESA Atmospheric Composition Validation Evolution (ACVE), Frascati, Italy, 2016.

Efremenko, D., Loyola, D., Doicu, A., Trautmann, T.: Data-intensive computing in radiative transfer modelling. Big Data from Space (BiDS'16), Santa Cruz de Tenerife, Spain, 2016.

Eichmann, K.-U., Weber, M., Heue, K.-P., Leventiduo, E., Richter, A., Burrows, J.P.: Tropical Upper Tropospheric Ozone Volume Mixing Ratios Retrieved with the Cloud Slicing Method using SCIATRAN/GOME2 data: Methodology, Ozone Sonde Comparisons, and Verification of the new S-5P Operational Processor. ESA Living Planet Symposium, Prague, Czech Republic, 2016.

Gottwald, M., Fritz, T., Breit, H., Schättler, B., Harris, A.: The Global TanDEM-X Digital Elevation Model and the Terrestrial Impact Crater Record. 79th Annual Meeting Meteoritical Society, Berlin, Germany, 2016.

Gottwald, M.: Irdische Einschlagskrater - ein neuer dreidimensionaler Blick. Public Lecture, Munich, 2016.

Gottwald, M., Thomas, F., Breit, H., Schättler, B., Harris, A.: Terrestrial Impact Craters in 3D. 5th TanDEM-X Science Team Meeting, Oberpfaffenhofen, Germany, 2016.

Gretschany, S., Lichtenberg, G., Meringer, M., Theys, N., Lerot, C., Liebing, P., Noël, S., Dehn, A., Fehr, T.: New Developments in the SCIAMACHY L2 Ground Processor. EGU General Assembly, Vienna, Austria, 2016.

Gretschany, S., Lichtenberg, G., Meringer, M., Theys, N., Lerot, C., Liebing, P., Noël, S., Dehn, A., Fehr, T.: New Developments in the SCIAMACHY L2 Ground Processor. ESA Living Planet Symposium, Prague, Czech Republic, 2016.

Gretschany, S., Lichtenberg, G., Meringer, M., Theys, N., Lerot, C., Eichmann, K.U.: New Developments in the SCIAMACHY L2 Ground Processor. ESA Atmospheric Composition Validation Evolution (ACVE), Frascati, Italy, 2016.

Hamidouche, M., Gimeno García, S., Schreier, F., Meringer, M., Lichtenberg, G., Hochstaffl, P., Trautmann, T.: Atmospheric methane with SCIAMACHY: Operational Level 2 data analysis and verification. ESA Living Planet Symposium, Prague, Czech Republic, 2016.

Hamidouche, M.: Infrared Astronomy: Star formation and SOFIA. Carl Cranz Gesellschaft: Infrarottechnik, Lecture, Weßling, Germany, 2016.

Hao, N., Ding, A., Safieddine, S., Valks P., Clerbaux, C., Trautmann, T.: Assessment of the Impact of The East Asian Summer Monsoon on the Air Quality Over China. EGU General Assembly, Vienna, Austria, 2016.

Hao,N., Loyola, D., Van Roozendael, M., Lerot, C., Valks, P., Spurr, R.J.D., Koukouli, M.E., Zyrichidou, I., Zimmer, W., Balis, D.S.: Improvement of the operational Near-Real-Time total ozone retrieval algorithm for GOME-2 on MetOp-A & MetOp-B and perspectives for TROPOMI/S5P. EUMETSAT Meteorological Satellite Conference, Darmstadt, Germany, 2016.

Hao, N., Loyola, D., Van Roozendael, M., Lerot, C., Valks, P., Spurr, R.J.D., Koukouli, M.E., Zyrichidou, I., Zimmer, W., Balis, D.S.: Developments of the operational Near-Real-Time total ozone retrieval algorithm for GOME-2 and TROPOMI. ESA Living Planet Symposium, Prague, Czech Republic, 2016.

Hao, N., Ding, A., Safieddine, S., Valks P., Clerbaux, C., Risse E., Städt S., Trautmann, T.: Assessment of the Impact of The East Asian Summer Monsoon on the Air Quality Over China. Dragon 3 Final Results and Dragon 4 KO Symposium, Wuhan, China, 2016.

Hao, N., Loyola, D., Van Roozendael, M., Lerot, C., Valks, P., Spurr, R.J.D., Koukouli, M.E., Zyrichidou, I., Zimmer, W., Balis, D.S.: Improvement of the operational Near-Real-Time total ozone retrieval algorithm for GOME-2 on MetOp-A & MetOp-B and perspectives for TROPOMI/S5P. Quadrennial Ozone Symposium (QOS), Edinburgh, United Kingdom, 2016.

Hedelt, P., Valks, P., Loyola, D.: Monitoring volcanic SO2 emissions using GOME-2/Metop-A & -B. 2nd Workshop on the Physics of Volcanoes, Mainz, Germany, 2016.

Hedelt, P., Valks, P., Loyola, D.: Monitoring volcanic SO2 emissions using GOME-2/Metop-A & -B. ESA Living Planet Symposium, Prague, Czech Republic, 2016.

Heue, K.-P., Coldewey-Egbers, M., Valks, P., Loyola, D., Van Roozendael, M., Lerot, C.: Investigation of trends in tropical tropospheric ozone columns derived from CCD satellite data. ESA Living Planet Symposium, Prague, Czech Republic, 2016.

Heue, K.-P., Loyola, D., Valks, P.: Tropospheric Ozone from GOME_2 in combination with other stratospheric ozone measurements. Quadrennial Ozone Symposium (QOS), Edinburgh, United Kingdom, 2016.

Heue, K.-P., Hao, N., Valks, P., Loyola, D., Raphoe, N., Delcloo, A., Lerot, C., Van Roozendael, M.: Tropical Tropospheric Ozone from GOME 2 and Extension to the Extra Tropics. EUMETSAT Meteorological Satellite Conference, Darmstadt, Germany, 2016.

Hochstaffl, P., Hamidouche, M., Schreier, F., Gimeno García, S., Lichtenberg, G.: Validation of Carbon Monoxide and Methane Vertical Column Densities Retrieved from SCIAMACHY Infrared Nadir Observations. EGU General Assembly, Vienna, Austria, 2016.

Hochstaffl, P., Gimeno García, S., Schreier, F., Hamidouche, M., Lichtenberg, G.: Validation of Carbon Monoxide Vertical Column Densities Retrieved from SCIAMACHY Infrared Nadir Observations. ESA Living Planet Symposium, Prague, Czech Republic, 2016.

Koukouli, M.E., Balis, D.S., Zyrichidou, I., van der A, R., Ding, J., Hedelt, P., Valks, P., Fioletov, V.: Area Sulphur Dioxide Emissions over China Extracted from GOME2/MetopA Observations. ESA Living Planet Symposium, Prague, Czech Republic, 2016.

Lerot, C., Danckaert, T., Van Roozendael, M., Koukouli, M.L., Balis, D., Spurr, R., Loyola, D., Coldewey-Egbers, M.: Improved Algorithm Baseline for the Generation of Total Ozone Climate Data Records: Application to GOME and OMI. ESA Atmospheric Composition Validation Evolution (ACVE), Frascati, Italy, 2016.

Lerot, C., Danckaert, T., Van Roozendael, M., Spurr, R., Loyola, D. Coldewey-Egbers, M., Koukouli, M., and Balis, D.: An improved soft-calibration approach for total ozone climate data record generation from GOME, SCIAMACHY, GOME-2 and OMI sensors, ESA Living Planet Symposium, Prague, Czech Republic, 2016.

Lerot, C., Danckaert, T., Van Roozendael, M., Spurr, R., Loyola, D., Coldewey-Egbers, M., Koukouli, M., and Balis, D.: Improved algorithm baseline for the generation of total ozone climate data records: application to OMI. Quadrennial Ozone Symposium (QOS), Edinburgh, United Kingdom, 2016.

Lichtenberg, G., Hamidouche, M., Schreier, F., Hochstaffl, P., Meringer, M.: SCIAMACHY: Spectral Calibration in the SWIR Channels. ESA Atmospheric Composition Validation Evolution (ACVE), Frascati, Italy, 2016.

Lichtenberg, G., Slijkhuis, S., Aberle, B., Scherbakov, D., Meringer, M., Noël, S., Bramstedt, K., Liebing, P., Bovensmann, H., Snel, R., Krijger, M., Van Hees, R., van der Meer, P., Lerot, C., Dehn, A., Fehr, T.: SCIAMACHY: The new Level 0-1 Processor. ESA Atmospheric Composition Validation Evolution (ACVE), Frascati, Italy, 2016.

Lichtenberg, G., Slijkhuis, S., Aberle, B., Scherbakov, D., Meringer, M., Noël, S., Bramstedt, K., Liebing, P., Bovensmann, H., Snel, R., Krijger, M., Van Hees, R., van der Meer, P. Lerot, C., Dehn, A., Fehr, T.: SCIAMACHY: The new Level 0-1 Processor. ESA Living Planet Symposium, Prague, Czech Republic, 2016.

Lichtenberg, G., Slijkhuis, S., Aberle, B., Scherbakov, D., Meringer, M., Noël, S., Bramstedt, K., Liebing, P., Bovensmann, H., Snel, R., Krijger, M., Van Hees, R., van der Meer, P., Lerot, C., Dehn, A., Fehr, T.: SCIAMACHY: The new Level 0-1 Processor. EGU General Assembly, Vienna, Austria, 2016.

Liu, S., Valks, P., Pinardi, G., De Smedt, I., Yu, H., Beirle, S.: Improvement of Total and Tropospheric NO_2 Column Retrieval for GOME-2. EGU General Assembly, Vienna, Austria, 2016.

Liu, S., Valks, P., Pinardi, G., De Smedt, I., Yu, H., Beirle, S.: An improved total and tropospheric NO_2 column retrieval for GOME-2. ESA Living Planet Symposium, Prague, Czech Republic, 2016.

Liu, S., Valks, P., Pinardi, G., De Smedt, I., Yu, H., Beirle, S.: An improved total and tropospheric NO_2 retrieval algorithm for GOME-2. EUMETSAT Meteorological Satellite Conference, Darmstadt, Germany, 2016.

Meringer, M.: 50 Years of Chemical Space Exploration Through Computation. GRC Origins of Life, Galveston, Texas, United States, 2016.

Meringer, M.: 50 Years of Virtual Chemical Space Exploration for Astrobiology. ELSI Seminar, Tokyo, Japan, 2016.

Meringer, M., Cleaves, H.J., Freeland, S.J.: Generation of Virtual Amino Acid Libraries for Multiple Applications in Astrobiology. Galveston, Texas, United States, 2016.

Molina García, V., Yang, Y., Doicu, A., Loyola, D.: Radiative transfer model for operational retrieval of cloud parameters from DSCOVR-EPIC measurements. AGU Fall Meeting, San Francisco, United States, 2016.

Plank, S., Hedelt, P., Paproth, C., Fischer, C., Kerr, G., Twele, A., Martinis, S.: Monitoring of active volcanoes by means of multi-sensor remote sensing – a case study of the 2014/15 Holuhraun fissure eruption. 2nd Workshop on the Physics of Volcanoes, Mainz, Germany, 2016.

Schreier, F., Gimeno García, S., Xu, J.: Py4CAtS - PYthon for Computational ATmospheric Spectroscopy. ASA – HITRAN Conference, Reims, France, 2016.

Schreier, F., Vasquez, M., Gimeno García, S., Kitzmann, D.: Thermal Infrared Emission Spectra of Terrestrial Exoplanets Influenced by Multi-layer Clouds. EGU General Assembly, Vienna, Austria, 2016.

Schreier, F.: Atmosphärische IR-Fernerkundung – Strahlungstransport und Inversion. Carl Cranz Gesellschaft: Infrarottechnik, Lecture, Weßling, Germany, 2016.

Van Roozendael, M., Lambert, J.-C., Lerot, C., Hubert, D., Keppens, A., Balis, D., Koukouli, M., Braesicke, P., Laeng, A., Stiller, G., Coheur, P.-F., Clerbaux, C., Pommereau, J.-P., Dameris, M., Loyola, D., Coldewey-Egbers, M., Heue, K.-P., Weber, M., Rahpoe, N., Siddans, R., Miles, G., Sofieva, V., Tamminen, J., van der A, R., van Peet, J., van Weele, M., Stuebi, R., Degenstein, D., Walker, K., Lopez-Puertas, M., and Zehner, C.: Overview of the main achievements of the Ozone Climate Change Initiative Project. ESA Living Planet Symposium, Prague, Czech Republic, 2016.

Wang, Z., Hao, N., Hendrick, F., Van Roozendael, M., Holla, R., Doicu, A., Valks, P.: Long-term MAX-DOAS measurement of trace gases and aerosol in the Environmental Research Station Schneefernerhaus. EGU General Assembly, Vienna, Austria, 2016.

Xu, J., Schreier, F., Doicu, A., Trautmann, T., Birk, M., Wagner, G.: Stratospheric Profiling of HDO from Far Infrared Limb Measurements by TELIS. ESA Living Planet Symposium, Prague, Czech Republic, 2016.

Xu, J., Schreier, F., Kenntner, M., Szajkowski, M., Fix, A., Trautmann, T.: Towards the Temperature Retrieval by Using Airborne Microwave Radiometer Data. ESA Living Planet Symposium, Prague, Czech Republic, 2016.

Xu, J., Schreier, F., Loyola, D., Schüssler, O., Doicu, A., Trautmann, T.: Monitoring ozone in different spectral regimes from space and balloon (Sentinel-4/-5P, TELIS). IGARSS 2016, Beijing, China, 2016.

5.3 Attended Conferences

GRC Origins of Life, Galveston, Texas, United States, 17-22 January 2016.

SPARC Stratospheric Change and its Role in Climate Prediction (SHARP) workshop, Berlin, Germany, 16-19 February 2016.

2nd Workshop on the Physics of Volcanoes, Mainz, Germany, 4. March 2016.

Big Data from Space (BiDS'16), Santa Cruz de Tenerife, Spain, 15-17 March 2016.

ELSI Seminar, Tokyo, Japan, 4 April 2016

European Geosciences Union General Assembly 2016, Vienna, Austria, 17-22 April 2016.

ESA Living Planet Symposium 2016, Czech Republic, Prague, 9-13 May 2016.

Dragon 3 Final Results and Dragon 4 KO Symposium, Wuhan, China, 4-8 July, 2016.

79th Annual Meeting Meteoritical Society 2016, Berlin, Germany, 7-12 August 2016.

ASA – HITRAN Conference, Reims, France, 24-26 August 2016.

Quadrennial Ozone Symposium (QOS), Edinburgh, UK, 4-9 September 2016.

EUMETSAT 2016 - Meteorological Satellite Conference, Darmstadt, Germany, 26-30 September 2016.

5th TanDEM-X Science Team Meeting, Oberpfaffenhofen, Germany, 17-20 October 2016.

ESA Atmospheric Composition Validation and Evolution (ACVE), Frascati, Italy, 18-20 October 2016.

AGU Fall Meeting, San Francisco, California, USA, 12-16 December 2016.

5.4 Academic Degrees

Master Thesis

Hochstaffl, P.: Validation of Carbon Monoxide Total Columns from SCIAMACHY Near Infrared Nadir Spectra with NDACC/TCCON Ground-Based Measurements. Master thesis, Institute of Atmospheric and Cryospheric Sciences, University of Innsbruck, completed in February 2016. (Supervisors: Dr. F. Schreier and Prof. Dr. T. Karl, University Innsbruck)

Montes Rubio, R.: Improvement on GOME-2 Satellite Retrieval on the Study of Tropospheric Air Pollutants over China. Master thesis, Universitat Politècnica de València, Spain. (Supervisors: Dr. Nan Hao and Dr. Sergio Hoyas Calvo, Universitat Politècnica de València)

Risse, E.-A.: Modelling air-pollution in Beijing: Emission reduction vs. meteorological influence. Master thesis, Technical University of Berlin, completed in April 2016. (Supervisors: Dr. N. Hao, Prof. Dr. T. Trautmann and Prof. Dr. J. Sesterhenn, Technical University of Berlin)

Städt, S.: Mini MAX-DOAS measurements of air pollutants over China. Master thesis, Free University of Berlin, completed in May 2016. (Supervisors: Dr. N. Hao, Prof. Dr. T. Trautmann and Prof. Dr. J. Fischer, Free University of Berlin)

Szajkowski, M.: Development of pre- and post-processing tools for the analysis of microwave temperature profiling observations. Master thesis, Wroclaw University of Technology, completed in September 2016. (Supervisors: Dr. F. Schreier and Prof. Dr. W. Urbańczyk, Wroclaw University of Technology)

Xu, H.: Impact of molecular absorption spectroscopy data on methane retrieved from SCIAMACHY and GOSAT shortwave infrared. Master thesis, Department of Electrical and Computer Engineering, Technical University of Munich. (Supervisors: Dr. F. Schreier and Prof. Dr.-Ing. J. Chen, Technical University of Munich)

Zhang, J.: Estimation of Atmospheric Temperature Using Airborne Microwave Remote Sensing. Master thesis, Faculty of Civil, Geo and Environmental Engineering, Technical University of Munich, (Supervisors: Dr.-Ing. J. Xu and PD Dr. A. Doicu)

Dissertation

Hochstaffl, P.: Trace gas concentration retrieval from near infrared nadir sounding spaceborne spectrometers. Dissertation, Faculty of Physics, Ludwig-Maximilians-Universität Munich (Supervisors: Dr. F. Schreier and Prof. Dr. A. Butz, Ludwig-Maximilians-Universität Munich)

Liu, S.: Improvement of total and tropospheric NO_2 column retrieval for GOME-2. Dissertation, Faculty of Civil, Geo and Environmental Engineering, Technical University of Munich. (Supervisors: Dr. P. Valks and PD Dr. A. Doicu)

Molina García, V.: Satellite measurements of cloud properties. Dissertation, Faculty of Civil, Geo and Environmental Engineering, Technical University of Munich. (Supervisor: PD Dr. A. Doicu)

Sasi, S.: Derivation of aerosols and surface properties from UV satellite measurements. Dissertation, Faculty of Civil, Geo and Environmental Engineering, Technical University of Munich. (Supervisor: PD Dr. A. Doicu)

Städt, S.: Retrieval of atmospheric parameters of terrestrial extrasolar planets around cool host stars. Dissertation, Technical University of Berlin. (Supervisors: Dr. F. Schreier, Prof. H. Rauer, Technical University of Berlin)

Wang, Z.: MAX-DOAS observations of trace gases and aerosol from the Environmental Research Station Schneefernerhaus. Dissertation. Faculty of Civil, Geo and Environmental Engineering, Technical University of Munich. (Supervisors: Dr. N. Hao and PD Dr. A. Doicu)

Annex: Abbreviations and Acronyms

AC	Atmospheric Composition
ACVE	Atmospheric Composition Validation and Evolution
ADAM	A Surface Reflectance Database for ESA's Earth Observation Missions
ADM-Aeolus	Atmospheric Dynamics Mission Aeolus
AISP	Annotated Instrument Source Packet
ALADIN	Atmospheric Laser Doppler Instrument
AMF	Air Mass Factor
AOCS	Attitude and Orbit Control System
ATBD	Algorithm Theoretical Baseline Document
ATLAS-3	Atmospheric Laboratory for Applications and Science
ATP	Atmosphärenprozessoren
bePRO	profiling tool developed by BIRA-IASB
BIRA-IASB	Belgisch Instituut voor Ruimte-Aëronomie / Institut d'Aéronomie Spatiale de Belgique
BIRRA	Beer Infrared Retrieval Algorithm
BU	Binary Unit
CAMS	Copernicus Atmospheric Monitoring Service
CCD	Charged Coupled Device
CCI	Climate Change Initiative
CDOP	Continuous Development and Operations Phase
CE-DOAS	Cavity Enhanced DOAS
CESAR	Cabauw Experimental Site for Atmospheric Research
CF	Climate Forecast
CINDI	Cabauw Intercomparison Campaign for Nitrogen Dioxide Measuring Instruments
CKD	Calibration Key Data
cL0	Consolidated Level 0
CNES	Centre Nationale d'Études Spatiales
CPU	Central Processing Unit
DAOD	Differential Absorption Optical Depth
DEM	Digital Elevation Model
DFD	Deutsches Fernerkundungsdatenzentrum
DFG	Deutsche Forschungsgemeinschaft
DISORT	Discrete Ordinate Method Radiative Transfer
DLR	Deutsches Zentrum für Luft- und Raumfahrt
DNA	Deoxyribonucleic Acid
DOAS	Differential Optical Absorption Spectroscopy
DOASIS	DOAS Intelligent System
DOM	Discrete Ordinate Method
DOME	Discrete Ordinate with Matrix Exponential
DP	Discrepancy Principle
DSCD	Differential Slant Column Densities
DSCOVR	Deep Space Climate Observatory
DU	Dobson Unit
E2S	End-to-End Simulator
ECHAM	European Centre for Medium-Range Weather Forecasts – Hamburg
ECV	Essential Climate Variable
EEE	Expected Error Estimation
ELC	Equivalent Lambertian Cloud
ELSI	Earth-Life Science Institute
EMAC	ECHAM/MESSy Atmospheric Chemistry
ENSO	El Niño Southern Oscillation
ENVISAT	Environmental Satellite
EOC	Earth Observation Center
EPIC	Earth Polychromatic Imaging Camera

EPO	Education and Public Outreach
EPS	EUMETSAT Polar System
ERS	European Remote Sensing Satellite
ESA	European Space Agency
ESL	Expert Support Laboratory
ESO	European Southern Observatory
ESOC	European Space Operation Center
ESRIN	European Space Research Institute
ESTEC	European Space Research and Technology Center
EUMETSAT	European Organisation for the Exploitation of Meteorological Satellites
FCDR	Fundamental Climate Data Record
FFT	Fast Fourier Transform
FIFI-LS	Far Infrared Field Imaging Line Spectrometer
FWHM	Full Width Half Maximum
GARLIC	Generic Atmospheric Radiation Line-by-Line Infrared Code
GCOS	Global Climate Observing System
GCV	Generalized Cross-Validation
GDP	GOME Data Processor
GFED	Global Fire Emissions Database
GOME	Global Ozone Monitoring Experiment
GTO	GOME-type Total Ozone
HITRAN	High-resolution Transmission
HKTM	Housekeeping Telemetry
HSS	High Speed Sampling
HT	Hartmann-Tran
IMAGES	Intermediate Model of Global Evolution of Species
IMF	Institut für Methodik der Fernerkundung
IPA	Institut für Physik der Atmosphäre
IPDA	Integrated Path Differential Absorption
ISRF	Instrument Spectral Response Function
IUP-IFE	Institut für Umweltphysik / Institut für Fernerkundung
KNMI	Koninklijk Nederlands Meteorologisch Instituut
L0	Level 0
L1	Level 1
L1	Lagrangian Point 1
L1a	Level 1a
L1b	Level 1b
L2	Level 2
L2WG	Level 2 Working Group
LbL	Line-by-Line
LC	L-Curve
LIDORT	Linearized Discrete Ordinate Radiative Transfer
LMU	Ludwig-Maximilians-Universität
LoS	Line of Sight
LP-DOAS	Long Path DOAS
LTM	Long-term Monitoring
LUT	Look-Up Table
MAX-DOAS	Multi-Axis DOAS
MDA	MacDonald Dettwiler and Associates Ltd.
MEI	Multivariate ENSO Index
MERLIN	Methane Remote Sensing Lidar Mission
MESSy	Modular Earth Submodel System
MetOp	Meteorological Operational Polar Satellites of EUMETSAT
ML-CIRRUS	Midlatitude Cirrus
MLE	Maximum Likelihood Estimation
MLP	Multi-Layer Perceptron

MODIS	Moderate Resolution Imaging Spectroradiometer
MOME	Matrix Operator with Matrix Exponential
MOZART	Model for Ozone and Related Chemical Tracers
MPC	Mission Performance Center
MTP	Microwave Temperature Profiler
NASA	National Aeronautics and Space Administration
NDACC	Network for the Detection of Atmospheric Composition Change
netCDF	Network Common Data Format
NIR	Near-Infrared
NRT	Near-realtime
NSO	Netherlands Space Office
OCRA	Optical Cloud Recognition Algorithm
OEI	Ozone ENSO Index
OEM	Optimal Estimation Method
OMI	Ozone Monitoring Instrument
OPS-FPML	Ozone Profile Shapes retrieval using Full Physics Machine Learning
PBL	Planetary Boundary Layer
PCA	Principal Component Analysis
pCqSDHCP	Partially Correlated Quadratic Speed-Dependent Hard-Collision Profile
PILS	Profile Inversion for Limb Sounding
PLOC	Payload Operations Center
PMD	Polarization Measurement Device
QBO	Quasi-Biennial Oscillations
QDOAS	cross-platform application for DOAS retrievals
QWG	Quality Working Group
RAL	Rutherford Appleton Laboratory
RMS	Root Mean Square
RT	Radiative Transfer
rTCA	Reverse TCA
RTM	Radiative Transfer Model
S4	Sentinel-4
S5	Sentinel-5
S5P	Sentinel-5 Precursor
SAC	Simulator AOCS Service
SAF	Satellite Application Facility
SAS	Simulator Atmospheric Service
SCIAMACHY	Scanning Imaging Absorption Spectrometer for Atmospheric Chartography
SDC	Simulator Data Controller
SDV	Speed-dependent Voigt
SF	Sun Follower
SIS	Simulator Interpolation Service
SLS	Spectral Line Source
SLS	Simulator Lidar Service
SNR	Signal-to-Noise Ratio
SOFIA	Stratospheric Observatory for Infrared Astronomy
SOST	SCIAMACHY Operations Support Team
SQWG	SCIAMACHY Quality Working Group
SRON	Netherlands Institute for Space Research
SRS	Simulator Resampling Service
STREAM	Stratospheric Estimation Algorithm from Mainz
SZA	Sun Zenith Angle
TCA	Tricarboxylic Acid
TCCON	Total Carbon Column Observing Network
TCDR	Thematic Climate Data Record
TIRAMISU	Temperature Inversion Algorithm for Microwave Sounding
TMS	Truncated MS

TNO	Toegepast Natuurwetenschappelijk Onderzoek (Netherlands Organisation for Applied Scientific Research)
TROPOMI	Tropospheric Ozone Monitoring Instrument
TTOC	Tropical Tropospheric Ozone Columns
TU	Technical University
TUB	Technical University of Berlin
TUM	Technical University of Munich
UPAS	Universal Processor for UV/VIS Atmospheric Spectrometers
USTC	University of Science and Technology of China
UTC	Coordinated Universal Time
UV	Ultraviolet
UVN	UV-VIS-NIR
VCD	Vertical Column Density
VIS	Visible
VMR	Volume Mixing Ratio
VZA	View Zenith Angle
WMO	World Meteorological Organization

DLR at a Glance

DLR is the national aeronautics and space research center of the Federal Republic of Germany. Its extensive research and development work in aeronautics, space, energy, transport and security is integrated into national and international cooperative ventures. In addition to its own research, as Germany's Space Agency, DLR has been given responsibility by the federal government for the planning and implementation of the German space program. DLR is also the umbrella organization for the nation's largest project management agency.

Approximately 8000 people are employed at 20 locations in Germany: Cologne (headquarters), Augsburg, Berlin, Bonn, Braunschweig, Bremen, Bremerhaven, Dresden, Göttingen, Hamburg, Jena, Jülich, Lampoldshausen, Neustrelitz, Oberpfaffenhofen, Oldenburg, Stade, Stuttgart, Trauen and Weilheim. DLR has also offices in Brussels, Paris, Tokyo and Washington, D.C.

Remote Sensing Technology Institute
Institut für Methodik der Fernerkundung

DLR's Remote Sensing Technology Institute (IMF) is located in Oberpfaffenhofen, Berlin-Adlershof, Bremen and Neustrelitz.

IMF carries out research and development for retrieving geoin-formation from remote sensing data. It conducts basic research on physical principles of remote sensing and develops algorithms, techniques, and operational processing systems for synthetic aperture radar, optical remote sensing, and spectrometric sounding of the atmosphere. The processing systems are in operational use for national, European, and international Earth observation missions.

For preparation and in support of space missions, IMF operates a suite of optical airborne sensors and laboratories. The institute contributes its expertise to novel sensor and mission concepts.

The German Remote Sensing Data Center (DFD) and IMF form DLR's Earth Observation Center (EOC).